

THE PENNSYLVANIA STATE UNIVERSITY  
SCHREYER HONORS COLLEGE

DEPARTMENT OF CHEMICAL ENGINEERING

THEORY AND METHODS TOWARD AN UNDERSTANDING OF FLOW-INDUCED  
CRYSTALLIZATION OF ISOTACTIC POLYPROPYLENE

MICHAEL P. HOWARD  
Spring 2013

A thesis  
submitted in partial fulfillment  
of the requirements  
for a baccalaureate degree  
in Chemical Engineering  
with honors in Chemical Engineering.

Reviewed and approved\* by the following:

Scott T. Milner  
Joyce Chair Professor of Chemical Engineering  
Thesis Supervisor

Ali Borhan  
Professor of Chemical Engineering  
Honors Adviser

\*Signatures are on file in the Schreyer Honors College.

## Abstract

The flow-induced crystallization (FIC) of polyolefins is an important part of many industrial processes such as injection molding. Injection molding is used to make a variety of commercial products ranging from piping for chemical plants to everyday goods like water bottles and children's toys. It is well-documented experimentally that FIC can accelerate the rate of crystallization for isotactic polypropylene by a factor of one hundred (changing the crystallization time scale from a matter of hours to seconds), and also greatly affects the material properties of the crystallized product. Yet, the underlying physics of FIC are poorly understood. Some hypothesize that FIC occurs because flow reduces the melt state entropy, and thus eases the transition from melt to crystal. In order to test this hypothesis, it is necessary to understand (1) how crystals form in commercial melts, and (2) how flow might affect the entropy of the melt. Here we present two important steps towards understanding this phenomenon: a model for quiescent crystal nucleation in commercial melts, and a method for simulating dilute polymer solutions in flow. Ultimately, these may be combined with data from melt rheology of entropy reduction due to flow to predict the effects of FIC in commercial processes.

# Table of Contents

<b>List of Figures</b>	<b>iv</b>
<b>List of Tables</b>	<b>vi</b>
<b>Acknowledgements</b>	<b>vii</b>
<b>1 Introduction</b>	<b>1</b>
Bibliography . . . . .	6
<b>2 Stochastic splitting methods for Rouse chains in flow</b>	<b>7</b>
2.1 Exact solution . . . . .	8
2.1.1 Rouse modes . . . . .	9
2.1.2 Mixed flows . . . . .	12
2.1.3 Finite extensibility . . . . .	13
2.1.4 Simulations . . . . .	14
2.2 Operator splitting . . . . .	15
2.2.1 Convergence properties . . . . .	20
2.2.2 Stability . . . . .	23
2.2.3 Computational benchmarking . . . . .	26
2.3 Conclusions . . . . .	27
Bibliography . . . . .	30
<b>3 Cylindrical cap model for heterogeneous nucleation</b>	<b>32</b>
3.1 Background . . . . .	33
3.2 Analysis . . . . .	37
3.2.1 Growth rate . . . . .	38
3.2.2 Nucleation parameters . . . . .	39
3.2.3 Droplet experiments . . . . .	41
3.2.4 Experimental data . . . . .	43
3.3 Results and Discussion . . . . .	43
3.4 Conclusion . . . . .	46
Bibliography . . . . .	47
<b>4 Atomistic calculation of interfacial tensions</b>	<b>50</b>
4.1 Computational methods . . . . .	53
4.1.1 Normal mode analysis . . . . .	53
4.1.2 Tail corrections . . . . .	54
4.1.3 Finite thickness corrections . . . . .	57
4.1.4 Crystal structure . . . . .	58
4.1.5 Solid-state “simulations” . . . . .	60
4.2 Results and Discussion . . . . .	62

---

## TABLE OF CONTENTS

---

4.2.1	Crystal-Vacuum Interface . . . . .	62
4.2.2	Crystal-Surface Interface . . . . .	65
4.2.3	Contact Angle . . . . .	68
4.3	Conclusion . . . . .	70
	Bibliography . . . . .	72
<b>A</b>	<b>Shear flow solution to Rouse model</b>	<b>74</b>
<b>B</b>	<b>Discretization of shear flow solution</b>	<b>78</b>
<b>C</b>	<b>Mixed flow solution to Rouse model</b>	<b>80</b>
<b>D</b>	<b>Correlated random values</b>	<b>84</b>
<b>E</b>	<b>Convergence order analysis</b>	<b>86</b>
	Bibliography . . . . .	92
<b>F</b>	<b>Derivation of cylindrical cap critical barrier</b>	<b>93</b>
<b>G</b>	<b>Tail corrections</b>	<b>95</b>
<b>H</b>	<b>Finite thickness correction</b>	<b>98</b>
<b>I</b>	<b>Wall parameters</b>	<b>100</b>
<b>J</b>	<b>Effect of tail corrections on Hessian</b>	<b>102</b>

# List of Figures

1.1	Cartoon of commercial polymer melt crystallizing. Red indicates long polymer chains, while orange indicates shorter chains due to the polydispersity of the melt. Circles represent spherulites. Gray lines represent impurities, on which heterogeneous nuclei may form and grow. Blue arrows show shear flow profile. . . . .	2
2.1	Probability distributions for adjacent bead-to-bead distance squared for shear rates $\dot{\gamma}\tau_R = 0, 4, 8$ ; $n = 15$ bonds, $\alpha = 0.1$ for nonlinearity. Distance given in units of the average relaxed distance between adjacent beads, so $b_\gamma^2 = (\partial_s \mathbf{R})^2$ for a given shear rate, and $b_0^2 = \langle (\partial_s \mathbf{R})^2 \rangle$ for a chain in zero shear with a linear spring. . . . .	15
2.2	Log-log plots of mean-square error for bead positions. $\dot{\gamma}\tau_R = 4$ , $n = 15$ bonds, $\alpha = 0.1$ . For explicit Euler, $dt = (1/256)(\tau_R/n^2)$ and maximum step size = $64 dt$ . For operator splitting, $dt' = (1/16)(\tau_R/n^2)$ and maximum swap time = $64 dt'$ . . . . .	22
2.3	Log-log plots of the absolute averaged error in the mean-square distance between adjacent beads. $\dot{\gamma}\tau_R = 4$ , $n = 15$ bonds, $\alpha = 0.1$ . For explicit Euler method, $dt = (1/256)(\tau_R/n^2)$ and maximum step size = $64 dt$ . For operator splitting, $dt' = (1/16)(\tau_R/n^2)$ and maximum swap time = $64 dt'$ . . . . .	23
2.4	Steady-state errors for the odd-number Rouse modes. $\dot{\gamma}\tau_R = 4$ , $n = 15$ bonds, $\alpha = 0.1$ , $dt' = \tau_R/n^2$ . Chains were allowed to evolve for $4\tau_R$ to reach steady state. . . . .	24
2.5	Sample conformations computed over a particular noise history with different swap rates. The conformation with the largest wiggles is the “true” dynamics. The progressively smoother conformations were run with swap times $\Delta t_{\text{swap}} = 4dt'$ and $\Delta t_{\text{swap}} = 8dt'$ . . . . .	25
2.6	Relative computational time required for operator splitting compared to explicit Euler method, $\dot{\gamma}\tau_R = 4$ , $n = 15$ bonds, $\alpha = 0.1$ . The computational time for explicit Euler was evaluated at $dt = (1/16)\tau_R/n^2$ . . . . .	27
3.1	Diagram of a cylindrical cap nucleus forming on a flat featureless surface. Shading indicates actual nucleus formed, dashed line visualizes the full cylinder of which the nucleus is a cap. . . . .	35
3.2	Cross section of cylindrical cap nucleus. . . . .	35
3.3	Isotactic polypropylene spherulite linear growth rate $u$ versus temperature. Data taken from Ref. 38, Tables VI.9 and VI.10 (100% isotacticity). . . . .	39
3.4	Estimated homogeneous nucleation barrier plot for crystal and rotator phases of isotactic polypropylene. See main text for discussion of assumptions. . . . .	41
3.5	Quiescent crystallization times $t_{1/2}$ for bulk isotactic polypropylene versus temperature. Circles (Ref. 2) were determined with calorimetry for the first two data points and turbidity for the third. Crosses (Ref. 43) and triangles (Ref. 44) were both determined by DSC. . . . .	43
3.6	Linearized crystallization data, replotted from Figure 3.5. . . . .	44

---

## LIST OF FIGURES

---

4.1	Cross section of cylindrical cap nucleus with featureless surface. Nucleus extends into the page. . . . .	50
4.2	Schematic of integrals for tail corrections. . . . .	56
4.3	Projection of the $\alpha_1$ phase of isotactic polypropylene into the $a \sin \beta - b$ plane. White circles represent backbone carbons, while black circles represent methyl groups. Arrows indicate handedness of chain. All methyl groups point in the same $z$ direction. Fractional labels indicate vertical offset of methyl group in terms of fractions of one helical repeat. Dashed line indicates cleaved surface. . . . .	59
4.4	Simulation box for crystal slab against Hamaker-matched surface. As in Figure 4.3, white atoms indicate backbone carbons while black atoms indicate methyl carbons (hydrogen atoms not depicted). Carbon atoms are 75% space filling. Triangles outline four chains in a unit cell. . . . .	60
4.5	Surface tension of $\alpha_1$ isotactic polypropylene with vacuum extrapolated from 0 K. . . . .	63
4.6	Average magnitude of the first two thousand mode eigenvectors versus nearest edge distance for crystal-vacuum and bulk crystal systems. For the bulk crystal, the “edge” was defined as the simulation box in the gap dimension. . . . .	64
4.7	Surface tension of $\alpha_1$ isotactic polypropylene with featureless Hamaker-matched surface extrapolated from 0 K. . . . .	66
4.8	Cumulative fraction of normal modes below energy level with temperature $T$ . Inset shows a closeup of the 0 K to 200 K temperature range, where the phonons for the slab systems are shifted to be “softer”. . . . .	66
G.1	Sketch of cutoff scenarios for an atom in a slab with cutoff radius $r_c$ , thickness $2d$ , distances to edges $h_1$ and $h_2$ ( $h_1 \leq h_2$ ), and full periodicity in other dimensions. . . . .	96
H.1	Schematic of finite thickness correction. . . . .	98

## List of Tables

3.1	Literature and derived values of important physical properties of polyethylene (PE) and isotactic polypropylene (iPP). Transition temperatures were calculated from Refs. 39 and 40. $\Delta S_{RL}$ for iPP is an estimated value (see text for discussion). . . .	40
3.2	Interfacial tensions for polyethylene (PE) and isotactic polypropylene (iPP). Values for PE were obtained from Ref. 11. All tensions given in erg/cm <sup>2</sup> . . . . .	41
3.3	Contact angles and attempt frequencies. XL and RL indicate the assumption of nucleation via crystal (X) or rotator (R) nuclei. Attempt frequencies $I_0$ have units of cm <sup>-3</sup> s <sup>-1</sup> . $\theta_{KWB}$ is the contact angle obtained using nucleation data from Ref. 8. . . . .	44
4.1	Lattice parameters of $\alpha$ isotactic polypropylene from experiment and our simulations at 0 K and 300 K (all lengths in Å). . . . .	62

## Acknowledgements

I thank Scott Milner for involving me in undergraduate research, and for invaluable advice and mentorship. When I came to college, I never imagined that I would pursue a career in research. Scott not only invited me to try research as a freshman, but also showed me how rewarding and fun it can be. His advice and guidance during the last three years have been more valuable to me than perhaps even he realizes, and I have learned more from him than could be squeezed into four years in the classroom.

I thank Jian Qin for a warm welcome and help transitioning into a research lab, as well as countless useful and enjoyable discussions. I thank Darrell Velegol for professional mentoring, and for sharing his passion for teaching. I gratefully acknowledge NSF DMR-0907370, ACS-PRF 49964-ND7, CBET-1067554, and the Barry M. Goldwater Scholarship Foundation for support.

Finally, I thank my parents Steven and Susan Howard for everything that they have done to bring me to this point in my life. It has been a while since they helped a fifth grader struggle with his math homework at the kitchen table, but they are the best parents and role models that a son could ever ask for, and have made me the man that I am today.



## Introduction

It is hard to imagine a world without polyolefins. Plastic polymers are used to make everything from the piping in chemical plants to the water bottles we drink from. Production of polyethylene and polypropylene alone combines to over 130 million tonnes per year. In a typical industrial process for making plastic products, such as injection molding, molten polymer is subjected to intense stress as it is flowed through production equipment before it is supercooled into a semicrystalline product.

The final product is greatly affected by flow. At low flow rates, the product has large spherulites. As the flow rate increases, isotactic polypropylene forms many nuclei faster, and crystallizes up to one hundred times faster than it does without flow.<sup>1</sup> The increased nucleation rate leads to the formation of smaller spherulites, making the final product stronger. If enough stress is applied, the crystal structure changes entirely from strong spherulites to weak rod-like “shish-kebabs” in the areas of fastest flow.

Although this empirical understanding of flow-induced crystallization is sufficient for many industrial applications, there is a distinct lack of mechanistic understanding of *how* flow affects the crystallization process. Such a theory would be useful for predicting material properties and designing industrial processes. More broadly, flow can be used to induce orientation prior to crystallization in organic photovoltaic cells and to align silver nanotubes for electronics. An understanding of how flow affects crystallization in a simple polyolefin system could be extended to design better processes in these areas that will become increasingly important in the future as energy and precision technology demands grow.

It is theorized that flow enhances the nucleation rate by ordering the melt state of the polymer, which decreases the melt entropy and eases the transition from melt to crystal (lowers the critical nucleation barrier). However, a complete theoretical description of flow-induced crystallization in an industrial melt is complicated by both melt polydispersity and the presence of impurities (Fig. 1.1). It has been observed experimentally that the addition of a small fraction of

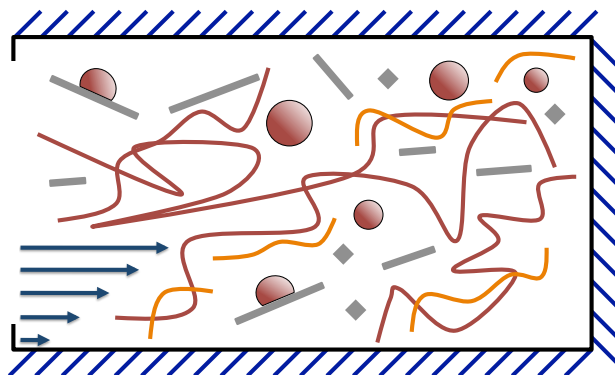


Figure 1.1: Cartoon of commercial polymer melt crystallizing. Red indicates long polymer chains, while orange indicates shorter chains due to the polydispersity of the melt. Circles represent spherulites. Gray lines represent impurities, on which heterogeneous nuclei may form and grow. Blue arrows show shear flow profile.

“long chains” (polymer with high  $M_w$ ) to polypropylene greatly enhances the rate of flow-induced crystallization, and promotes the formation of the anisotropic shish-kebab morphology.<sup>2</sup>

To test if flow especially enhances the nucleation rate near these long chains, it is necessary to quantify the effect of flow on the chain entropy. However, this is not a trivial theoretical task. Dilute polymers in shear flow are not well represented by simple average quantities because of their “molecular individualism”.<sup>3</sup> It is easiest to explore the behavior of these chains by direct simulation. Unfortunately, the typical approach to simulating such systems is surprisingly unstable and inefficient.

Melt impurities present another challenge to developing a theory of flow-induced crystallization. Crystal nuclei may form homogeneously (within the melt itself), or heterogeneously (for example, against the surface of an impurity, as shown in Figure 1.1). It is well-known that heterogeneous nucleation occurs more readily than homogeneous nucleation for quiescent melts at typical crystallization temperatures. Since bulk commercial samples of polypropylene are not carefully purified, it is expected that they would contain a large number of heterogeneities, causing heterogeneous nucleation to dominate the crystallization process. It would seem that the same nucleation mechanism should be dominant for both quiescent (no flow) and flow-induced crystallization.

However, there is a distinct lack of theory for heterogeneous nucleation of polymers, even

## 1. INTRODUCTION

---

in the quiescent case. Since flow-induced crystallization is hypothesized to increase the nucleation rate, it is important to have a sound theoretical understanding of the nucleation mechanism. Ultimately, a model of nucleation in bulk commercial samples of polypropylene can be combined with calculations from melt rheology or simulation to calculate the entropy reduction due to flow and estimate the increase in crystallization kinetics due to flow.

A major step towards understanding flow-induced crystallization is to address the issues of modeling quiescent heterogeneous nucleation, and of developing stable and efficient methods for simulating polymers in flow. To this end, I have explored three distinct areas of research:

1. *Numerical methods.* Efficient solution of nonlinear stochastic differential equations, such as the modified Rouse model in shear flow.
2. *Classical nucleation theory.* Modeling and theory of heterogeneous nucleation, analysis of quiescent crystallization in bulk samples of polypropylene.
3. *Molecular scale modeling.* Atomic level calculation of interfacial tensions of polypropylene crystal to validate the heterogeneous nucleation model.

Common to these research areas are classical elements of chemical engineering: mathematics, modeling, and computation. However, each area required mastery of a separate body of literature and set of techniques to build on these skills. Stochastic differential equations require different mathematics for solution and analysis than those needed for the deterministic equations that engineers typically encounter. Classical nucleation theory is an entirely different field from numerical analysis, with its basis in statistical mechanics, and has an extensive body of previous work tracing back to as early as 1938.<sup>4</sup> Molecular scale modeling and simulation are considerably newer fields; however, they necessitate a careful approach to computing, and attention to the details of the model or simulation.

During the course of conducting this research, I learned the need for careful appraisal of scientific literature, and perhaps even more valuably, the importance of perseverance even in the

---

## 1. INTRODUCTION

---

face of negative results. In a field like classical nucleation theory, which has a considerable body of established research, I learned that there will often be disagreement between experts on theory and interpretation. Some experiments may even have worrisome results. At first, this was incredibly frustrating. However, from this experience I learned that it is the scientist's job to carefully read and evaluate the literature, interpret and learn from past results, and report an honest and balanced opinion in new findings based on what is known at present.

In Chapter 2, a form of operator splitting is developed and applied to the nonlinear Rouse model in shear flow (a stochastic partial differential equation). This method for simulating dilute polymer solutions is a vast improvement on the numerical method typically implemented to evolve the Rouse model in time, reducing the total computational time by at least a factor of four. Splitting is generally applicable to a broad class of problems in stochastic dynamics in which noise competes with ordering and flow to determine steady-state parameter structures.

Chapter 3 proposes a model for heterogeneous nucleation of isotactic polypropylene in terms of a “cylindrical cap” with the critical size and barrier set by a contact angle. Quiescent crystallization data for bulk samples of polypropylene are analyzed to extract a contact angle in the range of  $40^\circ$  to  $70^\circ$  with a mean value of  $56^\circ$ , which corresponds to a factor six decrease in the critical barrier from the homogeneous case. This significant difference suggests that crystallization data for bulk samples should be analyzed in terms of heterogeneous (and not homogeneous) nucleation.

Finally, Chapter 4 describes a method for determining the surface tensions of crystalline polypropylene with vacuum and with a featureless Hamaker constant matched surface by all-atom calculations including contributions from phonons treated quantum-mechanically, and analytical “tail corrections” for long-ranged dispersion forces. The relative magnitudes of quantum effects, tail corrections, and finite system size effects on the surface tension are assessed. The surface tensions are extrapolated to finite temperature, and applied to the cylindrical cap model for heterogeneous nucleation to determine a contact angle of  $54 \pm 11^\circ$ . This is in excellent agreement with

## 1. INTRODUCTION

---

the result of Chapter 3, and lends supports to the cylindrical cap model for heterogeneous nucleation. Although the flow-induced crystallization problem is very complex, the results presented here may ultimately be combined with other data to make theoretical predictions about how flow affects crystallization in commercial samples.

## **Bibliography**

- [1] G. Kumaraswamy, A. Issaian, and J. Kornfield, *Macromolecules* **32**, 7537 (1999).
- [2] M. Seki, D. W. Thurman, J. P. Oberhauser, and J. A. Kornfield, *Macromolecules* **35**, 2583 (2002).
- [3] P. deGennes, *Science* **276**, 1999 (1997).
- [4] R. Becker, *Ann. Phys. (Berlin, Ger.)* **32**, 128 (1938).

## Stochastic splitting methods for Rouse chains in flow

The Rouse model underlies a great many simulations of polymer dynamics. It is used in slip-link models, and to represent dilute polymer solutions (neglecting hydrodynamic interactions), as well as unentangled polymer melts and concentrated solutions. In the Rouse model, a polymer is represented as a sequence of monomer beads bonded by springs. Each monomer feels a spring force from its neighbors, a drag force with respect to the surrounding fluid, and a stochastic force representing the effect of thermal fluctuations.

The Rouse model in shear flow is of interest because the resulting chain motion is complex and unsteady. Individual chains stretch in flow, and tumble over themselves when the leading end of the chain dips below the trailing end.

This unsteady motion leads generally to a varied ensemble of molecular configurations, which for some purposes are not well represented by simple average quantities such as chain average orientation or stretch. This variety of molecular configurations for sheared dilute polymers has been termed “molecular individualism”,<sup>1</sup> and is most easily explored by direct simulation. For the case of dilute and semidilute DNA solutions, such simulations have been compared to direct imaging studies carried out with fluorescently labeled DNA.<sup>2, 3</sup>

Numerical simulations of the Rouse model are also a central feature of sliplink simulations, which have been extensively used as a stochastic counterpart to tube-based constitutive theories of monodisperse and polydisperse linear chains.<sup>4–7</sup> In all of these simulations, a Rouse chain is somehow confined to a piecewise linear tube defined by a sequence of entanglement points called sliplinks, which are typically advected affinely with the mean flow.

The Rouse motion of the chain within the tube naturally imparts to the sliplink model the physics of contour fluctuations, constraint release, and stress relaxation via reptation. However, most of the CPU time in such simulations is spent on the Rouse motion; furthermore, the numerical method most often used is the simple but rather inaccurate and unstable explicit Euler method, which necessitates a very short timestep.

In many applications, the Rouse model is augmented with additional terms and interactions, which are typically nonlinear but deterministic. For example, the harmonic springs of the Rouse model can be upgraded to finitely extensible nonlinear elastic (FENE) springs, to limit the fully extended length of the chain.<sup>8</sup> Or, for simulations of dilute chains in a solution, various approximate hydrodynamic interactions may be added.<sup>9</sup> In either case, the random forces in the model are unaltered, and remain the chief reason for using simple explicit methods like Euler and thus short timesteps, which result in uncomfortable limitations on the lengths of chains that can be simulated.<sup>9</sup>

In short, most polymer dynamics simulations require time-evolution of the Rouse equation in some form. Much of the computational power in such simulations is spent numerically integrating the Rouse equation. This can become a rate-limiting computational step for large or lengthy simulations. However, if there were an exact solution to the Rouse equation, the time-evolution of the Rouse equation for any forward timestep could be done in one quick step, greatly speeding up the simulation.

## 2.1 Exact solution

The Rouse equation takes the form

$$\zeta \left( \frac{\partial \mathbf{R}(s,t)}{\partial t} - \mathbf{v}(\mathbf{R}(s,t)) \right) = K \frac{\partial^2 \mathbf{R}(s,t)}{\partial s^2} + \mathbf{f}(s,t) \quad (2.1)$$

where  $\mathbf{R}(s,t)$  is the chain position at arclength  $s$  and time  $t$ ,  $\mathbf{v}(\mathbf{r})$  is the imposed flow field,  $\zeta$  is the monomeric drag coefficient,  $K$  is the stiffness of the spring between neighboring beads, and  $\mathbf{f}(s,t)$  is the random force.

The noise  $\mathbf{f}(s,t)$  is taken to be delta-correlated in time and space, and Gaussian distributed



with zero mean, with variance given by

$$\langle \mathbf{f}_i(s, t) \mathbf{f}_j(s', t') \rangle = \frac{2\zeta}{\beta} \delta_{ij} \delta(s - s') \delta(t - t') \quad (2.2)$$

where  $\beta = 1/(kT)$ . The noise amplitude  $2\zeta/\beta$  is determined by requiring that the chain diffusion constant  $D$  satisfies the Stokes-Einstein relation  $D = kT/(N\zeta)$ .

### 2.1.1 Rouse modes

The Rouse equation is a system of linear constant-coefficient PDEs with a linear stochastic driving force, which is analytically solvable with Fourier analysis. Each position vector  $\mathbf{R}(s, t)$  can be represented as a linear combination of the Rouse modes  $X_p(t)$  as

$$\mathbf{R}(s, t) \cdot \hat{\mathbf{x}} = R_x(s, t) = \sum_{p=1}^{\infty} X_p(t) \cos\left(\frac{p\pi s}{n}\right) \quad (2.3)$$

where  $n$  is the arclength of the chain. Cosine expansion is chosen in order to impose tension-free ends on the chain. The  $p = 0$  mode is omitted here because it is only responsible for translational motion. Analogous equations relate  $y$  and  $z$  coordinates  $R_y(s, t)$  and  $R_z(s, t)$  to mode amplitudes  $Y_p(t)$  and  $Z_p(t)$ .

The inverse relation between the Rouse modes and the chain conformation is

$$X_p(t) = \frac{2}{n} \int_0^n R_x(s, t) \cos\left(\frac{p\pi s}{n}\right) ds \quad (2.4)$$

and analogously for  $Y_p(t)$  and  $R_y(s, t)$ .

The mode noise  $x_p$  is obtained by Fourier cosine transform of the real space noises  $f_x(s, t) = \mathbf{f}(s, t) \cdot \hat{\mathbf{x}}$  with Eq. 2.4. The mode noise has variance

$$\langle x_p(t) x_q(t') \rangle = \frac{4\zeta}{\beta n} \delta_{pq} \delta(t - t') \quad (2.5)$$

A simple shear flow field takes the form

$$\mathbf{v}(\mathbf{r}) = \dot{\gamma} \mathbf{\hat{x}} \quad (2.6)$$

with the shear rate  $\dot{\gamma}$ , the velocity direction taken as  $\mathbf{\hat{x}}$ , and the gradient direction taken as  $\mathbf{\hat{y}}$ . Since simple shear flow is a linear function of position, the Fourier transform can usefully be applied to it as well in Eq. 2.1.

For a shear flow like Eq. 2.6, only the  $R_x$  component in Eq. 2.1 is coupled to the flow.  $R_y$  and  $R_z$  are each independent of the other components. The equation of motion for  $R_x$  has a source term  $\dot{\gamma} R_y$  from the flow, but is completely decoupled from  $R_z$ . Thus, solving for  $R_z$  is trivial and analogous to solving for  $R_y$ , and we neglect it for simplicity.

Since the Rouse modes are only time dependent, Eq. 2.1 reduces to a system of linear ordinary differential equations (ODEs). Substituting the modes and rearranging gives

$$\zeta X_p' = \dot{\gamma} Y_p - K_p X_p + x_p \quad (2.7a)$$

$$\zeta Y_p' = -K_p Y_p + y_p \quad (2.7b)$$

where  $p$  is a positive integer,  $K_p = \pi^2 p^2 K / n^2$ , and  $x_p$  and  $y_p$  are the mode noises.

Solution for the Rouse modes  $Y_p$  (solving Eq. 2.7b) for a finite  $\Delta t = t_1 - t_0$  is a simple integrating factor problem. Let  $\omega_p = K_p / \zeta$ . Then,

$$\begin{aligned} Y_p(t_1) &= e^{-\omega_p \Delta t} Y_p(t_0) + \frac{1}{\zeta} \int_{t_0}^{t_1} e^{\omega_p(t-t_1)} y_p(t) dt \\ &= e^{-\omega_p \Delta t} Y_p(t_0) + \Delta Y_p \end{aligned} \quad (2.8)$$

$Y_p$  has a fading memory of its current value (the exponential term), plus a change due to stochastic noise ( $\Delta Y_p$ ). For sufficiently long times, the new mode value will “forget” its initial value and depend on only its noise history.

---

## 2. STOCHASTIC SPLITTING METHODS FOR ROUSE CHAINS IN FLOW

---

The governing equation for the modes  $X_p$  (Eq. 2.7a) depends not only on  $X_p$  but also on  $Y_p$  (because of the shear flow force). Substituting Eq. 2.8 into Eq. 2.7a, and solving with integrating factors over the same time range gives

$$\begin{aligned}
 X_p(t_1) &= e^{-\omega_p \Delta t} \left( X_p(t_0) + \frac{\dot{\gamma} \Delta t}{\zeta} Y_p(t_0) \right) + \frac{1}{\zeta} \int_{t_0}^{t_1} e^{\omega_p(t-t_1)} x_p(t) dt \\
 &\quad + \frac{\dot{\gamma}}{\zeta^2} \int_{t_0}^{t_1} (t_1 - t) e^{\omega_p(t-t_1)} y_p(t) dt \\
 &= e^{-\omega_p \Delta t} \left( X_p(t_0) + \frac{\dot{\gamma} \Delta t}{\zeta} Y_p(t_0) \right) + \Delta X_p^{(x)} + \frac{\dot{\gamma}}{\zeta} \Delta X_p^{(y)}
 \end{aligned} \tag{2.9}$$

Like  $Y_p$ ,  $X_p$  has a fading memory of its current value, and a stochastic forcing ( $\Delta X_p^{(x)}$ ). It also has a fading memory of the flow force at its current value, and an additional stochastic forcing that depends on  $y_p$ . Because of this dependence,  $X_p$  is correlated to  $Y_p$ .

The integrals  $\Delta Y_p$ ,  $\Delta X_p^{(x)}$ , and  $\Delta X_p^{(y)}$  can be thought of as summations of the mode noises (weighted by the exponential) over the given time range. Since the mode noises are Gaussian random variables with zero mean, any linear combination of these variables is also a Gaussian random variable with zero mean. Thus,  $\Delta Y_p$ ,  $\Delta X_p^{(x)}$ , and  $\Delta X_p^{(y)}$  are all Gaussian random variables with zero mean, and their variances can be computed as functions of  $\Delta t$  since the variances of the mode noises are known (see Appendix A).

$$\langle \Delta Y_p^2 \rangle = \langle \Delta X_p^{(x)2} \rangle = \frac{4}{\zeta \beta n} \frac{v_0(2\omega_p \Delta t)}{2\omega_p} \tag{2.10a}$$

$$\langle \Delta X_p^{(y)2} \rangle = \frac{4}{\zeta \beta n} \frac{v_1(2\omega_p \Delta t)}{8\omega_p^3} \tag{2.10b}$$

where  $v_0(x) = 1 - \exp(-x)$  and  $v_1(x) = 2 - (2 + 2x + x^2) \exp(-x)$ .

Frequently, the Rouse model is evolved forward in time to generate “snapshots” of a chain in a given flow. In order to do this numerically, the time period of interest  $\Delta t$  is usually divided into  $m$  fundamental steps, and the chain is evolved over a noise history with  $m$  different noise pairs (integrating over the noise). However, since the noise integrals  $\Delta Y_p$ ,  $\Delta X_p^{(x)}$ , and  $\Delta X_p^{(y)}$  are

themselves Gaussian random variables with known variance, it is sufficient to generate appropriate *representative* values for each over the *total* timestep  $\Delta t$ . Thus, only one triplet of Gaussian random variables needs to be generated for each  $\Delta t$ .

### 2.1.2 Mixed flows

The formal solution to the Rouse model generalizes to flow fields of mixed shear and extensional flows

$$\mathbf{v}(\mathbf{r}) = \dot{\gamma}(y\hat{\mathbf{x}} + \beta x\hat{\mathbf{y}}) \quad (2.11)$$

where  $\dot{\gamma}$  is the shear rate, and  $0 < \beta \leq 1$  is the “extensional character”. If  $\beta = 0$ ,  $\mathbf{v}$  is the shear flow profile, and the solution of Section 2.1.1 applies. If  $\beta = 1$ ,  $\mathbf{v}$  is pure extensional flow along  $y = x$ . Flow fields with  $\beta$  between zero and unity are of mixed type, with a character between shear and extensional.

The profile for a mixture of shear and extensional flow is still linear, so the solution proceeds through the Rouse modes as before

$$\zeta X'_p = \dot{\gamma} Y_p - K_p X_p + x_p \quad (2.12a)$$

$$\zeta Y'_p = \dot{\gamma} \beta X_p - K_p Y_p + y_p \quad (2.12b)$$

In matrix form

$$\begin{pmatrix} X'_p \\ Y'_p \end{pmatrix} = \frac{1}{\zeta} \begin{pmatrix} -K_p & \dot{\gamma} \\ \dot{\gamma} \beta & -K_p \end{pmatrix} \begin{pmatrix} X_p \\ Y_p \end{pmatrix} + \frac{1}{\zeta} \begin{pmatrix} x_p \\ y_p \end{pmatrix} \equiv \mathbf{M} \begin{pmatrix} X_p \\ Y_p \end{pmatrix} + \frac{1}{\zeta} \begin{pmatrix} x_p \\ y_p \end{pmatrix} \quad (2.13)$$

$\mathbf{M}$  has basis of eigenvectors  $(1, \sqrt{\beta})$  and  $(1, -\sqrt{\beta})$ . If  $\beta \neq 0$  (non-shear flow),  $\mathbf{M}$  has a complete basis of eigenvectors, and is diagonalizable.

If  $\lambda_1$  and  $\lambda_2$  are the corresponding eigenvalues for  $\mathbf{M}$ , Eq. 2.13 takes the form

$$\tilde{X}'_p = \lambda_1 \tilde{X}_p + \frac{1}{\zeta} \tilde{x}_p \quad (2.14a)$$

$$\tilde{Y}'_p = \lambda_2 \tilde{Y}_p + \frac{1}{\zeta} \tilde{y}_p \quad (2.14b)$$

where  $\tilde{X}_p$ ,  $\tilde{Y}_p$  and the noise terms are in the basis of the eigenspace. Note that the solution to the mixed flow case is actually simpler than the shear flow solution because the modes are decoupled in the eigenspace. The solution to Eq. 2.14 then proceeds as in Section 2.1.1 (see Appendix C).

### 2.1.3 Finite extensibility

The Rouse model assumes that the bonds of a chain are harmonic springs, which exert a force proportional to the stretch,  $F = -K\Delta x$ . The change in spring force (or, the “stiffness” of the spring)  $\partial F/\partial x$  is the spring constant  $K$ . However, in reality, the stiffness of the spring is not constant at all.

There are several models for such “anharmonic” (finitely extensible) springs. Although these models vary in form, they are fundamentally the same – the stiffness of the spring  $\partial F/\partial x$  increases with stretch. In most such models,  $\partial F/\partial x$  diverges at a certain stretch, which represents the spring becoming too stiff and “breaking”. Simulating such springs in a stochastic equation is inconvenient because it can require integration near the singularity.

A quartic spring is a suitable model for a spring that stiffens without the spring force diverging. The stretching energy for a quartic spring is

$$U = \int \frac{1}{2} K \left[ \left( \frac{\partial \mathbf{R}}{\partial s} \right)^2 + \frac{\alpha}{2} \left( \frac{\partial \mathbf{R}}{\partial s} \right)^4 \right] ds \quad (2.15)$$

This amounts to replacing the spring constant in the Rouse equation with a value that depends on

local stretch, given by

$$K \rightarrow K_0 \left[ 1 + \alpha \left( \frac{\partial \mathbf{R}}{\partial s} \right)^2 \right] \quad (2.16)$$

Here  $\alpha$  is a parameter that determines the stiffness of the springs. The value of  $\alpha$  is chosen so that the spring becomes  $k$  times stiffer than  $K_0$  at a given stretch  $b^2 = (\partial_s \mathbf{R})^2$ , so that

$$\alpha = \frac{k - 1}{b^2} \quad (2.17)$$

In our simulations, we chose  $\alpha = 0.1$  so that the spring constant would double at a squared bead-to-bead distance of 10.

#### 2.1.4 Simulations

It is computationally simple to collect data on the behavior of chains in shear flow with an explicit update formula for the Rouse modes. A valid starting conformation is defined in real space, transformed to Fourier space and evolved for a desired  $\Delta t$ , and then transformed back to real space for analysis. This data can be used to generate averages and probability distributions for chain properties, like end-to-end distance or inclination angle.

One measure of interest to nucleation theory is the squared distance between adjacent beads. Figure 2.1a shows this property for a chain with harmonic springs in increasing shear. As expected, the distributions broaden as  $\dot{\gamma}\tau_R$  increases (more flow stress). However, these distributions also demonstrate the physical simplifications of the Rouse model. Although probability distributions of the distance between adjacent beads are expected to broaden with increasing shear, they should not broaden indefinitely. The bonds of the chain should stretch to a point, but then become stiffer and more resistant to change. Otherwise, a chain could stretch to arbitrary length.

Figure 2.1b shows more realistic chain behavior after the quartic spring term is introduced. The distributions become narrower and steeper. This effect is most noticeable at high shear rates (where the harmonic springs would ordinarily become very stretched). For  $\dot{\gamma}\tau_R = 8$ , the distribution

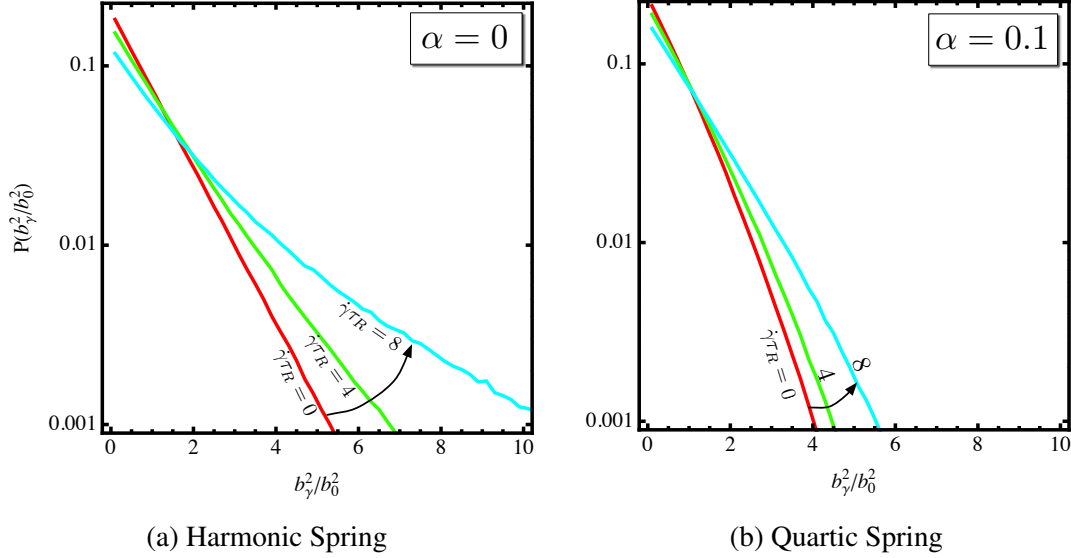


Figure 2.1: Probability distributions for adjacent bead-to-bead distance squared for shear rates  $\dot{\gamma}\tau_R = 0, 4, 8$ ;  $n = 15$  bonds,  $\alpha = 0.1$  for nonlinearity. Distance given in units of the average relaxed distance between adjacent beads, so  $b_\gamma^2 = \langle (\partial_s \mathbf{R})^2 \rangle$  for a given shear rate, and  $b_0^2 = \langle (\partial_s \mathbf{R})^2 \rangle$  for a chain in zero shear with a linear spring.

completely changes shape, becoming concave down. The effect of the quartic spring is most significant at high shear rates because the nonlinear term  $\alpha(\partial_s \mathbf{R})^2$  is negligible at small stretches (where the spring behaves mostly harmonically), and dominates at large stretches.

Although the anharmonic spring is a better model for the physical behavior of a chain in flow, it has unfortunate consequences for the formal solution to the Rouse equation. The Rouse equation (Eq. 2.1) is solvable because it is linear, and can be diagonalized with a Fourier cosine transform. The nonlinear term “breaks” the solution because the Rouse equation is no longer diagonalizable. Any modification to the Rouse model that introduces a nonlinear term would have this effect. Some type of numerical method is required to evolve the modified Rouse equation.

## 2.2 Operator splitting

The typical approach to solving the nonlinear Rouse equation is to integrate over a discrete noise history with very small timesteps, using a stochastic numerical integrator. Although such

methods solve deterministic differential equations reasonably well, they are not as effective at solving stochastic equations. Such numerical integrators march across the integration interval based on local values of the derivative at each integration step. If an equation is sufficiently “smooth” (several times differentiable), such methods work well because the value of the derivative changes smoothly and predictably.

Since deterministic equations are usually smooth, reasonably large integration steps can be taken, and these methods are efficient and accurate. However, stochastic equations are not smooth because of the noise, so small integration step sizes are required. A new noise term needs to be generated at each integration step. Since simulations of chain behavior typically require fairly large cumulative time scales, this process becomes computationally intensive.

Even though the modified Rouse equation is no longer linear, it is tempting to capitalize on the exact solution to the linear Rouse equation in designing a numerical solution method. The modified Rouse equation can be expressed as the sum of a linear part  $L$  and a nonlinear part  $N$ , where  $L$  represents the linear Rouse equation, and  $N$  represents the nonlinearity introduced by the quartic spring.

$$\begin{aligned}\frac{\partial \mathbf{R}}{\partial t} &= \mathbf{v}(\mathbf{R}) + \frac{1}{\zeta} \left[ K_0 + K_0 \alpha \left( \frac{\partial \mathbf{R}}{\partial s} \right)^2 \right] \frac{\partial^2 \mathbf{R}}{\partial s^2} + \frac{1}{\zeta} \mathbf{f} \\ &= \left( \mathbf{v}(\mathbf{R}) + \frac{K_0}{\zeta} \frac{\partial^2 \mathbf{R}}{\partial s^2} + \frac{1}{\zeta} \mathbf{f} \right) + \left[ \frac{K_0 \alpha}{\zeta} \left( \frac{\partial \mathbf{R}}{\partial s} \right)^2 \right] \frac{\partial^2 \mathbf{R}}{\partial s^2}\end{aligned}\tag{2.18a}$$

$$= L + N\tag{2.18b}$$

Although it would be difficult to solve this equation since it is nonlinear and stochastic, it is easy to solve either  $L$  or  $N$  independently.  $L$  can be evolved over the entire  $\Delta t$  in one step because it has an exact solution.  $N$  is integrable numerically with reasonably large timesteps since it is deterministic and smooth.

Operator splitting provides a general and effective way to solve equations like Eq. 2.18b, in which the time evolution operator is the sum of pieces that can each be solved separately, but



not easily at the same time. One first evolves  $L$  exactly, and then evolves  $N$  numerically. If these evolutions are done quickly enough (by swapping between operators over short time scales  $\Delta t_{\text{swap}}$ ), then Eq. 2.18b is solved exactly in the limit of  $\Delta t_{\text{swap}} \rightarrow 0$ . Error propagates as the swap times become “greedy” (too large). This method applies not only to the quartic spring, but also to *any* separable nonlinear operator.

Since  $L$  is solved in Fourier space, and numerical integration of  $N$  is done in real space, each swapping step requires one forward Fourier transform, and one inverse Fourier transform. Fast Fourier transforms (FFTs) can be applied if the solution is discrete in space. The Rouse model is discretized along arclength  $s$  into monomeric beads, with  $s = 1, 2, \dots, N$ . FFTs are  $O(N \log N)$  operations, so the conversion between Fourier space and real space can be done quickly.

Operator splitting is commonly employed for ordinary deterministic differential equations, as described in Ref. 10. Splitting was introduced by Ottinger in the context of stochastic dynamics of continuous fields.<sup>11</sup> The convergence properties of Ottinger’s algorithm were analyzed by Petersen.<sup>12</sup> More recently, stochastic splitting was applied by Lennon et al. to improve efficiency of complex Langevin simulations.<sup>13</sup>

Ideally, a numerical method has error that quickly decreases as the computational timestep  $h$  is taken smaller, and remains stable as large steps are taken. Numerical methods are compared in terms of the rate at which error becomes small, and the range of timesteps over which the methods are stable.

Convergence measures how quickly error decreases as the computational step size decreases. For deterministic equations of motion, convergence is straightforward to describe. A method is “of order  $\alpha$ ” if the difference between the approximate solution  $y_a$  and the true solution  $y$  for a single step  $h$  is

$$y(h, y_0) - y_a(h, y_0) = O(h^{\alpha+1}) \quad (2.19)$$

Across a finite time interval  $\Delta t$ ,  $\Delta t/h$  steps are taken, and the cumulative error for an order  $\alpha$

method is

$$y(\Delta t, y_0) - y_a(\Delta t, y_0) = O(h^\alpha) \quad (2.20)$$

If  $y$  is a vector, it is convenient to compute the error as the average of the sum of the squares of the differences between the components of  $y_a$  and  $y$  (the mean-square error). The mean-square error for a finite time interval will be  $O(h^{2\alpha})$ .

Stochastic differential equations can be thought of as deterministic equations with a particular time-dependent random driving force. As for deterministic equations, “strong” convergence measures the fidelity of the approximate solution to the true solution for a given noise history. For the Rouse model, the entire chain conformation  $\mathbf{R}$  is taken as  $y$ , and the solution error is the mean-square error in the bead positions. Finally, to eliminate sensitivity to the particular noise history, the solution error is averaged over many noise histories.

Frequently in simulations of polymer dynamics, the statistical properties for a chain are of greater interest than the actual solution for a particular noise history. These properties are represented by distribution functions  $P[\mathbf{R}(s, t)]$ , the probability for a given trajectory to be generated from a starting condition  $\mathbf{R}(s, 0)$ . The approximate distribution functions should approach the true distribution functions as the step size  $h$  becomes small.

Weak convergence describes how quickly the error between distributions decreases as  $h$  becomes small. If the distribution functions of possible trajectories match, then all correlation functions will also match. Here we briefly reprise the basic concepts related to weak convergence of numerical methods for stochastic differential equations, which are treated extensively in the monograph of Kloeden and Platen,<sup>14</sup> and can be adapted to the present problem.

A method has weak convergence “of order  $\beta$ ” if

$$\langle g[y(t)] \rangle - \langle g[y_a(t)] \rangle = O(h^\beta) \quad (2.21)$$

where  $g$  is any functional of the solution  $y(t)$  over some time interval  $\Delta t$ , and the average is taken

over both noise and initial conditions. Here,  $g[y(t)]$  can be any correlation function, such as the autocorrelation function  $y(t)y(t')$ . Note that any correlation function can be expressed in terms of the distribution  $P[y(t)]$ , so convergence of the approximate distribution  $P[y_a(t)]$  to the true distribution  $P[y(t)]$  ensures the validity of Eq. 2.21.

Although Eq. 2.21 provides a formal definition for weak convergence, it is not useful for verifying the convergence order of a numerical method. It is impossible to confirm explicitly that Eq. 2.21 holds for *all* possible correlation functions. It would be more convenient to have Eq. 2.21 in a form where the convergence of only a *small set* of quantities needs to be checked.

Consider the evolution of the distribution over a short time interval  $\Delta t$  from a well-defined initial configuration corresponding to a very narrow initial distribution function  $P(y_0)$ . If the time interval is short enough, the distribution does not have time to change very much. If a numerical scheme is accurate, then the small changes in the approximate distribution  $P(y_a)$  should also match the change in the true distribution  $P(y)$ . Since both the true and approximate distributions remain narrow after the short time  $\Delta t$ , it suffices to compare them by comparing the low-order moments of each distribution.

To verify weak convergence, the error between true and approximate moments of the distribution is compared in the limit of small time intervals. A useful theorem gives this criterion for weak convergence: the difference in the  $k$ -th moments for a single step  $h$  is<sup>14</sup>

$$\langle \Delta y^k(h) \rangle - \langle \Delta y_a^k(h) \rangle = O(h^{\beta+1}) \quad (2.22)$$

where  $k = 1, 2, \dots, 2\beta + 1$ . The corresponding cumulative error for the moments evaluated after a finite interval  $\Delta t$  is

$$\langle \Delta y^k(\Delta t) \rangle - \langle \Delta y_a^k(\Delta t) \rangle = O(h^\beta) \quad (2.23)$$

However, note that if  $y$  is a vector, it becomes increasingly cumbersome to compute the successive moments, which are tensors of increasing rank. This is certainly the case for the Rouse

model for a chain of  $N$  beads, for which there are  $2N$  degrees of freedom. Therefore in the present work, instead of explicitly verifying numerically the weak convergence criterion Eq. 2.23, we content ourselves with exemplifying weak convergence Eq. 2.21 for a particular property of interest, namely the mean squared distance between adjacent beads,  $(1/n) \sum (\partial_s \mathbf{R})^2$ .

### 2.2.1 Convergence properties

It is easier to understand the significance of convergence properties for some numerical method of interest by comparing it to a baseline numerical method. A suitable point of comparison is the explicit Euler method because it is a typical solution method for stochastic equations. The explicit Euler method is ordinarily not a good numerical method for solving deterministic equations because it is order  $\alpha = 1$  and has a narrow range of stability (see Section 2.2.2). However, the explicit Euler method is commonly used to solve stochastic equations because it only relies on the noise at the initial conditions to evolve the equation, and thus is simple to implement.

Operator splitting can be applied symmetrically or asymmetrically, yielding different convergence properties. Asymmetric splitting proceeds as described before, with alternation between  $L$  and  $N$  for equal times. In symmetric splitting,  $N$  is first evolved for half of the swap time, then  $L$  is evolved for the full swap time, and finally  $N$  is evolved for the remainder of the swap time. In the limit of infinite time evolution, symmetric and asymmetric splitting are indistinguishable. When evolved over finite time scales, symmetric splitting has better convergence properties, with only one additional FFT. For the purposes of this paper, operator splitting is taken to mean symmetric splitting.

The “true” dynamic for each method must be defined in order to compare error as the computational step size is varied. For the explicit Euler method, the true dynamics is defined as the solution for a stepsize  $h = dt$ . For operator splitting, the true dynamics is defined as the solution for a fundamental stepsize  $dt'$  when  $L$  and  $N$  are evolved on the swap time  $\Delta t_{\text{swap}} = 2dt'$  (the shortest possible discrete symmetric swap time). We define the true evolution under the nonlinear operator

---

## 2. STOCHASTIC SPLITTING METHODS FOR ROUSE CHAINS IN FLOW

---

$N$  to be the solution obtained using an accurate numerical integrator. In this way we can focus on the error introduced only by operator splitting.

Approximations are computed for the explicit Euler method by taking  $h = 2^k dt$ , and for operator splitting by taking  $\Delta t_{\text{swap}} = 2^k dt'$  for  $k = 1, 2, \dots, k_{\text{max}}$ . For each method, the approximations and true dynamic are evolved over the same short time period so that solutions change on equal time scales. The difference between the approximations and the true dynamic will be the cumulative error (of order  $\alpha$  or  $\beta$ ).

Since all dynamics are compared over the same time period, the overall time explored  $\Delta t$  must be at a minimum  $\Delta t = 2^{k_{\text{max}}} dt$ . However, the convergence theorems are only true for short stepsizes  $h$ . Thus, the fundamental steps  $dt$  and  $dt'$  must be very short times. Additionally, the explicit Euler method requires *very* small steps so that the solution does not explode over the total  $\Delta t$ .

To exemplify convergence orders with numerical results, the size of  $dt$  and  $dt'$  must be determined by trial-and-error for each method and convergence type. They must be chosen short enough that the distribution function does not have time to change very much, long enough that the distribution function *does* change, and also long enough that computational underflow is avoided. In general, good choices for  $dt$  and  $dt'$  to exhibit convergence properties are fractions of the shortest Rouse time  $\tau_R/n^2$ , and  $dt$  for the explicit Euler method is much shorter than  $dt'$  for operator splitting.

Analysis shows that both the explicit Euler method and operator splitting exhibit strong convergence of order  $\alpha = 1$  (see Appendix E). In order to verify strong convergence, the approximate and true dynamics for each method are evolved over a particular noise history. For the explicit Euler method, this simply requires computing a noise history at the start of each step, and applying an appropriate number of terms based on the size of  $h$ . For operator splitting, the exact solution to  $L$  must be adapted from continuous time to discrete time in order to apply the integrals over the noise as a summation of a noise history (see Appendix B).

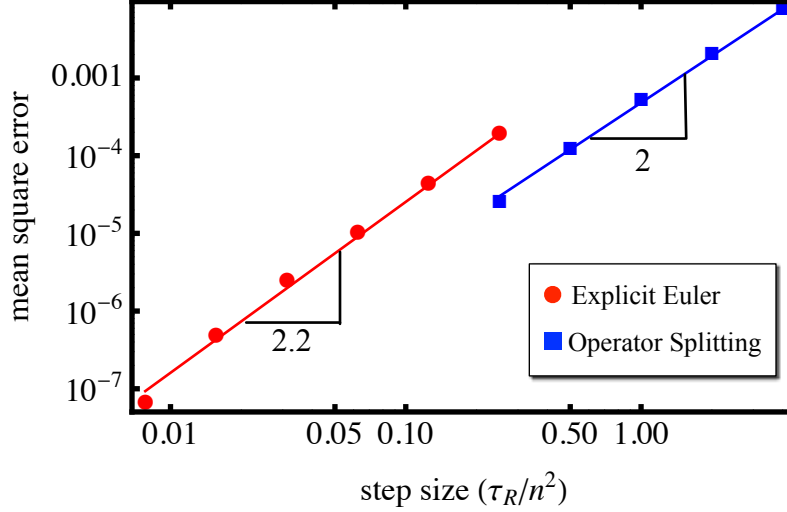


Figure 2.2: Log-log plots of mean-square error for bead positions.  $\dot{\gamma}\tau_R = 4$ ,  $n = 15$  bonds,  $\alpha = 0.1$ . For explicit Euler,  $dt = (1/256)(\tau_R/n^2)$  and maximum step size =  $64 dt$ . For operator splitting,  $dt' = (1/16)(\tau_R/n^2)$  and maximum swap time =  $64 dt'$ .

Since the mean-square error is  $O(h^{2\alpha})$ , log-log plots of the error versus step (swap) size should appear linear with slope  $2\alpha$  (Fig. 2.2). Both operator splitting and explicit Euler have approximately a slope of two, verifying that operator splitting and explicit Euler are strong order  $\alpha = 1$ .

In contrast to strong convergence, the explicit Euler method only has weak convergence order  $\beta = 1$  while operator splitting has order  $\beta = 2$  (see Appendix E). The change in the sum of squared distances between adjacent beads is computed using the explicit Euler method and operator splitting by averaging over initial configurations and noise. The error is log-log plotted versus the step (swap) size (Fig. 2.3).

Operator splitting has the same strong order as the explicit Euler method, but a better weak convergence order, which is often of greater interest. Note that in Figure 2.2 and Figure 2.3 the timesteps explored with operator splitting are considerably larger than those explored with explicit Euler. The timesteps for the explicit Euler method have to be taken shorter than operator splitting, or else the error in the solution diverges. This is a result of the most important advantage of operator splitting over the explicit Euler method: stability.

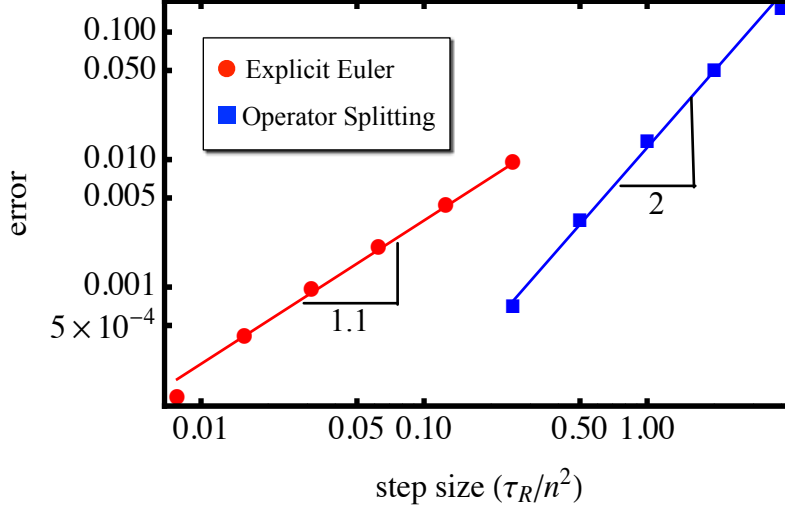


Figure 2.3: Log-log plots of the absolute averaged error in the mean-square distance between adjacent beads.  $\dot{\gamma}\tau_R = 4$ ,  $n = 15$  bonds,  $\alpha = 0.1$ . For explicit Euler method,  $dt = (1/256)(\tau_R/n^2)$  and maximum step size =  $64 dt$ . For operator splitting,  $dt' = (1/16)(\tau_R/n^2)$  and maximum swap time =  $64 dt'$ .

### 2.2.2 Stability

While convergence describes the behavior of the method as the time step becomes small, stability describes behavior as the time step becomes large. Stability is generally of more interest to running a simulation because one wants to take large timesteps to minimize the computational work.

Stability analysis studies how small error perturbations propagate as a numerical method marches forward. These errors may either die out, diverge, or maintain an approximately constant amplitude. The radius of stability describes how large of a step  $h$  can be taken without the method becoming unstable (causing the solution to diverge). Implicit numerical methods are typically more stable than explicit methods. Additionally, methods that are faithful at higher order derivatives tend to be stable.

The explicit Euler method is notoriously unstable. In the case of the nonlinear Rouse model, we observe that fundamental step sizes larger than  $dt = 2\tau_R/n^2$  cause the method to become un-

stable for  $n = 15$  bonds. This is why such small step sizes were required to verify the convergence orders (see Figs. 2.2 and 2.3).

Although the radius of stability can be investigated analytically, we have not carried out this analysis for operator splitting because of the complexities introduced by the nonlinear term. Instead, we have analyzed stability numerically by examining the steady-state error in the Rouse modes (Fig. 2.4). Let the error in the  $p$ -th mode  $\varepsilon_p$  be defined as

$$\varepsilon_p = \frac{\langle (X_p - X_p^{(a)})^2 \rangle}{\langle X_p^2 \rangle} \quad (2.24)$$

where  $X_p$  is the true mode and  $X_p^{(a)}$  is the approximate mode.

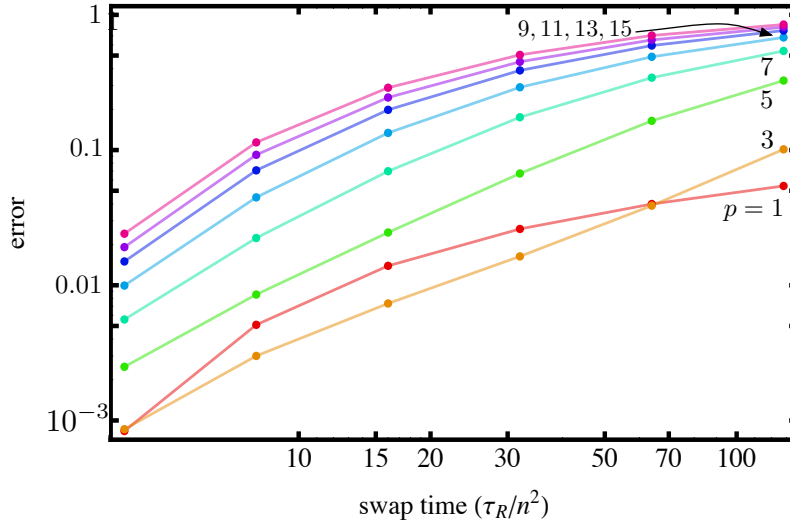


Figure 2.4: Steady-state errors for the odd-number Rouse modes.  $\dot{\gamma}\tau_R = 4$ ,  $n = 15$  bonds,  $\alpha = 0.1$ ,  $dt' = \tau_R/n^2$ . Chains were allowed to evolve for  $4\tau_R$  to reach steady state.

Figure 2.4 shows that as the swap time increases, the error in the Rouse modes increases. The higher modes are error-sensitive, so  $\varepsilon_p \rightarrow 1$  faster. The higher modes are more sensitive because changes occur on a shorter time scale than in the lower modes, so large swapping steps “skip” these dynamics. In contrast, the error in the lowest Rouse mode ( $p = 1$ ) is only about 10% if the swap time is approximately half the Rouse time. Further, the error for each mode at a given



---

## 2. STOCHASTIC SPLITTING METHODS FOR ROUSE CHAINS IN FLOW

---

swap time saturates to a steady-state value. Cumulatively, this implies unconditional stability for operator splitting.

Error in the high Rouse modes is not as important as error in the low Rouse modes for representing the polymer conformation. The low Rouse modes give the general orientation and shape of the conformation, while the high Rouse modes provide the “definition” to the conformation – the contours, sharp twists, and turns. As error is introduced to the high Rouse modes, chains become smoother (Fig. 2.5). However, the low Rouse modes are mostly faithful, so the chains remain synchronized to the true chain.

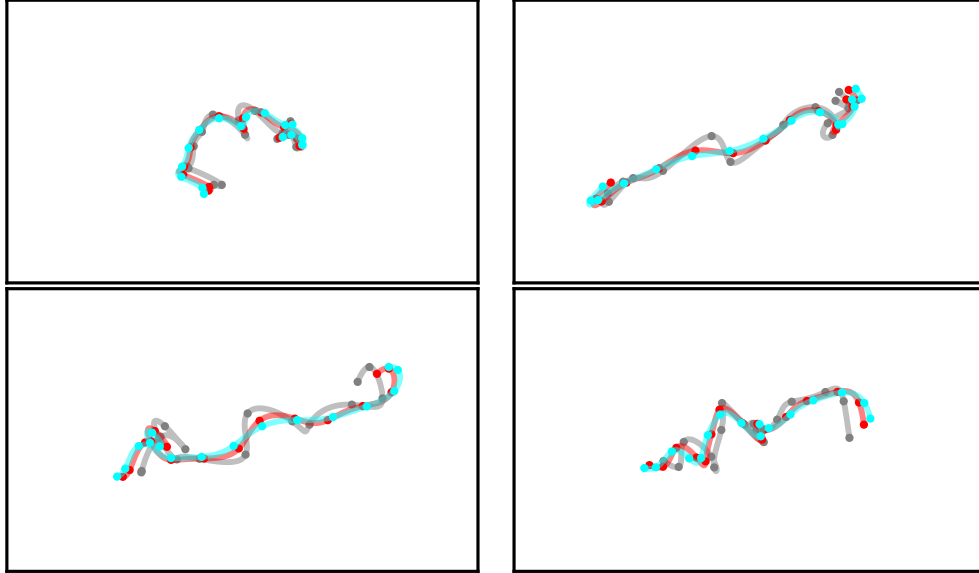


Figure 2.5: Sample conformations computed over a particular noise history with different swap rates. The conformation with the largest wiggles is the “true” dynamics. The progressively smoother conformations were run with swap times  $\Delta t_{\text{swap}} = 4dt'$  and  $\Delta t_{\text{swap}} = 8dt'$ .

One can impose an error tolerance on the modes (say, 10% in the highest mode), and select the corresponding swap time. Error will enter the solution almost immediately after the simulation begins, but it will not increase. The swap time can then be chosen depending on the required fidelity at a given mode.

### 2.2.3 Computational benchmarking

The computational efficiency of operator splitting was compared to the explicit Euler method. Operator splitting was implemented using FFTW v.3.3b for FFTs,<sup>15</sup> and the fifth order adaptive step size Cash-Karp Runge-Kutta method and driver from *Numerical Recipes in C* for numerical integration.<sup>16</sup> The time required for a single step was averaged over ten million steps, each with a different initial condition and noise.

It was observed that, as expected, explicit Euler had a constant computational time independent of step size. However, operator splitting had a variable time on a single step, due to the amount of work done by the numerical integrator, which depended on the starting chain configuration and step size.

It is worth noting that the amount of work required for operator splitting is dependent on the strength of the flow. Under strong shear flow, the chain becomes more stretched during the linear step than under weak or no flow. The stretched configuration makes the system stiffer for the numerical integrator in the nonlinear step, which necessitates shorter steps and thus more work. For our benchmarking tests, we have applied a fairly strong shear rate of  $\dot{\gamma}\tau_R = 4$ . If we were to simulate diffusion (no flow), it is likely that the added computational cost for operator splitting would be somewhat reduced.

A plot of the relative amount of computational time required on a single step ( $t_{OS}/t_E$ ) for operator splitting and explicit Euler versus step size (Fig. 2.6) shows that splitting initially requires about five times more computational work for single short steps. However, when large steps are taken, the increase in work is significantly less than the increase in step size.

This means that operator splitting can significantly reduce the amount of work required in standard practice. We previously noted that explicit Euler certainly became unstable near  $2\tau_R/n^2$  when  $n = 15$ . A safer step size to guarantee stability is  $(1/4)\tau_R/n^2$ , as we have used as a maximum in our convergence tests. If we enforce a modest error of no more than  $\approx 30\%$  (square error 0.1) in the highest three Rouse modes when  $n = 15$ , we find from Figure 2.4 that we can take a

step of approximately  $10\tau_R/n^2$  with operator splitting. From an interpolation of Figure 2.6, this corresponds to approximately a ten fold increase in work. However, we were able to increase the step size forty fold, so this corresponds to a factor of four speed up using operator splitting.

At very large timesteps, splitting is not faithful to the dynamics of the highest modes, even if it is faithful to the lowest modes. However, the highest modes still take on random values with the correct equilibrium statistics because they are regenerated at each step from a random noise with fading memory of the previous value. This is ultimately what leads to the stability of splitting, and prevents the error in the modes from blowing up. It is thus reasonable to take *very* large timesteps, with considerably higher error in the highest Rouse modes than 30%. It is ultimately this stability property that gives operator splitting the computational edge over explicit Euler.

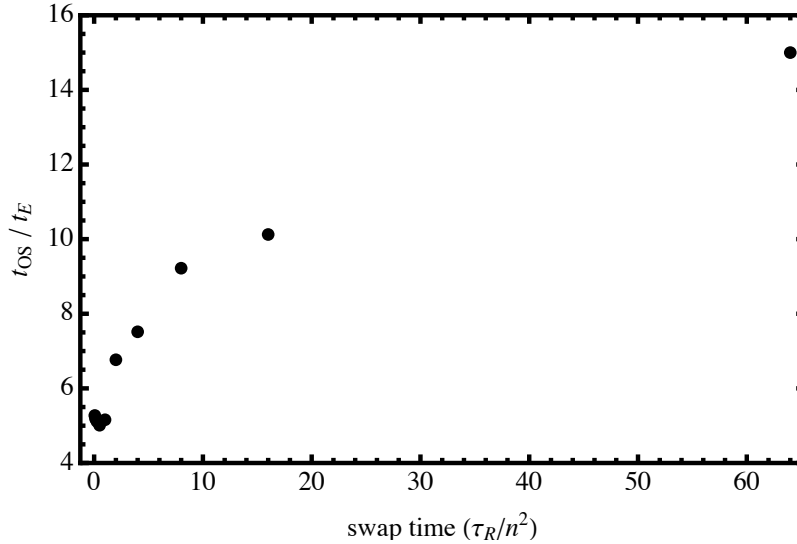


Figure 2.6: Relative computational time required for operator splitting compared to explicit Euler method,  $\dot{\gamma}\tau_R = 4$ ,  $n = 15$  bonds,  $\alpha = 0.1$ . The computational time for explicit Euler was evaluated at  $dt = (1/16)\tau_R/n^2$ .

## 2.3 Conclusions

Although ideally a numerical method has high order convergence and good stability properties, it is difficult to devise a method with weak convergence higher than order  $\beta = 2$  because

non-Gaussian random variables are required. Thus, operator splitting is a very useful numerical method because it has weak convergence  $\beta = 2$  and seemingly unconditional stability.

Operator splitting was successfully implemented to evolve the nonlinear Rouse equation in shear flow in order to generate probability distributions for the distance between adjacent beads. Strong convergence order  $\alpha = 1$  and weak convergence order  $\beta = 2$  were verified numerically. The stability of operator splitting was explored numerically, and shown to be almost unconditionally stable. The exact solution to the linear Rouse equation was also extended to mixed flow, demonstrating the generalizability of the method.

An implementation of operator splitting requires

1. *“Splittable” equation.* The differential equation must be separable into an exactly solved part, and a numerically solvable part.
2. *Faithful numerical integrator.* A high order numerical integrator is required to minimize error in the numerical solution, so that error is introduced mostly by operator splitting.
3. *Fast Fourier transforms.* Frequently, the exact solution is treated in Fourier space and the numerical solution in real space. Fast Fourier transform allows for cheap conversion between the two at each swapping step.

Although implementing operator splitting may seem inconvenient compared to a simple implementation of the explicit Euler method, the higher order weak convergence and stability properties of operator splitting are worth the effort. In particular, large stepsizes may be taken so that evolutions which would be computationally intensive with explicit Euler can be done considerably more quickly.

Operator splitting can be applied to a variety of problems in the stochastic dynamics of continuous-field order parameters, for which the evolution equations are of the same essential form as the nonlinear Rouse model, i.e., conforming to the three conditions listed above. Examples include mixed binary fluids in flow, block copolymer order-disorder transitions in flow, and flow

## 2. STOCHASTIC SPLITTING METHODS FOR ROUSE CHAINS IN FLOW

---

alignment of ordered fluids such as smectic or nematic liquid crystals. Flow effects in these systems are often treated as initial value problems with noise effects neglected, but clearly for each case there is a regime where noise effects compete with flow and ordering in determining the steady-state structure, for which the present splitting approach should prove useful.

## Bibliography

- [1] P. deGennes, *Science* **276**, 1999 (1997).
- [2] J. Hur *et al.*, *J. Rheol.* **45**, 421 (2001).
- [3] J. Hur, E. Shaqfeh, H. Babcock, and S. Chu, *Phys. Rev. E* **66**, 011915 (2002).
- [4] J. Schieber, J. Neergaard, and S. Gupta, *J. Rheol.* **47**, 213 (2003).
- [5] S. Shanbhag and R. Larson, *Macromolecules* **37**, 8160 (2004).
- [6] A. Likhtman, *Macromolecules* **38**, 6128 (2005).
- [7] Y. Masubuchi, G. Ianniruberto, F. Greco, and G. Marrucci, *Rheol. Acta* **46**, 297 (2006).
- [8] J. Hur, E. Shaqfeh, and R. Larson, *J. Rheol.* **44**, 713 (2000).
- [9] C. Hsieh and R. Larson, *J. Rheol.* **48**, 995 (2004).
- [10] W. H. Press, S. A. Teukolsky, W. T. Vetterling, and B. P. Flannery, in *Numerical Recipes: The Art Of Scientific Computing* (Cambridge University Press, Cambridge, UK, 2007), Chap. 20.3.3.
- [11] H. C. Ottinger, in *Stochastic Processes In Polymeric Fluids* (Springer, Berlin, 1996), Chap. 3.
- [12] W. Petersen, *SIAM J. Numer. Anal.* **35**, 1439 (1998).
- [13] E. M. Lennon *et al.*, *Multiscale Model. Sim.* **6**, 1347 (2007).
- [14] P. Kloeden and E. Platen, *Numerical Solution of Stochastic Differential Equations (Stochastic Modelling and Applied Probability)* (Springer, Berlin, 2011).
- [15] M. Frigo and S. G. Johnson, *Proc. IEEE* **93**, 216 (2005), special issue on “Program Generation, Optimization, and Platform Adaptation”.

- [16] W. H. Press, S. A. Teukolsky, W. T. Vetterling, and B. P. Flannery, in *Numerical recipes in C (2nd ed.): the art of scientific computing* (Cambridge University Press, Cambridge, UK, 1992), Chap. 16.2.

## Cylindrical cap model for heterogeneous nucleation

The flow-induced crystallization of polymers is of considerable interest because of its relevance to industrial processes such as injection molding, extrusion, and fiber spinning. In such processes, molten polymer is subjected to intense stress from flow before it is supercooled into a semicrystalline product. It is well documented that the properties of the material are strongly dependent on the processing conditions, and in particular much research has gone into studying the effect of flow on crystallization kinetics.<sup>1–4</sup>

In a typical experiment, a sample of molten polymer is subjected to a brief interval of shear flow, and its crystallinity is monitored over time. Shear flow causes isotactic polypropylene to crystallize one hundred times faster than it would in the absence of flow.<sup>1</sup> The flow-induced crystallization of isotactic polypropylene has been frequently studied in the literature, in part because of its ubiquitous industrial and commercial presence. Isotactic polypropylene is also particularly useful for flow studies because it crystallizes on a time scale that is not so fast that crystallization is hard to observe, but also not so slow that experiments become prohibitively long.

Crystallization is a nucleated process. Nuclei may be homogeneous (formed within the melt itself) or heterogeneous (formed on a surface such as an interface or a colloidal solid like dust or catalytic debris). Heterogeneous nucleation occurs more readily than homogeneous nucleation at higher temperatures. For isotactic polypropylene, heterogeneous nucleation tends to dominate in a temperature range of approximately  $115^{\circ}\text{C} - 150^{\circ}\text{C}$ , while homogeneous nucleation does not become significant until  $80^{\circ}\text{C} - 85^{\circ}\text{C}$ .<sup>5</sup> As a result, homogeneous nucleation is quite difficult to observe in bulk samples, such as the commercial polymers used in flow-induced crystallization experiments.

However, homogeneous quiescent crystallization has been investigated for polyolefins through heroic efforts to form isolated micron sized droplets of exquisitely clean sample, free of heterogeneities.<sup>6–10</sup> These experiments provide estimates of the homogeneous nucleation barrier. Homogeneous nucleation parameters for polyethylene have also been calculated with reasonable success,



but such calculations do not exist for isotactic polypropylene.<sup>11</sup>

Some have theorized that flow accelerates the rate of crystallization by increasing the rate of homogeneous nucleation. It stands to reason that quiescent crystallization of the same sample should also be controlled by the same mechanism. However, we shall show that quiescent crystallization data for bulk samples is inconsistent with this idea. Indeed, analysis of quiescent crystallization data for bulk polypropylene gives a nucleation barrier that is much smaller than the value obtained from careful homogeneous nucleation experiments. This suggests that heterogeneous nucleation is the relevant mechanism at typical experimental conditions in flow-induced crystallization experiments. Although substantial theory has been developed for homogeneous nucleation, there is a lack of theory for heterogeneous nucleation of polymers.

## 3.1 Background

Heterogeneous nucleation presents somewhat of a challenge to the theorist. Although it is well known that a polyolefin nucleus can be modeled as a cylinder with high energy end caps (due to chain folding), and a low energy lateral face, it is not readily apparent how to model the various heterogeneities that could be present in the melt. Not all heterogeneities are equal; there is no reasonable way to know what shape they have, how favorable they are as a substrate, or in what concentration they are present in any given sample. However, with reasonable assumptions, a simple model can be constructed.

The heterogeneities in a melt should be quite large compared to the size of a critical nucleus, which is on the order of a few nanometers. Locally, the overall shape of a heterogeneous particle is inconsequential; the surface appears to be flat. Further, we note that typical nucleating agents added to polyolefins to promote nucleation are insoluble crystals with exposed hydrocarbon groups.<sup>12</sup> Such a surface would not be specially templated to match the crystal structure on the Ångström scale – and yet it promotes nucleation. Thus it is reasonable to model the nucleating substrate as a flat, featureless surface. Finally, we expect that dispersed heterogeneous particles must be roughly

---

### 3. CYLINDRICAL CAP MODEL FOR HETEROGENEOUS NUCLEATION

---

Hamaker constant matched with the crystal so that the heterogeneities do not aggregate due to van der Waals attraction.

Extensive theory on the kinetics of crystallization has long been established by Turnbull, Hoffman, Lauritzen, and others.<sup>13–16</sup> Nuclei are either considered to form instantaneously (all at once) or sporadically (constant rate). Binsbergen has proposed a mechanism for heterogeneous nucleation in which all nuclei are preformed instantaneously in the melt.<sup>17–19</sup> However, given that the observed nucleation density has a strong temperature dependence, it seems more plausible that nucleation is occurring sporadically at a rate that may simply be so fast that it appears instantaneous at high supercoolings. Classical nucleation theory gives an expression for the nucleation rate  $I$  (per volume per time) as outlined in Refs. 13 and 20

$$I = I_0 \exp \left[ -\frac{U^*}{R(T - T_g^\infty)} \right] \exp \left[ -\frac{\Delta G^*}{kT} \right] \quad (3.1)$$

The first factor of the WLF form accounts for the temperature dependence of local motions that govern the attempt frequency for nucleating  $I_0$ , controlled by proximity to the glass transition.<sup>21</sup> As Hoffman has discussed, empirically  $T_g^\infty$  is about 50°C below the glass transition, and  $U^*$  has a value of about 1500 cal/mole for polyethylene.<sup>22</sup> Although some have assumed slightly different values  $U^*$ ,<sup>8</sup> we assume a value of 1500 cal/mole is also reasonable for polypropylene. The second factor is the Boltzmann weight for forming the critical nucleus with  $\Delta G^*$  the critical free energy barrier. The critical quiescent homogeneous nucleation barrier  $\Delta G_{\text{hom}}^*$  for a cylindrical bundle is

$$\Delta G_{\text{hom}}^* = \frac{8\pi\sigma_s^2\sigma_e}{(\Delta S\Delta T)^2} \quad (3.2)$$

where  $\sigma_s$  and  $\sigma_e$  are the lateral and end cap interfacial tensions,  $\Delta S$  is the volumetric entropy of transition, and  $\Delta T$  is the undercooling.<sup>23, 24</sup>

The simplest physical model for heterogeneous nucleation is a “spherical cap” nucleus against a flat surface.<sup>25–28</sup> Unfortunately, the spherical cap model does not apply to polymeric

---

### 3. CYLINDRICAL CAP MODEL FOR HETEROGENEOUS NUCLEATION

---

crystallization where the nucleus is better modeled as a cylinder. For polymers, heterogeneous nucleation should be modeled as a cylinder against a surface. This cylinder could be situated one of two ways on the surface: with either the end cap of a cylinder or the lateral face of a “cylindrical cap” parallel to the surface. However, it is difficult to see how the end cap chain folds could arrange in a favorable way if they abutted a flat interface. It seems that the natural choice is to model the nucleus as a cylindrical cap situated lengthwise on a flat surface, as shown in Figure 3.1.

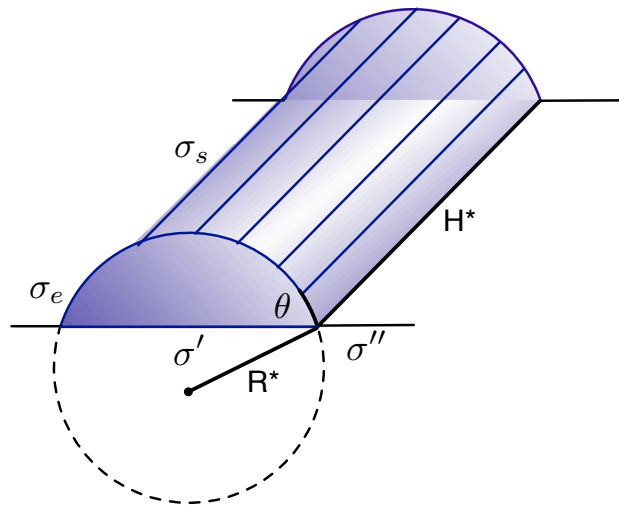


Figure 3.1: Diagram of a cylindrical cap nucleus forming on a flat featureless surface. Shading indicates actual nucleus formed, dashed line visualizes the full cylinder of which the nucleus is a cap.

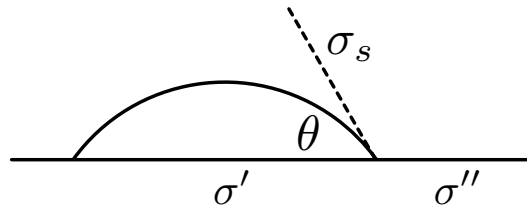


Figure 3.2: Cross section of cylindrical cap nucleus.

The geometry of the cylindrical cap is controlled by a contact angle, as shown in Figure 3.2. The contact angle arises from a balance between the lateral interfacial tension, and two additional interfacial tensions: the nucleus-surface tension  $\sigma'$  and the melt-surface tension  $\sigma''$ . If values for

---

### 3. CYLINDRICAL CAP MODEL FOR HETEROGENEOUS NUCLEATION

---

the interfacial tension are known, the contact angle may be approximated from Young's equation

$$\sigma' + \sigma_s \cos \theta = \sigma'' \quad (3.3)$$

In this geometry, it can be shown that the heterogeneous nucleation barrier  $\Delta G_{\text{het}}^*$  is

$$\begin{aligned} \Delta G_{\text{het}}^* &= \frac{8\pi\sigma_s^2\sigma_e}{(\Delta S\Delta T)^2} \left( \frac{\theta - \sin(2\theta)/2}{\pi} \right) \\ &= \Delta G_{\text{hom}}^* v(\theta) \end{aligned} \quad (3.4)$$

where  $\theta$  ranges from zero to  $\pi$ . Details of this derivation are included in Appendix F.

It is worth noting a few important features of Eq. 3.4, which are also true of the spherical cap model. The critical radius  $R^*$  and critical height  $H^*$  do not depend on the contact angle. We can interpret  $v(\theta)$  as the volume fraction of the homogeneous nucleus that must be formed. As the contact angle approaches zero (a perfectly wetting surface), the nucleation barrier disappears. In this limit, the nucleus is essentially already part of the solid, so there is no barrier to formation. As the contact angle approaches  $180^\circ$  (perfectly nonwetting surface), the original homogeneous barrier is recovered, since the nucleus and the surface are essentially non-interacting, and there is no advantage to having a surface present.

A common crystallization experiment is to observe the crystallinity of a bulk sample by turbidity or differential scanning calorimetry (DSC). The temperature dependent nucleation rate can be extracted and compared to Eq. 3.1 to obtain the nucleation barrier. Because the bulk samples are not exquisitely clean, heterogeneous nucleation dominates the crystallization. By applying homogeneous nucleation parameters and comparing the observed barrier to Eq. 3.4, the contact angle parameter can be extracted from  $v(\theta)$ . The contact angle should be in a “reasonable” range of values if our model is correct; that is, the contact angle should neither be so acute that the nucleus is unreasonably small nor be so obtuse that the effect of the heterogeneity is insignificant. Further support for our model can be provided by estimating a value for the contact angle from

molecular-level theory, and comparing to the experimental value. These calculations are treated in a companion publication.

## 3.2 Analysis

We assume that nucleation is random in space, occurring at a constant rate  $I$ , and that there is no site saturation effect. Site saturation occurs if the number of heterogeneities is limited. However, we would expect that a typical bulk commercial melt should have no shortage of impurities, and that these impurities should be well-dispersed in the sample so that nuclei can form at random. From Eq. 3.1, we expect that nucleation will occur at a constant rate at a constant undercooling. Given these conditions and a constant spherical crystal growth rate  $u$  the relative crystalline volume fraction  $X$  is

$$-\ln(1 - X) = \frac{\pi u^3}{3} t^4 I \quad (3.5)$$

which is the Avrami equation in the case of three dimensional sporadic growth.<sup>29-31</sup>

An expression for  $I$  can be written by combining Eqs. 3.1 and 3.4

$$I = I_0 \exp \left[ -\frac{U^*}{R(T - T_g^\infty)} \right] \exp \left[ -\frac{8\sigma_s^2 \sigma_e}{kT\Delta T^2 \Delta S^2} \left( \theta - \frac{1}{2} \sin 2\theta \right) \right] \quad (3.6)$$

$$= I_0 \exp \left[ -\frac{U^*}{R(T - T_g^\infty)} \right] \exp \left[ -\frac{A(\theta)}{T\Delta T^2} \right] \quad (3.7)$$

In the above,  $A(\theta)$  is a grouping of temperature independent constants

$$A(\theta) = \frac{8\sigma_s^2 \sigma_e}{k\Delta S^2} \left( \theta - \frac{1}{2} \sin 2\theta \right) \quad (3.8)$$

At the characteristic crystallization time  $t_{1/2}$ , the sample is approximately half crystallized. Substituting Eq. 3.7 into Eq. 3.5 and rearranging to put all terms which are a function of tempera-

ture on the left hand side gives

$$4 \ln t_{1/2} + 3 \ln u(T) - \frac{U^*}{R(T - T_g^\infty)} = A(\theta) \left( \frac{1}{T \Delta T^2} \right) + \ln \left( \frac{3 \ln 2}{\pi I_0} \right) \quad (3.9)$$

The value of the contact angle  $\theta$  and attempt frequency  $I_0$  can be extracted from the slope and intercept of a plot of the left hand side of Eq. 3.9 versus  $1/T \Delta T^2$  if values for the temperature dependent growth rate  $u(T)$  and the nucleation parameters in  $A(\theta)$  other than the contact angle are known.

### 3.2.1 Growth rate

Over the temperature range of the data collected, the linear growth rate of the crystal  $u$  varies considerably with temperature, so it may not be taken as a constant. The crystal growth rate is controlled by the crystallization temperature relative to the glass transition and the melting point. Hoffman has proposed a form similar to the form of the nucleation rate<sup>32, 33</sup>

$$u \sim \exp \left[ -\frac{U^*}{R(T - T_g^\infty)} \right] \exp \left[ -\frac{B}{T \Delta T} \right] \quad (3.10)$$

The constants  $U^*$  and  $T_g^\infty$  have the same meaning as in Eq. 3.1. Van Krevelen and Mandelkern et al have argued that the WLF form may not accurately model the slow down in chain mobility for semi-crystalline melts, and that this term is better represented as an Arrhenius activated process.<sup>20, 34</sup> Theory predicts that  $B$  takes the value of

$$B = \frac{4b_0 \sigma \sigma_e}{k \Delta S} \quad (3.11)$$

with  $b_0$  the thickness of the chain molecules, and  $\sigma$  and  $\sigma_e$  the interfacial tensions associated with growing a small rectangular patch of crystal.<sup>35</sup> The constant  $B$  typically has a value of about 265 K times the melting point.<sup>20</sup>

---

### 3. CYLINDRICAL CAP MODEL FOR HETEROGENEOUS NUCLEATION

---

For many polymers it has been found that Eq. 3.10 describes the data quite well, and fitting parameters are used to correct for small discrepancies. Indeed, for a class of “normal” polymers (including polyethylene and isotactic polystyrene) the crystal growth rate can be well-represented by a simple model, and (for some polymers) collapsed onto a single master curve, as has been shown by Gandica and Magill.<sup>20, 33, 36</sup>

Unfortunately, polypropylene does not belong to this privileged class of “normal” polymers. Ratajski and Janeschitz-Kriegl have shown that at times experimentally determined growth rates deviate from theory by as much as a full decade.<sup>37</sup> Some theorize that this discrepancy is due to the different growth regimes of the  $\alpha$  phase.<sup>33</sup> For our purposes, the crystal growth of polypropylene has been shown experimentally to be log-linear in the temperature range of interest, so we need only fit the experimental points, such as those given by Wunderlich and plotted in Figure 3.3.<sup>38</sup>

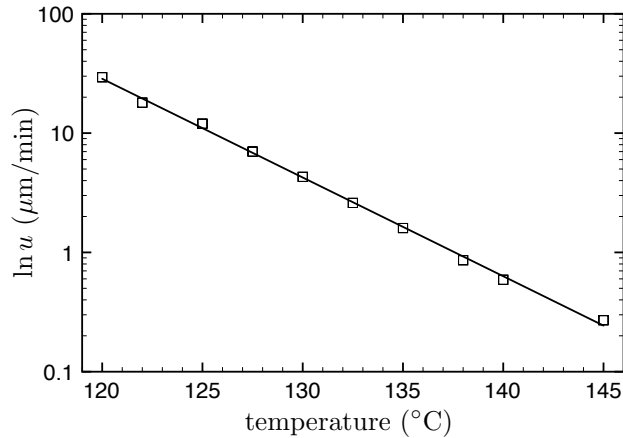


Figure 3.3: Isotactic polypropylene spherulite linear growth rate  $u$  versus temperature. Data taken from Ref. 38, Tables VI.9 and VI.10 (100% isotacticity).

#### 3.2.2 Nucleation parameters

In order to extract a contact angle from  $A(\theta)$ , values for the surface tensions and transition properties for polypropylene are needed. It is not obvious which parameter values should be used. Some polyolefins, such as polyethylene, are theorized to crystallize via a metastable rotator phase;

### 3. CYLINDRICAL CAP MODEL FOR HETEROGENEOUS NUCLEATION

however, it is unclear whether polypropylene crystallizes in this manner.<sup>11</sup> Although experimental data is available for a few of the parameters for the crystal phase, only sparse data is available for the rotator phase. Here, we will estimate values for all the crystal and rotator phase parameters for polypropylene based on experiment when available, and on the corresponding values for polyethylene otherwise.

Taking a linear approximation of free energy differences (X denotes crystal, R denotes rotator, L denotes liquid)

$$\Delta F_{XR} = \Delta F_{XL} - \Delta F_{RL} = (T - T_{XL})\Delta S_{XL} - (T - T_{RL})\Delta S_{RL} \quad (3.12)$$

and requiring that  $\Delta F_{XR} = 0$  at equilibrium gives the rotator transition temperature  $T_{RL}^\infty$

$$T_{RL}^\infty = T_{XR}^\infty - \frac{\Delta S_{XL}}{\Delta S_{RL}}(T_{XR}^\infty - T_{XL}^\infty) \quad (3.13)$$

where  $T_{XR}^\infty$  and  $T_{XL}^\infty$  are determined from extrapolation of the melting and crystallization lines for polypropylene of Iijima and Strobl to infinite lamellar thickness,<sup>39, 40</sup>  $\Delta S_{XL}$  is taken from the literature,<sup>41</sup> and  $\Delta S_{RL}$  has been estimated by assuming that  $\Delta S_{RL}$  is in the same proportion to  $\Delta S_{XL}$  for polypropylene as for polyethylene.<sup>11</sup> The values of these properties are summarized in Table 3.1.

Table 3.1: Literature and derived values of important physical properties of polyethylene (PE) and isotactic polypropylene (iPP). Transition temperatures were calculated from Refs. 39 and 40.  $\Delta S_{RL}$  for iPP is an estimated value (see text for discussion).

	$\rho$ (g/cm <sup>3</sup> )	$\Delta H_f$ (kJ/mol)	$\Delta S_{XL}$ (J/g-K)	$\Delta S_{RL}$ (J/g-K)	$T_{XL}^\infty$	$T_{XR}^\infty$	$T_{RL}^\infty$
PE	0.784 <sup>42</sup>	$4.1 \pm 0.2$ <sup>41</sup>	0.718 <sup>10</sup>	0.485 <sup>10</sup>	145°C	158°C	139°C
iPP	0.853 <sup>41</sup>	$8.7 \pm 1.6$ <sup>41</sup>	$0.449 \pm 0.083$ <sup>41</sup>	$0.303 \pm 0.055$	188°C	193°C	185°C

The crystal end cap interfacial tension  $\sigma_e^{XL}$  can be determined experimentally from the Gibbs-Thomson relation and the slope of the melting line of Iijima and Strobl<sup>39</sup>

$$T_m(d) = T_m^\infty - \frac{2\sigma_e^{XL}}{\Delta S} \frac{1}{d} \quad (3.14)$$



### 3. CYLINDRICAL CAP MODEL FOR HETEROGENEOUS NUCLEATION

where  $d$  is the lamellar thickness.

Experimental values for the lateral surface tension  $\sigma_s$  are not available. Likewise, although  $\sigma_s$  has been calculated for polyethylene, such calculations have not been carried out for polypropylene.<sup>11</sup> Instead, we estimate the crystal lateral interfacial tension by assuming that it is proportional to the calculated polyethylene lateral tension by volumetric heat of fusion. The polypropylene rotator tensions are assumed proportional to the crystal tensions by the same ratios as their polyethylene counterparts. These values are summarized in Table 3.2, and a barrier plot is shown in Figure 3.4.

Table 3.2: Interfacial tensions for polyethylene (PE) and isotactic polypropylene (iPP). Values for PE were obtained from Ref. 11. All tensions given in erg/cm<sup>2</sup>.

	$\sigma_E^{XL}$	$\sigma_S^{XL}$	$\sigma_E^{RL}$	$\sigma_S^{RL}$
PE	57.1	24.5	33.1	16.4
iPP	$46.5 \pm 8.6$	$15.9 \pm 3.0$	$27.0 \pm 5.0$	$10.7 \pm 2.0$

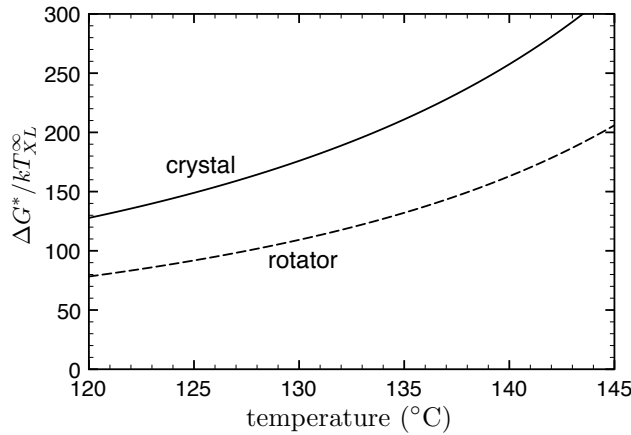


Figure 3.4: Estimated homogeneous nucleation barrier plot for crystal and rotator phases of isotactic polypropylene. See main text for discussion of assumptions.

#### 3.2.3 Droplet experiments

Reliable homogeneous nucleation experimental data can be collected by a carefully designed droplet experiment, such as those by Cormia, Price, and Turnbull (CPT);<sup>6, 7</sup> Koutsky, Walton, and Baer (KWB);<sup>8</sup> Ross and Frolen (RF),<sup>9</sup> or Kraack, Deutsche, and Sirota (KDS).<sup>10</sup> In the

---

### 3. CYLINDRICAL CAP MODEL FOR HETEROGENEOUS NUCLEATION

---

method of KWB, droplets of polymer solution were sprayed by atomizers onto slides and stabilized in silicone oil. CPT and RF achieved a droplet suspension by dispersing highly purified crystals into a viscous nonionic surfactant. KDS followed a similar method by dispersing into a solution of viscous surfactant and water to allow for pumped filtration of the solution.

Each individual droplet constitutes an individual nucleation “experiment” isolated from the others. The droplets which contain heterogeneities crystallize quickly, but homogeneous nucleation can then be observed in the remaining population of heterogeneity-free droplets. In all such experiments, it is necessary to create exquisitely clean samples so that most of the droplet population is free of heterogeneities. If these droplets are uniform in size, homogeneous nucleation parameters can be calculated by observing the number of homogeneous droplets that nucleate over time under a known thermal profile (e.g. isothermal or constant cooling).

We have reanalyzed the isothermal droplet experimental data of KWB to determine  $A(180^\circ)$ , the lumping of temperature independent constants for homogeneous nucleation. Although KWB report values for the interfacial tensions, we have reanalyzed their data ourselves to avoid estimating parameters or reverse engineering their calculations. To briefly summarize this procedure, details of which are well documented elsewhere,<sup>9</sup> the fraction of equal volume droplets crystallized is monitored over time for multiple undercoolings. The temperature dependent nucleation barrier  $I(T)$  at each undercooling is determined from the slope of a log-linear plot of this data. Then,  $A(180^\circ)$  can be determined from the slope of a plot of  $\ln I(T)$  versus  $1/T\Delta T^2$ . If we assume the crystal melting point  $T_{XL}^\infty$ , we recover a value of  $5.6 \times 10^7 \text{ K}^3$  for  $A(180^\circ)$ . We note that the choice of melting point temperature (crystal versus rotator) has a negligible effect since the two differ by only a few degrees, and the typical homogeneous crystallization temperatures are far from the melting point.

### 3.2.4 Experimental data

Quiescent crystallization data (crystallization time  $t_{1/2}$  versus temperature) for polypropylene is available from multiple experiments, and is reproduced in Figure 3.5. Kumaraswamy et al measured the crystallization time with a mixture of turbidity and DSC,<sup>2</sup> whereas Silvestre et al and Sajkiewicz measured only with DSC.<sup>43, 44</sup> The data of Silvestre et al and Sajkiewicz are in good agreement. It is unclear why the data of Kumaraswamy et al shows a softer temperature dependence. All experiments used some commercially available polymer with  $M_w$  approximately  $3.5 \times 10^5$  g/mol and with comparable polydispersity ( $M_w/M_n \approx 6 - 8$ ).

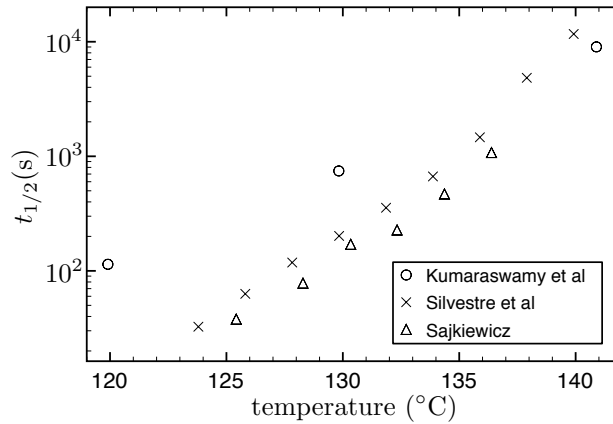


Figure 3.5: Quiescent crystallization times  $t_{1/2}$  for bulk isotactic polypropylene versus temperature. Circles (Ref. 2) were determined with calorimetry for the first two data points and turbidity for the third. Crosses (Ref. 43) and triangles (Ref. 44) were both determined by DSC.

## 3.3 Results and Discussion

Plotting according to Eq. 3.9 gives reasonably linear data, as shown in Figure 3.6. For each set of data, the contact angle and attempt frequencies were calculated using the estimated crystal (XL) and rotator (RL) parameters. The contact angle was also determined for each data set using the homogeneous  $A(180^\circ)$  obtained by the isothermal droplet experiments of KWB. These results are summarized in Table 3.3. Note that again the choice of melting point had a negligible effect on

### 3. CYLINDRICAL CAP MODEL FOR HETEROGENEOUS NUCLEATION

$I_0$ .

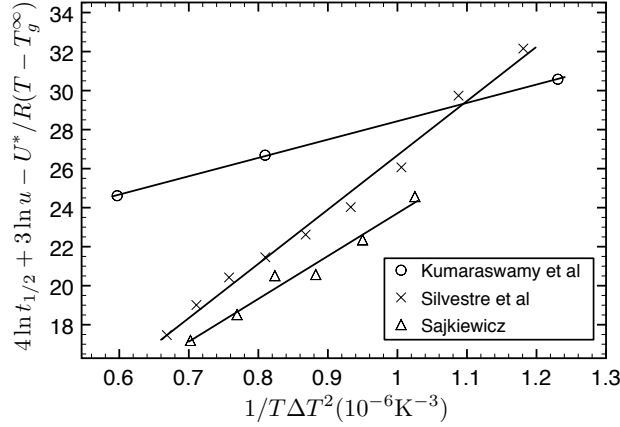


Figure 3.6: Linearized crystallization data, replotted from Figure 3.5.

Table 3.3: Contact angles and attempt frequencies. XL and RL indicate the assumption of nucleation via crystal (X) or rotator (R) nuclei. Attempt frequencies  $I_0$  have units of  $\text{cm}^{-3}\text{s}^{-1}$ .  $\theta_{\text{KWB}}$  is the contact angle obtained using nucleation data from Ref. 8.

	$\theta_{\text{XL}}$	$\log_{10} I_0^{\text{XL}}$	$\theta_{\text{RL}}$	$\log_{10} I_0^{\text{RL}}$	$\theta_{\text{KWB}}$
Ref. 2	$42^\circ \pm 6^\circ$	$9.1 \pm 0.4$	$49^\circ \pm 8^\circ$	$8.9 \pm 0.7$	$39^\circ \pm 1^\circ$
Ref. 43	$63^\circ \pm 11^\circ$	$18.2 \pm 1.2$	$75^\circ \pm 14^\circ$	$17.6 \pm 1.1$	$58^\circ \pm 2^\circ$
Ref. 44	$57^\circ \pm 10^\circ$	$16.8 \pm 2.0$	$68^\circ \pm 13^\circ$	$16.4 \pm 1.9$	$53^\circ \pm 5^\circ$

The values found for the attempt frequency were surprisingly low compared to the values typically reported for homogeneous nucleation. Typical values for  $I_0$  for homogeneous nucleation are of the order of  $10^{25} - 10^{35} \text{ cm}^{-3}\text{s}^{-1}$ .<sup>8, 45</sup> However, if the atypical data set of Kumaraswamy et al is disregarded, the determined attempt frequencies are roughly of the order of  $10^{18} \text{ cm}^{-3}\text{s}^{-1}$ , which is seven decades smaller than the lowest “typical” value reported for homogeneous nucleation. This may be partially accounted for by two factors: an extremely small “privileged” volume fraction of polymer in the neighborhood of a surface that may attempt to form a nucleus, and an even smaller fraction of this surface that presents a highly favorable substrate for nucleation. We may also partially attribute this discrepancy to the difficulty of determining an accurate value for  $I_0$  due to the high sensitivity of  $I_0$  to the quality of data and the fitting procedure, since it is determined by exponentiating the intercept of a linear fit.

### 3. CYLINDRICAL CAP MODEL FOR HETEROGENEOUS NUCLEATION

---

The calculated contact angles ranged from roughly  $40^\circ$  to  $70^\circ$  depending on parameter choice and data set, with a mean value of  $56^\circ$ . The contact angles calculated with the estimated crystal parameters were in excellent agreement with the angles calculated using the barrier of KWB. This may suggest that isotactic polypropylene does not crystallize via a rotator phase. However, regardless of parameter choice, the contact angles all lie in roughly the same range, and such a conclusion is not definitive.

It is worth noting that the standard error reported for the contact angles calculated by the estimated parameters is rather large. This is due to the large uncertainty in the heat of fusion of polypropylene, which propagates through our calculations. Bu, Cheng, and Wunderlich have discussed the difficulty in pinning down a reliable value for the heat of fusion.<sup>46</sup> However, in light of the approximations made in these calculations, we find these error bars acceptable.

The extracted contact angles were in a “reasonable” range of values. As previously discussed, it would be physically unreasonable to have a contact angle that is extremely acute or obtuse. If the contact angle were too acute, the size of the cylinder would become very small, to the point that the small number of chains may no longer be accurately modeled. In contrast, a very obtuse contact angle would suggest that the presence of the surface had only a negligible effect on the nucleation barrier, and the assumption of heterogeneous nucleation (instead of homogeneous nucleation) would become tenuous. We would expect that the contact angle should be somewhere in between these extremes. The fact that the contact angle is slightly acute is in agreement with Binsbergen’s experiments that have shown that good nucleating agents have exposed hydrocarbon groups.<sup>12</sup> These hydrocarbons would be expected to have a favorable interaction with the hydrocarbon nucleus, which should decrease the contact angle.

In a complementary approach in Chapter 4, we have reinforced our model by calculating a contact angle from a molecular scale description of the crystal and its interface. Our calculations give a value of  $54^\circ \pm 11^\circ$  for the contact angle, which is in excellent agreement with the extracted values. This suggests that the cylindrical cap model for heterogeneous nucleation is correct.

## 3.4 Conclusion

Given the extracted values for the contact angle and attempt frequency, it can be concluded that the cylindrical cap model for heterogeneous nucleation of polypropylene is a reasonable representation of crystallization in bulk commercial samples. Typical values for the contact angle correspond to an approximate factor of six decrease in the nucleation barrier predicted by homogeneous nucleation theory. Given this significant difference, crystallization in bulk samples (both quiescent and flow induced) should be analyzed as a heterogeneous nucleation event, and not a homogeneous one. This model may ultimately be combined with calculations from melt rheology of entropy reduction due to flow to estimate the heterogeneous nucleation barrier reduction due to flow, and hence the increase in crystallization rate.

## Bibliography

- [1] G. Kumaraswamy, A. Issaian, and J. Kornfield, *Macromolecules* **32**, 7537 (1999).
- [2] G. Kumaraswamy, J. A. Kornfield, F. Yeh, and B. S. Hsiao, *Macromolecules* **35**, 1762 (2002).
- [3] O. O. Mykhaylyk *et al.*, *Macromolecules* **41**, 1901 (2008).
- [4] O. O. Mykhaylyk *et al.*, *Macromolecules* **43**, 2389 (2010).
- [5] C. Silvestre, M. Di Lorenzo, and E. Di Pace, in *Handbook of Polyolefins*, 2nd ed., edited by C. Vasile (Taylor & Francis, New York, 2000), Chap. 9.
- [6] R. L. Cormia, F. P. Price, and D. Turnbull, *J. Chem. Phys.* **37**, 1333 (1962).
- [7] J. R. Burns and D. Turnbull, *J. Appl. Phys.* **37**, 4021 (1966).
- [8] J. Koutsky, A. Walton, and E. Baer, *Journal of Applied Physics* **38**, 1832 (1967).
- [9] G. Ross and L. Frolen, *J. Res. Natl. Bur. Stand., Sect. A* **79A**, 701 (1975).
- [10] H. Kraack, E. Sirota, and M. Deutsch, *J. Chem. Phys.* **112**, 6873 (2000).
- [11] S. T. Milner, *Soft Matter* **7**, 2909 (2011).
- [12] F. L. Binsbergen, *Polymer* **11**, 253 (1970).
- [13] D. Turnbull and J. Fisher, *J. Chem. Phys.* **17**, 71 (1949).
- [14] P. Flory and A. McIntyre, *J. Polym. Sci.* **18**, 592 (1955).
- [15] J. Lauritzen and J. Hoffman, *J. Res. Natl. Bur. Stand., Sect. A* **64A**, 73 (1960).
- [16] J. Hoffman, G. Davis, and J. Lauritzen, in *Treatise on Solid State Chemistry*, edited by N. Hannay (Plenum, New York, 1976), Vol. 3, Chap. 7.

- [17] F. L. Binsbergen and B. De Lange, *Polymer* **11**, 309 (1970).
- [18] F. L. Binsbergen, *Prog. Solid State Chem.* **8**, 189 (1973).
- [19] F. L. Binsbergen, *J. Polym. Sci., Polym. Phys. Ed.* **11**, 117 (1973).
- [20] D. Van Krevelen, in *Properties of Polymers*, 4th ed. (Elsevier, Amsterdam, 2009), Chap. 19.
- [21] M. Williams, R. Landel, and J. Ferry, *J. Am. Chem. Soc.* **77**, 3701 (1955).
- [22] J. Hoffman, *SPE Trans.* **4**, 315 (1964).
- [23] D. Turnbull and R. Cormia, *J. Chem. Phys.* **34**, 820 (1961).
- [24] D. Uhlmann, G. Kritchevsky, R. Straff, and G. Scherer, *J. Chem. Phys.* **62**, 4896 (1975).
- [25] K. L. Moazed and J. P. Hirth, *Surf. Sci.* **3**, 49 (1965).
- [26] R. D. Gretz, *Surf. Sci.* **5**, 239 (1966).
- [27] I. Markov, *Thin Solid Films* **8**, 281 (1971).
- [28] A. Sedehi, Z. H. Meiksin, and J. R. Blachere, *Thin Solid Films* **82**, 179 (1981).
- [29] M. Avrami, *J. Chem. Phys.* **7**, 1103 (1939).
- [30] M. Avrami, *J. Chem. Phys.* **8**, 212 (1940).
- [31] M. Avrami, *J. Chem. Phys.* **9**, 177 (1941).
- [32] J. Hoffman *et al.*, *Kolloid Z. Z. Polym.* **231**, 564 (1969).
- [33] H. Janeschitz-Kriegl, in *Crystallization Modalities in Polymer Melt Processing* (Springer, New York, 2009), Chap. 2.
- [34] L. Mandelkern, N. Jain, and H. Kim, *J. Polym. Sci., Polym. Phys. Ed.* **6**, 165 (1968).



- [35] F. Gornick and J. Hoffman, *Ind. Eng. Chem.* **58**, 41 (1966).
- [36] A. Gandica and J. Magill, *Polymer* **13**, 595 (1972).
- [37] E. Ratajski and H. Janeschitz-Kriegl, *Colloid Polym. Sci.* **274**, 938 (1996).
- [38] B. Wunderlich, in *Macromolecular Physics: Crystal Nucleation, Growth, Annealing* (Academic Press, New York, 1976), Vol. 2, Chap. 6.
- [39] M. Iijima and G. Strobl, *Macromolecules* **33**, 5204 (2000).
- [40] G. Strobl, *European Physical Journal E* **3**, 165 (2000).
- [41] J. Brandrup, E. Immergut, and E. Grulke, *Polymer Handbook*, 4th ed. (Wiley-Interscience, New York, 2003).
- [42] L. Fetters *et al.*, *Macromolecules* **27**, 4639 (1994).
- [43] C. Silvestre, S. Cimmino, D. Duraccio, and C. Schick, *Macromol. Rapid Commun.* **28**, 875 (2007).
- [44] P. Sajkiewicz, *J. Polym. Sci., Part B: Polym. Phys.* **40**, 1835 (2002).
- [45] Z. Bartczak and A. Galeski, *Polymer* **31**, 2027 (1990).
- [46] H. Bu, S. Cheng, and B. Wunderlich, *Makromol. Chem., Rapid Commun.* **9**, 75 (1988).

## Atomistic calculation of interfacial tensions

In typical polymer crystallization processes, bulk melts are quenched below the melting point where the polymer can nucleate and crystallize. Homogeneous nuclei form within the melt, while heterogeneous nuclei form on surfaces and interfaces. The presence of these interfaces reduces the barrier to heterogeneous nucleation as compared to the homogeneous barrier, and hence softens the temperature dependence of the nucleation rate compared to purely homogeneous nucleation. At typical quench temperatures for isotactic polypropylene ( $120^{\circ}\text{C} - 140^{\circ}\text{C}$ ), heterogeneous nucleation tends to dominate.<sup>1</sup>

In Chapter 3, we have proposed a simple “cylindrical cap” model for heterogeneous nucleation of isotactic polypropylene. The key controlling parameter in this model is the contact angle of the cap with a featureless Hamaker constant matched surface. As shown in Figure 4.1,  $\sigma_s$  is the interfacial tension of the lateral face of the nucleus with the melt,  $\sigma''$  is the interfacial tension of the melt with the substrate, and  $\sigma'$  is the interfacial tension of the crystal with the substrate.

We have extracted a value for the contact angle of roughly  $56^{\circ}$  from experimental data. One way to validate our model is to calculate a value for the contact angle from theory, and compare it to the experimental value. Although it is possible to estimate values for  $\sigma_s$  and  $\sigma''$ , such an estimate for  $\sigma'$  is difficult to make. A more convenient way to calculate  $\sigma'$  is by an all-atom calculation of the interfacial tension of the crystal against a model surface. With all three interfacial tensions known, Young’s equation can be applied to determine the contact angle.

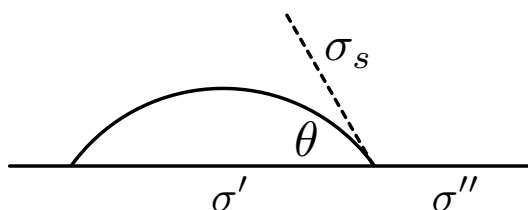


Figure 4.1: Cross section of cylindrical cap nucleus with featureless surface. Nucleus extends into the page.

#### 4. ATOMISTIC CALCULATION OF INTERFACIAL TENSIONS

---

Lacks and Rutledge have developed a method for computing thermodynamic properties from an atomistic Hamiltonian, including the effects of thermal fluctuations. In their method, the total free energy of a small system of atoms is minimized at finite temperature by assuming all chains in the unit cell are identical, and adjusting their relative position and orientation, as well as the lattice parameters. Quantum vibrational free energy is included by assuming a quasi-harmonic model, followed by construction of and numerical integration over the Brillouin zone on a mesh of wave vectors. Analytical derivatives are used to compute forces, and Ewald summation is used to treat “long-ranged” dispersion interactions (crystal cohesive energy). Lacks and Rutledge have computed the temperature dependence of mechanical properties of bulk crystalline polyethylene and isotactic polypropylene, including thermal expansion coefficients and elastic moduli.<sup>2, 3</sup> The quasi-harmonic approximation was found to be valid up to roughly one-half to two-thirds of the melting point, at which point anharmonic coupling effects were found to cause significant deviation from the harmonic approximation.<sup>4</sup>

Using this approach, Wilhelmi and Rutledge have computed the surface tension of polyethylene crystal at finite temperature.<sup>5</sup> They obtained the surface tension by comparing the free energy of a slab and a bulk crystal, again adjusting parameters to minimize the total free energy of the systems. Because of the limitation of system size to small numbers of atoms, they studied a system that was several unit cells wide in the slab dimension (roughly 50 Å), but only one unit cell wide in the other dimensions (a few Ångströms). They were unable to use Ewald summation methods for the dispersion interactions because of the two dimensional slab geometry, and instead applied a very large cutoff radius of 25 Å (it is unclear how they implemented such a cutoff radius given the narrow periodic boundaries of their system). They found the somewhat worrisome result that the surface tension *increased* at finite temperature, which is opposite of the behavior typically observed for virtually all liquids and polymer melts.<sup>6, 7</sup> We note that Ross and Frolen long ago empirically fitted a very weak temperature dependence of the same sign for the lateral surface tension of polyethylene in analyzing homogeneous nucleation experiments.<sup>8</sup> However, this fitting

#### 4. ATOMISTIC CALCULATION OF INTERFACIAL TENSIONS

---

procedure is sensitive, the temperature range is narrow, and the effect is weak.

In this work, we employ a simplified version of the Rutledge procedure. At present, it is our goal only to estimate a contact angle for the critical polypropylene nucleus by estimating the surface tension  $\sigma'$  in order to validate our nucleation model, and not to obtain precise values for properties at finite temperature. For this reason, we will carry out all calculations at 0 K and extrapolate to higher temperatures. We will also assume that quantum effects have a negligible effect on the optimum lattice parameters at 0 K as observed in Ref. 2, and so the potential minimum is roughly the free energy minimum. These approximations greatly simplify the process of optimizing the crystal structure.

We expand on the Rutledge method in two important ways: (1) the inclusion of an index matched substrate for the crystal and (2) the inclusion of tail corrections and finite thickness corrections rather than increased cutoff radius to simulate “infinite” systems. We are unaware of others that have simulated the interfacial tension of a crystal against a surface towards an understanding of polymer nucleation.

Furthermore, with the advantage of modern computing power, we have undertaken to simulate a considerably larger system than was accessible to Wilhelmi and Rutledge. Although larger systems can more closely approximate the infinite system, they present new difficulties. Analytical derivatives and large cutoff radii are impractical for large systems. Instead, we can use analytical “tail corrections” unique to the slab geometry to calculate potential energies for infinite crystals and semi-infinite slabs from results obtained with finite cutoffs. We also introduce continuum corrections to account for the finite thickness of the slab system, which was noted to be a significant issue for the results of Ref. 5.

In this work we consider the surface tensions of two systems: a crystal-vacuum interface and a crystal-surface interface. For the crystal-vacuum interface, we estimate the surface tension of the crystal, and assess the relative contributions of quantum effects, tail corrections, and finite system sizes. For the crystal-surface interface, we again calculate the interfacial tension, and

combine it with other estimated parameters to calculate a value for the contact angle.

### 4.1 Computational methods

Interfacial tensions arise due to differences in free energy between bulk systems and slab systems with interfaces. The free energy has a potential energy contribution from bonded and nonbonded interactions, as well as an entropic contribution due to vibrations. Intuitively, it is expected that the potential energy of the crystal against the surface should be higher compared to the bulk crystal due to missing Lennard-Jones contacts, but the vibrational free energy should be slightly lowered due to the increased vibrational freedom of atoms near the surface. The surface tension is then given by the difference in free energy per area of interface

$$\sigma' = \frac{\partial F}{\partial A} = \frac{F_{\text{slab}} - F_{\text{xtal}}}{2A} \quad (4.1)$$

where  $F_{\text{slab}}$  and  $F_{\text{xtal}}$  are the Helmholtz free energies of the crystal against the surface and the bulk crystal respectively, and  $A$  is the cross sectional area of the interface (the factor of two accounts for the two faces of the slab).

#### 4.1.1 Normal mode analysis

The quasi-harmonic oscillator approximation is a reasonable model for the vibrational free energy.<sup>2</sup> We assume that the crystal free energy is approximately at a minimum when the potential energy is at a minimum. The Hamiltonian is expanded to quadratic order in displacement from the minimum energy positions. This expansion has a set of normal eigenmodes with frequency  $\omega_i$ , which decouple the vibrations to a set of independent harmonic oscillators. It is important to treat these normal modes quantum mechanically because many have energy much larger than  $kT$ . The

vibrational free energy  $F_v$  is then

$$F_v = \sum_i^{3N-3} \frac{\hbar \omega_i}{2} + \frac{1}{\beta} \sum_i^{3N-3} \ln \left( 1 - e^{-\beta \hbar \omega_i} \right) \quad (4.2)$$

where  $\beta = 1/kT$  and sums are taken over all normal mode angular frequencies  $\omega_i$ , neglecting the first three zero-modes which correspond to bulk translation of the 3D periodic system. For a system that has only 2D periodic boundary conditions, there will instead be  $3N - 2$  normal modes because one direction of periodicity is lost. The total free energy  $F$  is given by adding the potential minimum  $U_0$  to the vibrational energy  $F_v$ .

In practice, normal modes are computed for an atomistic-level model by thorough energy minimization followed by the construction and diagonalization of the mass-weighted Hessian matrix of the potential. The eigenvalues of the Hessian can then be converted to normal mode frequencies. We use the OPLS-aa force field for our molecular Hamiltonian, and capabilities of the GROMACS simulation package for energy minimization, Hessian construction, and diagonalization.<sup>9, 10</sup>

### 4.1.2 Tail corrections

Intermolecular van der Waals forces dominate the attractive forces in a crystal. Since these forces are relatively short-ranged (decaying as  $r^{-6}$ ), the typical approach in calculations with atomistic classical Hamiltonians (as in molecular dynamics simulations) is to enforce a cutoff on the order of a nanometer in order to improve efficiency. The resulting truncation errors in the force on a given atom are typically quite small. However, in quantities such as the potential energy, missing weak attractions from many distant atoms can add up to a significant difference.

The truncation effect is important when comparing the free energy of a bulk crystal to the free energy of a crystal slab. Although both the bulk crystal and the slab are missing cohesive energy beyond the cutoff, the slab is not missing as much energy because part of the space beyond the cutoff is vacuum. This means that the apparent potential energy of the bulk crystal is much

---

#### 4. ATOMISTIC CALCULATION OF INTERFACIAL TENSIONS

---

higher than its true value, while the apparent potential energy of the slab is only somewhat higher. This artificially reduces the difference in potential energy between the slab and bulk, which favors the formation of interfaces and causes the apparent surface tension to be lower than its true value.

To remedy this, we introduce analytical tail corrections for the van der Waals interactions, in which missing attractive energy beyond the cutoff is added back, approximating the missing atoms as a featureless continuum with the same density as the system. The Lennard-Jones 12-6 potential is

$$U(r) = 4\epsilon_{ij} \left( \frac{\sigma_{ij}^{12}}{r^{12}} - \frac{\sigma_{ij}^6}{r^6} \right) \quad (4.3)$$

where  $r$  is the interatomic distance, and  $\epsilon_{ij}$  and  $\sigma_{ij}$  have their usual meanings. A typical cutoff radius is approximately  $2.5\sigma_{ij}$ . Beyond this distance, the fully periodic system can be approximated as a structureless continuum.<sup>11</sup> Integrating beyond the cutoff sphere gives the “missing” potential energy  $U_{\text{sph}}$  of an atom of type  $i$  interacting with a density of type  $j$  in the fully periodic crystal (Figure 4.2a)

$$U_{\text{sph}}(r_c) = \frac{\rho_j}{2} \int_{r_c}^{\infty} U(r) 4\pi r^2 dr = 8\pi\rho_j\epsilon_{ij} \left[ \frac{\sigma_{ij}^{12}}{9r_c^9} - \frac{\sigma_{ij}^6}{3r_c^3} \right] \quad (4.4)$$

where  $r_c$  is the cutoff radius and  $\rho_j$  is the number density of the  $j$ -th interaction type. The full tail correction is given by summing over all atoms interacting with all possible density types.

This method applies well to the full crystal, which has fully periodic boundary conditions in all directions (i.e. uniform composition). However, it fails when an atom is not surrounded by a repeating structure with the same composition (for example, if there is a gap or surface in one direction as is the case for a crystal slab). The correction in Eq. 4.4 would artificially “credit” missing interactions in the void where no atoms exist.

Instead, the missing energy between an atom of type  $i$  and a density of type  $j$  must be found by integrating over only the volume of the slab beyond the cutoff radius ( $V'_c$ ), which is infinite in

---

#### 4. ATOMISTIC CALCULATION OF INTERFACIAL TENSIONS

---

two dimensions and finite in a third

$$\Delta U_{ij} = \frac{\rho_j}{2} \int_{V'_c} U(r_{ij}) d\mathbf{r} \quad (4.5)$$

where  $r_{ij}$  represents the distance between the atom and the density. This integral is not trivial to compute directly, but can instead be conveniently evaluated by manipulating simpler integrals. The general correction scheme is to add back the energy missing from the slab beyond the cutoff (as for the bulk crystal), but then subtract the energy that was artificially credited to the gapped dimension (where there is no crystal).

The tail correction for an atom of type  $i$  that is a distance  $h_1$  and  $h_2$  ( $h_1 \leq h_2$ ) from the finite edges of slab of thickness  $2d$  with cutoff radius  $r_c$  ( $\leq d$ ) is

$$\Delta U_{ij} = \begin{cases} U_{\text{sph}}(r_c) - U_{\text{half}}(h_1) - U_{\text{half}}(h_2) & h_1 \geq r_c \\ U_{\text{sph}}(r_c) - U_{\text{half}}(h_1) - U_{\text{half}}(h_2) + U_{\text{cap}}(r_c, h_1) & h_1 < r_c \\ U_{\text{sph}}(r_c)/2 - U_{\text{half}}(2d) & h_1 = 0 \end{cases} \quad (4.6)$$

where  $j$  indicates the type of density with which an atom of type  $i$  interacts. The full tail correction to the simulated potential is computed by summing over all atoms (each with a specific type  $i$  and edge distances) and then summing over all  $j$  atom types in the continuum.

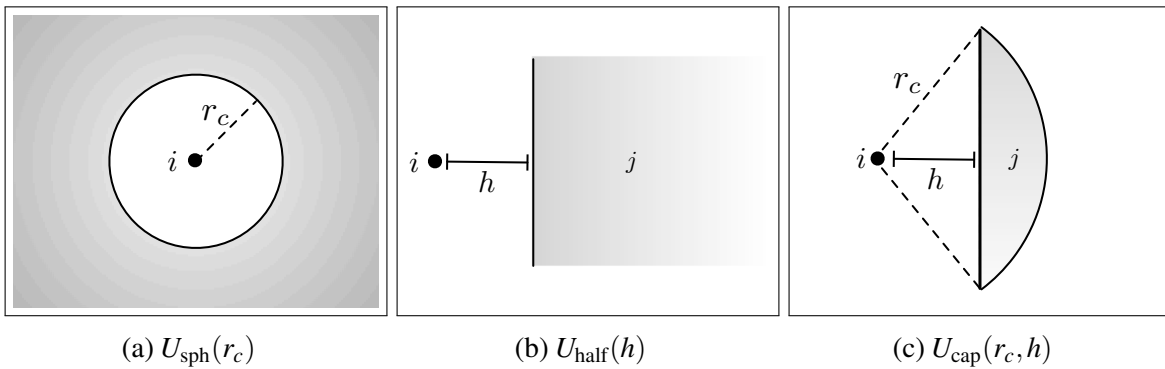


Figure 4.2: Schematic of integrals for tail corrections.

In Eq. 4.6,  $U_{\text{half}}$  is the potential energy of an atom of type  $i$  interacting with a semi-infinite



half plane with density type  $j$  a distance  $h$  away (Figure 4.2b)

$$U_{\text{half}}(h) = 2\pi\rho_j\epsilon_{ij} \left[ \frac{\sigma_{ij}^{12}}{45h^9} - \frac{\sigma_{ij}^6}{6h^3} \right] \quad (4.7)$$

$U_{\text{cap}}$  is the potential energy of an atom of type  $i$  interacting with a spherical cap with density type  $j$ , defined by a sphere of radius  $r_c$  with nearest distance  $h$  (Figure 4.2c)

$$U_{\text{cap}}(r_c, h) = 4\pi\rho_j\epsilon_{ij} \left[ \left( \frac{\sigma_{ij}^6}{3r_c^3} - \frac{\sigma_{ij}^{12}}{9r_c^9} \right) (1 - h_r) + \frac{\sigma_{ij}^{12}}{90h^9} (1 - h_r^{10}) - \frac{\sigma_{ij}^6}{12h^3} (1 - h_r^4) \right] \quad (4.8)$$

where  $h_r = h/r_c$ . Details are included as in Appendix G.

### 4.1.3 Finite thickness corrections

Although ideally we would analyzed systems of infinite size, the number of atoms that can be simulated is restricted by the time and memory required to compute and diagonalize the Hessian matrix during the normal modes analysis. This is not problematic for the fully periodic crystal, since only a sufficiently large system and tail corrections are required to guarantee that the infinite crystal is well represented. However, we would like to compare the energy of the infinite crystal to the energy of an “infinite” slab (that is, a slab where each surface is unaware that the other exists). If the slab is not sufficiently thick, the slab “misses” cohesive energy from its middle, which artificially raises the surface tension. However, if the original slab is sufficiently large, we can again correct this in the continuum.

The finite thickness correction to the surface tension  $\Delta\sigma'_{ij}$  for atoms of type  $i$  in the slab of thickness  $2d$  interacting with a missing density of type  $j$  is

$$\Delta\sigma'_{ij} = \frac{\pi}{2}\rho_i\rho_j\epsilon_{ij} \left[ \frac{\sigma_{ij}^{12}}{90} \left( \frac{1}{d^8} - \frac{1}{(2d)^8} \right) - \frac{\sigma_{ij}^6}{3} \left( \frac{1}{d^2} - \frac{1}{(2d)^2} \right) \right] \quad (4.9)$$

where  $\rho_i$  is the number density of atoms of type  $i$  in the slab. Combining our simulation results with

tail corrections and finite thickness corrections, we arrive at the final expression for the interfacial tension of the crystal against the surface from Eq. 4.1

$$\sigma' = \frac{\Delta U_0 + \Delta F_v}{2A} + \frac{\sum_{i,j}^{\text{slab}} \Delta U_{ij} - \sum_{i,j}^{\text{xtal}} U_{\text{sph}}(r_c)}{2A} + \sum_{i,j}^{\text{types}} \Delta \sigma'_{ij} \quad (4.10)$$

The corrected surface tension contains three groupings of terms: the “basic” surface tension resulting directly from simulation, the tail correction, and the slab finite thickness correction.  $\Delta U_0$  is the difference in the simulated potential energies, and  $\Delta F_v$  is the difference in vibrational free energy between the slab and crystal systems computed from Eq. 4.2. Both the bulk crystal and the slab system have the same number of atoms. Tail corrections are taken by summing over all  $i$  atoms and all  $j$  density atom types interacting with the slab or crystal. Both sums on  $\Delta \sigma'_{ij}$  are taken over all possible atom types. Details of this derivation are included in Appendix H.

#### 4.1.4 Crystal structure

We have simulated the monoclinic  $\alpha_1$  ( $Cc$ ) phase of isotactic polypropylene, as described by Natta and Corradini.<sup>12</sup> The  $\alpha_1$  phase has a unit cell consisting of four  $3_1$  helices with alternating handedness and all methyl groups pointing in the same upward or direction, as shown in Figure 4.3.

The  $\alpha$  phase of polypropylene is polymorphic. It has been shown computationally that the  $\alpha_2$  ( $P2_1/c$ ) phase is slightly more stable than the  $\alpha_1$  phase.<sup>13</sup> In the  $\alpha_2$  phase, chains with two neighboring methyl groups have their methyls oriented in the same  $z$  direction, while chains with only one neighboring methyl group point in the opposite  $z$  direction (for example, the middle two chains in Figure 4.3 would point upward if the outer two chains pointed downward). However, simulations by Ferro et al and Corradini et al have shown that the difference in potential energy of the  $\alpha_1$  and  $\alpha_2$  phases is marginal at best.<sup>14, 15</sup> Since the two phases have only minor differences in crystal structure and potential energy, the choice between  $\alpha_1$  and  $\alpha_2$  should have minimal effect on

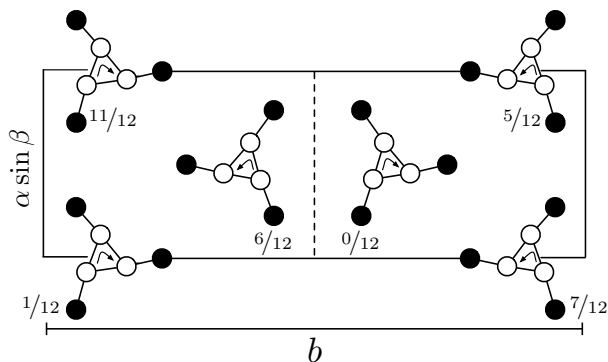


Figure 4.3: Projection of the  $\alpha_1$  phase of isotactic polypropylene into the  $a \sin \beta - b$  plane. White circles represent backbone carbons, while black circles represent methyl groups. Arrows indicate handedness of chain. All methyl groups point in the same  $z$  direction. Fractional labels indicate vertical offset of methyl group in terms of fractions of one helical repeat. Dashed line indicates cleaved surface.

the calculated surface tension. For simplicity of system construction, we have chosen to simulate the  $\alpha_1$  phase.

In order to simulate surfaces, it is necessary to choose a plane upon which to cleave the crystal. There are many different ways to cleave the polypropylene unit cell. We are interested in simulating the face that will have the lowest surface free energy, since it is expected that a nucleating crystal would naturally seek to minimize its surface energy. Wilhelmi and Rutledge found this to be the (100) facet for polyethylene in vacuum,<sup>5</sup> and a similar result might be expected for the analogous (010) facet for polypropylene in vacuum.

It is natural to ask if the same facet will also minimize the free energy of the crystal with a surface. By assumption, the surface in our model is featureless and has no corrugation or templating to match the crystal. We can then reasonably conclude that the surface with the lowest free energy will be a “smooth” face, which again corresponds to a smooth lateral surface. We have chosen to cleave the crystal at the (010) facet as indicated by the dashed line in Figure 4.3.

### 4.1.5 Solid-state “simulations”

All calculations were conducted using the GROMACS simulation package with the OPLS-aa force field and double precision methods for a system with 7,776 atoms.<sup>9, 10</sup> This system size corresponds to a supercell consisting of six unit cells in the  $a$  direction, two unit cells in the  $b$  direction, and six helical repeats, for a roughly cubic box in Cartesian coordinates.

Periodic boundary conditions and periodic covalent bonding were employed to represent an infinite system. Since chains were periodically bonded, an orthorhombic simulation box with chains appropriately shifted was used for simplicity. The crystal slab against vacuum was represented by adding a 10.0 nm gap to the crystal in fully periodic boundary conditions to isolate the slab in the gap dimension. The crystal against a Hamaker constant matched surface was modeled with two Lennard-Jones 9-3 walls (2D periodic boundary conditions) with parameters chosen to match the number density and Lennard-Jones parameters of the crystal (Figure 4.4). Details of choosing the wall parameters are included in Appendix I.

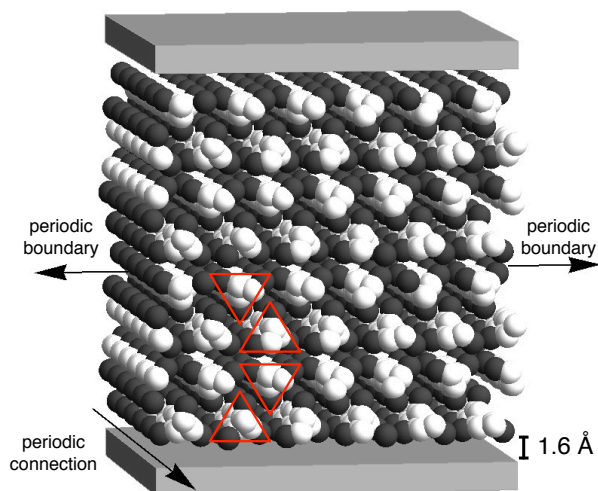


Figure 4.4: Simulation box for crystal slab against Hamaker-matched surface. As in Figure 4.3, white atoms indicate backbone carbons while black atoms indicate methyl carbons (hydrogen atoms not depicted). Carbon atoms are 75% space filling. Triangles outline four chains in a unit cell.

A switched 12-6 Lennard-Jones potential for van der Waals interactions (cutoff from 1.0

---

#### 4. ATOMISTIC CALCULATION OF INTERFACIAL TENSIONS

---

nm, switched from 0.8 nm) and Particle-Mesh-Ewald (PME) method for Coulomb electrostatics (short range cutoff of 1.3 nm, dielectric constant  $\epsilon = 2.3$ ) were employed for the normal modes analysis for the bulk crystal and crystal against vacuum.<sup>16</sup> Coulomb interactions with reaction field zero (cutoff from 1.0 nm,  $\epsilon_{rf} = \infty$ ) were used instead of PME for electrostatics for the crystal against the index matched surface, because PME is ill-suited for 2D periodic systems when the aperiodic dimension is not roughly three times the size of the periodic dimensions.<sup>9</sup> A neighbor list radius of 1.3 nm was used to ensure good energy conservation.

The box dimensions were manually adjusted to minimize the potential energy. The potential energy was then further minimized to a tolerance of  $10^{-4}$  kJ/mol-nm with the L-BFGS minimization algorithm, and the normal modes were computed. GROMACS returns the eigenvalues of the mass-weighted Hessian ( $\lambda_i$ ) in units of kJ/mol-nm<sup>2</sup>-amu. The normal mode frequencies  $\omega_i$  are then  $\sqrt{\lambda_i} \times 10^{12}$  s<sup>-1</sup>.

The system potential energy was then recalculated using a cutoff Lennard-Jones potential with the largest possible cutoff radius for both the Lennard-Jones and electrostatic interactions (1.9 nm). This cutoff also corresponds to half the slab thickness for the systems with interfaces, so the tail correction formula developed previously applies. Tail corrections and finite size corrections were then applied to this energy, and the interfacial tension was computed according to Eq. 4.10.

Short NPT simulations were also conducted to check that the OPLS force field can reasonably reproduce experimental lattice parameters. NPT simulation starting from the energy minimized structure was conducted at 1 atm and 300 K for 50 ps until the density equilibrated. Switched Lennard-Jones and PME electrostatics (with the same parameters used for the normal modes analysis) were used with a velocity rescaling thermostat ( $\tau = 0.1$  ps) and a Parrinello-Rahman barostat with anisotropic pressure coupling ( $\tau = 1.0$  ps,  $\kappa = 4.5 \times 10^{-5}$  bar<sup>-1</sup>).<sup>17</sup> We found that at 300 K the average simulated lattice parameters were in excellent agreement with the experimental parameters also determined at room temperature, with a maximum error of 2.4% in the  $b$  parameter (see Table 4.1). Based on this, we can be reasonably confident that the OPLS forcefield reasonably

represents the real polypropylene crystal.

Table 4.1: Lattice parameters of  $\alpha$  isotactic polypropylene from experiment and our simulations at 0 K and 300 K (all lengths in Å).

	Experiment	OPLS 0 K	OPLS 300 K
$a$	$6.65 \pm 0.05$	6.57	6.63
$b$	$20.96 \pm 0.15$	19.40	20.46
$c$	$6.50 \pm 0.05$	6.47	6.60
$\beta$	$99^\circ 20' \pm 1^\circ$	$99^\circ 36'$	$99^\circ 32'$

## 4.2 Results and Discussion

### 4.2.1 Crystal-Vacuum Interface

The surface tension of polypropylene against vacuum was found to be  $80.0 \text{ erg/cm}^2$  at 0 K. Inclusion of the normal modes in the free energy had a significant effect on the surface tension. The normal modes contribute both a temperature independent zero-point vibrational free energy term (the first term in Eq. 4.2), and a temperature dependent term. The difference in zero-point vibrational free energy lowers the surface tension by  $8.9 \text{ erg/cm}^2$  at 0 K. Differences in the temperature dependent vibrational free energy of the bulk and the slab further lowers the surface tension at higher temperatures. Figure 4.5 shows the surface tension extrapolated to typical crystallization temperatures by neglecting the thermal expansion of the crystal. We will discuss the validity of this extrapolation in more detail later.

The vibrational free energy significantly lowers the surface tension (especially at finite temperature) because of a “softening” of vibrations near the surface of the slab crystal compared to the vibrations in the bulk. Intuitively, modes near the surface have lower frequency because atoms near the surface have fewer neighbors and hence more freedom to vibrate than atoms in the bulk. These softer surface modes contribute more to the entropy. One way to visualize the soft surface modes is to examine the associated eigenvectors as a function of position in the slab. The

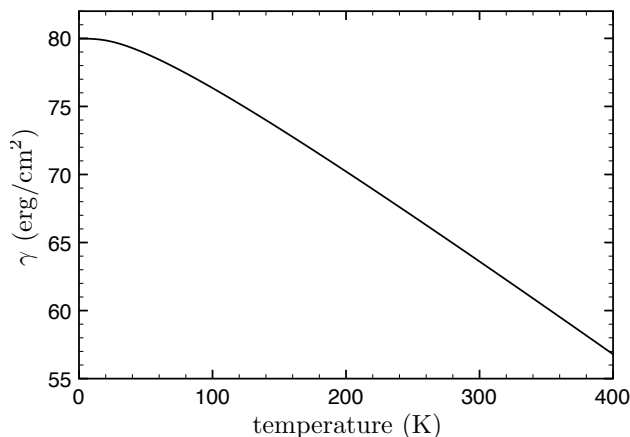


Figure 4.5: Surface tension of  $\alpha_1$  isotactic polypropylene with vacuum extrapolated from 0 K.

eigenvectors give the direction and magnitude of atom displacements in that mode. Figure 4.6 shows the magnitude of these eigenvectors versus the distance to the nearest edge averaged over the first two thousand normal modes (ordered by increasing frequency). The “nearest edge” for the bulk crystal (which is fully periodic and has no real “edge”) was defined as the edge of the simulation box in the same dimension as the slab.

As expected, the average magnitude of vibrations in the bulk crystal has essentially no spatial dependence. However, the magnitudes of vibrations within 10 percent of the nearest edge (roughly 4 Å) for the slab are considerably higher than those in the center of the slab. For higher frequency modes (not included in the average), the magnitudes show essentially no spatial dependence, just as for the bulk crystal. It is thus apparent that the vibrational free energy is lowered for the slab system due to modification of low frequency vibrations near the surface.

The tail corrections made a significant contribution to the surface tension. When the cutoff radius was increased from 1.0 nm for the normal modes analysis to 1.9 nm (the maximum cutoff radius in our periodic box), the surface tension increased by approximately 10.8 erg/cm<sup>2</sup>. Continuum corrections beyond this cutoff added an additional 3.1 erg/cm<sup>2</sup> to the surface tension for a total correction of 13.9 erg/cm<sup>2</sup>. This agrees with our expectations; increasing the cutoff radius and including tail corrections increases the total cohesive energy of the bulk system more than in

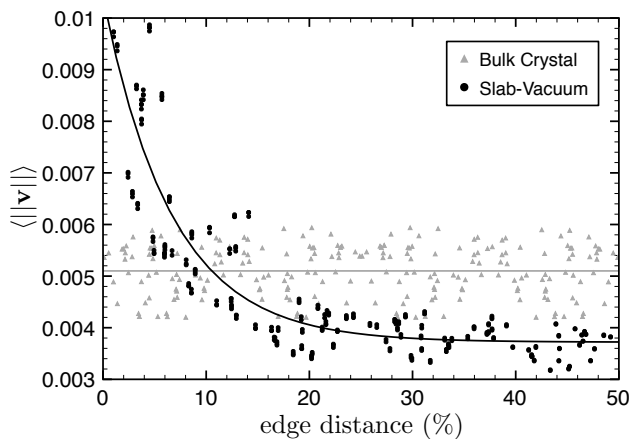


Figure 4.6: Average magnitude of the first two thousand mode eigenvectors versus nearest edge distance for crystal-vacuum and bulk crystal systems. For the bulk crystal, the “edge” was defined as the simulation box in the gap dimension.

the slab system since the tail corrections make atoms in the middle of the slab system “aware” that they are missing interactions that would be present in the bulk. Evidently, it is important to apply tail corrections when calculating surface tensions in systems like organic crystals, where cohesive intermolecular attractions dominate.

The significant contribution of tail corrections to the potential invites the question: are the normal modes, which are obtained from the Hessian of the potential, similarly sensitive to the missing tail energies? It would be unfortunate if the Hessian were significantly affected by cutoff effects, since further increasing the cutoff radius is impractical for numerical reasons. A cutoff radius of 1.0 nm is sufficiently large that (1) all important short-ranged interactions are treated discretely and (2) all atoms are close to their “true” minimum energy positions. Then, we can analyze the effect of tail corrections on the normal modes by analyzing the magnitude of second derivatives of the tail corrections (see Appendix J).

In the bulk system, the tail correction is a constant term that has no position dependence, so no correction to the Hessian is required. For the slab system, the tail corrections do depend on position, in the direction of the slab normal. Since the tail corrections are independent for each atom, this amounts to correcting only one-third of the diagonal elements of the Hessian. It can



then be shown that the relative magnitude of these corrections compared to the Lennard-Jones contribution to the Hessian is of order  $(\sigma/r_c)^5 \ll 1$ . Thus, we can be reasonably confident that the normal modes are accurate.

The finite thickness corrections to the slab had only a small effect on the surface tension ( $-0.4$  erg/cm<sup>2</sup>). This makes sense given that the simulated slab was already roughly 3.8 nm wide. The slab was sufficiently thick that it was not “missing” a sizable amount of cohesive energy. Based on the small size of this correction, we can be reasonably confident that the normal modes in the slab system are representative of two isolated surfaces, and are not artificially softened by missing cohesive energy in the bulk of the slab.

### 4.2.2 Crystal-Surface Interface

The surface tension of the crystal against the Hamaker-matched surface was found to be 13.7 erg/cm<sup>2</sup> at 0 K and 2.2 erg/cm<sup>2</sup> at 400 K (Figure 4.7). As expected, the surface tension was considerably lower for the crystal-surface system than the crystal-vacuum system, because the surface provided some cohesive interactions for the slab that the vacuum did not. The slab had a preferred distance from the surface of about 1.6 Å, which is in agreement with the rule of thumb of Israelachvili.<sup>18</sup> Once again, the vibrational free energy was lower for the crystal-surface system than for the bulk crystal.

Surface vibrations for the slab with the Hamaker-matched substrate were not softened as much as for the slab with vacuum. This is evident in Figure 4.8, which visualizes this difference in the normal modes of the bulk and slab systems. The main figure shows the discrete cumulative fraction of normal modes  $F(T)$  below an energy level with temperature  $T$ . Three distinct bands are observed: a low temperature band corresponding to lattice vibrations, a medium temperature band corresponding to the motion of the CH<sub>2</sub> groups, and a high temperature band corresponding to C–H bond stretching. The inset shows a close-up view of the low temperature modes for all three systems. The slab-vacuum curve is shifted to the left, which corresponds to having “softer”

---

#### 4. ATOMISTIC CALCULATION OF INTERFACIAL TENSIONS

---

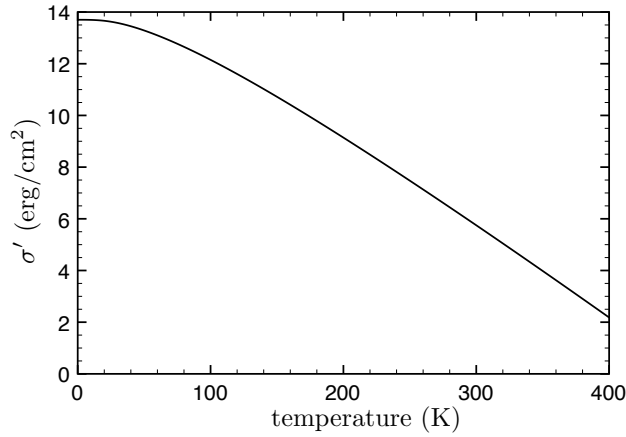


Figure 4.7: Surface tension of  $\alpha_1$  isotactic polypropylene with featureless Hamaker-matched surface extrapolated from 0 K.

modes (modes with lower energy). The slab-surface system is also shifted left from the bulk crystal, but not by as much as the vacuum. At higher temperatures, the curves are not significantly shifted from one another, suggesting that the free energy is lowered mainly by the low frequency lattice modes. Although all modes contribute in principle to the zero-point vibrational free energy, only these low temperature lattice modes are “switched on” in the range of temperatures relevant to crystallization. Thus, it is the differences in these low temperature modes that dominate the reduction in the vibrational free energy of the slab systems versus the bulk crystal.

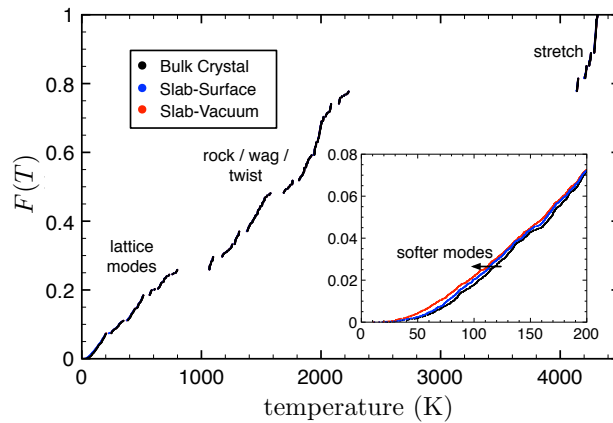


Figure 4.8: Cumulative fraction of normal modes below energy level with temperature  $T$ . Inset shows a closeup of the 0 K to 200 K temperature range, where the phonons for the slab systems are shifted to be “softer”.

#### 4. ATOMISTIC CALCULATION OF INTERFACIAL TENSIONS

---

We have made two key approximations in our calculations of the crystal-surface interfacial tension: (1) the surface is non-vibrating, and (2) the free energy may be extrapolated from 0 K to finite temperature. We would physically expect that the presence of the crystal against the substrate should increase the vibrational free energy of the substrate since its entropy is reduced by surface adsorption. Treating this in simulation would be quite difficult, since it requires exact knowledge of the structure of the substrate. However, in light of our idealization of the substrate as a featureless surface, it is reasonable to approximate the surface as non-vibrating.

Extrapolation of the free energy from the zero-point to finite temperature is a more sensitive issue. As discussed previously, the quasi-harmonic oscillator approximation is reasonably accurate to roughly one-half to two-thirds of the melting point (or about 200 K – 300 K), so some error is introduced at typical crystallization temperatures (400 K) by anharmonic effects. The polypropylene crystal undergoes highly anisotropic thermal expansion at finite temperature, which weakens the cohesive energy and modifies the normal mode frequencies, since they are obtained by Taylor expanding around the potential minimum. A procedure in which the lattice parameters are optimized with respect to the total free energy including vibrations, such as been attempted by Wilhelmi and Rutledge, could remedy this issue. Our present goal is to estimate the contact angle of the crystal nucleus against a surface, and not to obtain precise values for the interfacial tension at finite temperature. We contend that the extrapolation is roughly valid for this purpose.

Moreover, we expect that the zero-point surface tension gives an upper bound, and that the surface tension should in fact decrease with increasing temperature. Although Ross and Frolen fitted a very weak positive temperature dependence of the surface tension, this dependence was obtained by a sensitive fitting procedure with data taken over only a very narrow temperature range,<sup>8</sup> and Hoffman has noted that there is no reason to be particularly confident that this temperature dependence is correct.<sup>19</sup> In fact Hoffman et al originally predicted a decreasing lateral surface tension.<sup>20</sup>

Qualitatively, increasing the temperature has two effects: thermal expansion of the crystal

and an “unfreezing” of high frequency modes. It is well known that materials generally expand on heating, which weakens intermolecular attractions. Both the slab and the bulk crystal should expand, causing both of their potentials to increase. However, on expansion, the missing cohesive energy in the slab should become less “noticeable” to the atoms in the middle, so the difference in potential energy should decrease, lowering the surface tension. Increasing the temperature also causes more vibrations to become significant, which lowers the free energy due to the second term in Eq. 4.2. Vibrations become active once the energy of the quantum oscillator is of order  $kT$ . The slab system has consistently “softer” normal modes (more modes at lower energy). This means that at finite temperature the slab should have more active modes, and thus a lower vibrational free energy. One would expect that the slab would still have softer modes than the bulk even at finite temperature. It can thus be reasonably concluded that the surface tension should decrease with increasing temperature.

### 4.2.3 Contact Angle

With an estimate for the value of  $\sigma'$  at typical crystallization temperatures, we may make an estimate for the contact angle of the crystal nucleus against the Hamaker constant matched surface. From Young’s equation and Figure 4.1

$$\theta = \cos^{-1} \left( \frac{\sigma'' - \sigma'}{\sigma_s} \right) \quad (4.11)$$

where  $\sigma''$  is the interfacial tension between the melt and the surface and  $\sigma_s$  is the interfacial tension of the lateral face of the nucleus. We have previously estimated the value of  $\sigma_s$  to be  $15.9 \pm 3.6$  erg/cm<sup>2</sup>. The interfacial tension  $\sigma''$  between melt and substrate can be estimated theoretically by a lattice-based analytical calculation; here we briefly summarize the approach and quote the numerical result.

Both the melt and the underlying substrate are approximately structureless, Hamaker-matched, and hence nearly enthalpically identical (the small density mismatch contributes roughly

---

#### 4. ATOMISTIC CALCULATION OF INTERFACIAL TENSIONS

---

1 erg/cm<sup>2</sup> to the interfacial tension). Likewise, the contributions from surface phonons to this interfacial free energy are expected to be small, as they were indeed for the crystal against a surface. Unlike the case of a crystal against vacuum, the surface acts to restrain the motion of atoms in the surface layers nearly as much as a continuation of the crystal would have done. The dominant contribution to this interfacial tension is the reduction in entropy of flexible chains near an impenetrable wall.

Roughly speaking, we may say that polymer chains in a bulk melt adopt ideal random-walk configurations; whereas, every monomer in the surface layer adjacent to an uncrossable surface (whether a solid substrate, or an interface with vacuum) must turn back, rather than cross into the forbidden half-space.

To estimate the resulting entropy loss relative to the bulk melt, we consider flexible chains on a cubic lattice. Of the monomers in the surface layer, 5/6 are constrained to step in the plane, while 1/6 are constrained to step into the adjacent melt half-space. (This 1/6 represents the number of walks that on average “arrive from below” in a bulk melt, so that the adjacent melt may adopt ideal random walk statistics.) Thus the entropic cost per unit area is

$$\sigma = \frac{kT}{A_0} (-(5/6) \ln(4/6) - (1/6) \ln(1/6)) = 0.636 \frac{kT}{A_0} \quad (4.12)$$

where  $A_0$  is the placquet area.

We place polypropylene on a cubic lattice by filling each cell with one monomer at melt density; this sets the placquet volume, and hence  $A_0 = 19.9 \text{ \AA}^2$ . At this scale, polypropylene is semiflexible — one monomer can execute a 90-degree turn (with two successive gauche bonds), but with an energy cost. However, it turns out that an analytical approximation to the interfacial tension of semiflexible polymers on a lattice can also be constructed. The bending energy is adjusted so that the end-to-end distance of chains on the lattice matches experiment. For polypropylene, the result is

$$\sigma = 0.367 \frac{kT}{A_0} \approx 10.5 \text{ erg/cm}^2 \quad (4.13)$$

The value is smaller than the flexible result, which is sensible since a stiffer chain tends to run parallel to the interface with less entropic penalty than a flexible chain would suffer. Combining this result with the enthalpic penalty, we estimate a value for  $\sigma''$  of roughly 11.5 erg/cm<sup>2</sup>.

Based on these estimates, we can conclude that at 400 K, the contact angle is roughly  $54^\circ \pm 11^\circ$ . At the zero-point, the contact angle is slightly obtuse ( $\sigma' > \sigma''$ ); however, as previously argued, we reasonably expect that at finite temperature  $\sigma'$  should significantly decrease, and the contact angle should be acute. The estimated value for  $\theta$  is in excellent agreement with the values for the contact angle extracted from experimental data, which ranged from  $40^\circ$  to  $70^\circ$  with a mean of  $56^\circ$ . At the very least, we have shown that the simulated contact angle should be acute, as we have consistently found in our analysis of experimental data.

In our original analysis of experimental data, we assumed that the contact angle was independent of temperature. We obviously expect that the interfacial tensions (and thus the contact angle) should have a temperature dependence. However, over the narrow range of temperatures explored in crystallization experiments, our simulations show that the contact angle is roughly constant, and our approximation is justified.

### 4.3 Conclusion

We have successfully calculated surface tensions of isotactic polypropylene. As Lacks and Rutledge found previously, quantum vibrational free energy contributed significantly due to modification of low frequency modes near the surface. Tail corrections make a significant contribution to the surface tension, but do not much affect the Hessian matrix (and thus vibrational energy) and so can be treated separately from the finite cutoff calculations. We were able to simulate sufficiently large systems that finite slab size effects were not significant.

Modeling of the crystal slab against a Hamaker constant matched surface predicted a contact angle of  $54 \pm 11^\circ$ , which is in excellent agreement with the value previously extracted from experimental data. This provides evidence that the cylindrical cap model for heterogeneous nucle-

#### 4. ATOMISTIC CALCULATION OF INTERFACIAL TENSIONS

---

ation is valid. In future work, the surface tension at finite temperature for different crystal faces may be treated more carefully to assess if the extrapolation from the 0 K structure was justified, and predict more accurate values for the contact angle.

## Bibliography

- [1] C. Silvestre, M. Di Lorenzo, and E. Di Pace, in *Handbook of Polyolefins*, 2nd ed., edited by C. Vasile (Taylor & Francis, New York, 2000), Chap. 9.
- [2] D. Lacks and G. Rutledge, *J. Phys. Chem.* **98**, 1222 (1994).
- [3] D. Lacks and G. Rutledge, *Macromolecules* **28**, 1115 (1995).
- [4] D. Lacks and G. Rutledge, *J. Chem. Phys.* **101**, 9961 (1994).
- [5] J. L. Wilhelmi and G. C. Rutledge, *J. Phys. Chem.* **100**, 10689 (1996).
- [6] W. Haynes, D. Lide, and T. Bruno, *CRC Handbook of Chemistry and Physics*, 93rd ed. (CRC Press, New York, 2012).
- [7] J. Brandrup, E. Immergut, and E. Grulke, *Polymer Handbook*, 4th ed. (Wiley-Interscience, New York, 2003).
- [8] G. Ross and L. Frolen, *J. Res. Natl. Bur. Stand., Sect. A* **79A**, 701 (1975).
- [9] B. Hess, C. Kutzner, D. van der Spoel, and E. Lindahl, *J. Chem. Theory Comput.* **4**, 435 (2008).
- [10] W. Jorgensen, D. Maxwell, and J. Tirado-Rives, *J. Am. Chem. Soc.* **118**, 11225 (1996).
- [11] D. Frenkel and B. Smit, in *Understanding Molecular Simulation*, 2nd ed. (Academic Press, New York, 2001), Chap. 3, pp. 36–37.
- [12] G. Natta and P. Corradini, *Il Nuovo Cimento* **15**, 40 (1960).
- [13] M. Hirose, T. Yamamoto, and M. Naiki, *Comput. Theor. Polym. Sci.* **10**, 345 (2000).
- [14] D. Ferro, S. Brückner, S. Meille, and M. Ragazzi, *Macromolecules* **25**, 5231 (1992).



- [15] P. Corradini, V. Petraccone, and B. Pirozzi, *Eur. Polym. J.* **19**, 299 (1983).
- [16] U. Essmann *et al.*, *J. Chem. Phys.* **103**, 8577 (1995).
- [17] G. Bussi, D. Donadio, and M. Parrinello, *J. Chem. Phys.* **126**, 014101 (2007).
- [18] J. Israelachvili, in *Intermolecular and Surface Forces*, 2nd ed. (Academic Press, Amsterdam, 1992), Chap. 11.
- [19] J. Hoffman, G. Davis, and J. Lauritzen, in *Treatise on Solid State Chemistry*, edited by N. Hannay (Plenum, New York, 1976), Vol. 3, Chap. 7.
- [20] J. Hoffman *et al.*, *Kolloid Z. Z. Polym.* **231**, 564 (1969).

## Shear flow solution to Rouse model

From Eq. 2.7, the Rouse equations are

$$\zeta Y_p' = -K_p Y_p + y_p \quad (\text{A.1a})$$

$$\zeta X_p' = -K_p X_p + x_p + \dot{\gamma} Y_p \quad (\text{A.1b})$$

Rearranging and letting  $\omega_p = K_p/\zeta$  gives a coupled system of ODEs

$$Y_p' = -\omega_p Y_p + \frac{1}{\zeta} y_p \quad (\text{A.2a})$$

$$X_p' = -\omega_p X_p + \frac{1}{\zeta} x_p + \frac{\dot{\gamma}}{\zeta} Y_p \quad (\text{A.2b})$$

Note that  $X_p$  is coupled to  $Y_p$ , but  $Y_p$  is independent.

The solution for  $Y_p$  over the finite time interval  $\Delta t = t_1 - t_0$  is a simple integrating factor problem, with  $\mu = \exp(\omega_p t)$

$$Y_p(t_1) = Y_p(t_0) e^{-\omega_p \Delta t} + \frac{1}{\zeta} \int_{t_0}^{t_1} e^{\omega_p(t-t_1)} y_p(t) dt \quad (\text{A.3})$$

$$= e^{-\omega_p \Delta t} Y_p(t_0) + \Delta Y_p \quad (\text{A.4})$$

Since  $\Delta Y_p$  is the integral over Gaussian random variables with zero mean, it is itself a Gaussian random variable with zero mean.

Solution for  $X_p$  begins with the same integrating factor to give

$$X_p(t_1) = X_p(t_0) e^{-\omega_p \Delta t} + \frac{1}{\zeta} \int_{t_0}^{t_1} e^{\omega_p(t-t_1)} x_p(t) dt + \frac{\dot{\gamma}}{\zeta} \int_{t_0}^{t_1} e^{\omega_p(t-t_1)} Y_p(t) dt \quad (\text{A.5})$$

This solution is similar to Eq. A.3, except for the coupled integral over  $Y_p$ . Considering only this

term, and substituting Eq. A.3 gives

$$\frac{\dot{\gamma}}{\zeta} \int_{t_0}^{t_1} e^{\omega_p(t-t_1)} \left[ Y_p(t_0) e^{\omega_p(t_0-t)} + \frac{1}{\zeta} \int_{t_0}^t e^{\omega_p(t'-t)} y_p(t') dt' \right] dt \quad (\text{A.6})$$

Simplifying the integrals and exponentials

$$\frac{\dot{\gamma}}{\zeta} e^{\omega_p(t_0-t_1)} Y_p(t_0) \int_{t_0}^{t_1} dt + \frac{\dot{\gamma}}{\zeta^2} \int_{t_0}^{t_1} e^{\omega_p(t-t_1)} \int_{t_0}^t e^{\omega_p(t'-t)} y_p(t') dt' dt \quad (\text{A.7})$$

$$= \frac{\dot{\gamma} \Delta t}{\zeta} e^{-\omega_p \Delta t} Y_p(t_0) + \frac{\dot{\gamma}}{\zeta^2} \int_{t_0}^{t_1} \int_{t_0}^t e^{\omega_p(t'-t_1)} y_p(t') dt' dt \quad (\text{A.8})$$

The twice-repeated integral can be simplified with the Cauchy formula with  $n = 2$

$$\frac{\dot{\gamma} \Delta t}{\zeta} e^{-\omega_p \Delta t} Y_p(t_0) + \frac{\dot{\gamma}}{\zeta^2} \frac{1}{(2-1)!} \int_{t_0}^{t_1} (t_1 - t)^{2-1} e^{\omega_p(t-t_1)} y_p(t) dt \quad (\text{A.9})$$

The final update formula for  $X_p$  is given as

$$\begin{aligned} X_p(t_1) &= X_p(t_0) e^{-\omega_p \Delta t} + \frac{1}{\zeta} \int_{t_0}^{t_1} e^{\omega_p(t-t_1)} x_p(t) dt \\ &\quad + \frac{\dot{\gamma} \Delta t}{\zeta} e^{-\omega_p \Delta t} Y_p(t_0) + \frac{\dot{\gamma}}{\zeta^2} \int_{t_0}^{t_1} (t_1 - t) e^{\omega_p(t-t_1)} y_p(t) dt \end{aligned} \quad (\text{A.10})$$

$$= e^{-\omega_p \Delta t} \left( X_p(t_0) + \frac{\dot{\gamma} \Delta t}{\zeta} Y_p(t_0) \right) + \Delta X_p^{(x)} + \frac{\dot{\gamma}}{\zeta} \Delta X_p^{(y)} \quad (\text{A.11})$$

It is apparent that  $\Delta X_p^{(x)}$  is an independent Gaussian variable with variance analogous to  $\Delta Y_p$ . However,  $\Delta Y_p$  and  $\Delta X_p^{(y)}$  are correlated Gaussian variables since they both depend on  $y_p(t)$ . Thus,  $\langle \Delta Y_p^2 \rangle = \langle \Delta X_p^{(x)2} \rangle$ ,  $\langle \Delta X_p^{(y)2} \rangle$ , and  $\langle \Delta Y_p \Delta X_p^{(y)} \rangle$  must be computed to generate appropriate representative Gaussian variables for the integrals.

Starting with  $\langle \Delta Y_p^2 \rangle$ ,

$$\langle \Delta Y_p^2 \rangle = \frac{1}{\zeta^2} \int_{t_0}^{t_1} \int_{t_0}^{t_1} e^{-2\omega_p(t-t_1)} \langle y_p(t) y_p(t') \rangle dt dt' \quad (\text{A.12})$$

We can substitute Eq. 2.5 for  $\langle y_p(t)y_p(t) \rangle$  to obtain

$$\langle \Delta Y_p^2 \rangle = \frac{1}{\zeta^2} \int_{t_0}^{t_1} e^{2\omega_p(t-t_1)} \int_{t_0}^{t_1} \left[ \frac{4\zeta}{\beta n} \delta_{pq} \delta(t-t') \right] dt dt' \quad (\text{A.13})$$

$$= \frac{1}{\zeta^2} \int_{t_0}^{t_1} e^{2\omega_p(t-t_1)} \left( \frac{4\zeta}{\beta n} \right) dt \quad (\text{A.14})$$

$$= \frac{4}{\zeta \beta n} \frac{v_0(2\omega_p \Delta t)}{2\omega_p} \quad (\text{A.15})$$

where  $v_0(x) = 1 - \exp(-x)$ . This result applies analogously to  $\langle \Delta X_p^{(x)^2} \rangle$ .

Proceeding as in Eq. A.12 for  $\langle \Delta X_p^{(y)^2} \rangle$

$$\langle \Delta X_p^{(y)^2} \rangle = \frac{1}{\zeta^2} \int_{t_0}^{t_1} \int_{t_0}^{t_1} (t_1 - t)^2 e^{2\omega_p(t-t_1)} \langle y_p(t)y_p(t) \rangle dt dt' \quad (\text{A.16})$$

which may be simplified as before with Eq. 2.5 to give

$$\langle \Delta X_p^{(y)^2} \rangle = \frac{4}{\zeta \beta n} \int_{t_0}^{t_1} (t_1 - t)^2 e^{2\omega_p(t-t_1)} dt \quad (\text{A.17})$$

$$= \frac{4}{\zeta \beta n} \frac{v_1(2\omega_p \Delta t)}{8\omega_p^3} \quad (\text{A.18})$$

where  $v_1(x) = 2 - (2 + 2x + x^2) \exp(-x)$ .

Finally, the correlation term is computed

$$\langle \Delta Y_p \Delta X_p^{(y)} \rangle = \frac{1}{\zeta^2} \int_{t_0}^{t_1} \int_{t_0}^{t_1} (t_1 - t) e^{2\omega_p(t-t_1)} \langle y_p(t)y_p(t) \rangle dt dt' \quad (\text{A.19})$$

which simplifies as before

$$\langle \Delta Y_p \Delta X_p^{(y)} \rangle = \frac{4}{\zeta \beta n} \int_{t_0}^{t_1} (t_1 - t) e^{2\omega_p(t-t_1)} dt \quad (\text{A.20})$$

$$= \frac{4}{\zeta \beta n} \frac{v_2(2\omega_p \Delta t)}{4\omega_p^2} \quad (\text{A.21})$$

## A. SHEAR FLOW SOLUTION TO ROUSE MODEL

---

where  $v_2(x) = 1 - (1 + x)\exp(-x)$ .

## Discretization of shear flow solution

Discretize the operators forward in time, and with a central-difference with respect to space. Then,  $\mathbf{R}(s, t)$  is discretized into  $\mathbf{R}_{s,t}$  for integer values of  $s$  and  $t$ . We take the discrete Fourier transform as

$$\mathbf{X}_s = \frac{2}{N} \sum_{r=1}^N \mathbf{R}_r \cos\left(\frac{\pi}{N}(r-1/2)(s-1)\right) \quad (\text{B.1})$$

where  $\mathbf{X}_s = \langle X_s, Y_s \rangle$ , and  $r$  and  $s$  range from 1 to  $N$ . The inverse of this transform is given as

$$\mathbf{R}_s = \frac{\mathbf{X}_1}{2} + \sum_{r=2}^N \mathbf{X}_r \cos\left(\frac{\pi}{N}(r-1)(s-1/2)\right) \quad (\text{B.2})$$

Given this transform, it can be shown that the eigenvalues become

$$\lambda_s = 4 \sin^2\left(\frac{\pi}{2N}(s-1)\right) \quad (\text{B.3})$$

The center of mass of the chain can be fixed at the origin by forcing  $\mathbf{X}_1 = \mathbf{0}$ .

We choose this form of the FFT because Eq. B.1 and Eq. B.2 are the discrete analogs of Eq. 2.4 and Eq. 2.3, respectively. Given this convention for the FFT, the discrete noise variance is

$$\langle x_p(t_i) x_q(t_j) \rangle = \frac{4\zeta}{\beta} \frac{\delta_{ij}}{\Delta} \frac{\delta_{pq}}{n} \quad (\text{B.4})$$

with  $\Delta$  the fundamental step. This is the discrete analog of Eq. 2.5.

Letting  $\omega_s = (K/\zeta)\lambda_s$ , the discrete update formula for  $Y_s$  becomes

$$Y_s(t+k\Delta) = (1 - \omega_s \Delta)^k Y_s(t) + \frac{\Delta}{\zeta} \sum_{i=1}^k (1 - \omega_s \Delta)^{i-1} y_p(t + (k-i)\Delta) \quad (\text{B.5})$$

where  $\Delta$  is the fundamental time step, and  $y_p(t + (k-i)\Delta)$  is an entry in the noise history. Likewise,

it can be shown that the update formula for  $X_s$  is

$$\begin{aligned}
X_s(t + k\Delta) &= (1 - \omega_s \Delta)^k X_s(t) + \frac{\dot{\gamma} \Delta}{\zeta^2} (1 - \omega_s \Delta)^{k-1} Y_p(t) \\
&\quad + \frac{\Delta}{\zeta} \sum_{i=1}^k (1 - \omega_s \Delta)^{i-1} x_p(t + (k-i)\Delta) \\
&\quad + \frac{\dot{\gamma} \Delta^2}{\zeta^2} \sum_{i=2}^k (i-1) (1 - \omega_s \Delta)^{i-1} y_p(t + (k-i)\Delta)
\end{aligned} \tag{B.6}$$

## Mixed flow solution to Rouse model

From Eq. 2.13 in Section 2.1.2 and letting  $\omega_p = K_p/\zeta$ ,

$$\begin{aligned} \begin{pmatrix} \dot{X}_p \\ \dot{Y}_p \end{pmatrix} &= \begin{pmatrix} -\omega_p & \dot{\gamma}/\zeta \\ \dot{\gamma}\beta/\zeta & -\omega_p \end{pmatrix} \begin{pmatrix} X_p \\ Y_p \end{pmatrix} + \frac{1}{\zeta} \begin{pmatrix} x_p \\ y_p \end{pmatrix} \\ &\equiv \mathbf{M} \begin{pmatrix} X_p \\ Y_p \end{pmatrix} + \frac{1}{\zeta} \begin{pmatrix} x_p \\ y_p \end{pmatrix} \end{aligned} \quad (\text{C.1})$$

The eigenvalues of the matrix  $\mathbf{M}$  are

$$\lambda_{1,2} = -\omega_p \pm \frac{\dot{\gamma}\sqrt{\beta}}{\zeta} \quad (\text{C.2})$$

It is apparent that  $\lambda_2$  is always negative, and that  $\lambda_1$  may be negative, positive, or zero depending on the relative magnitudes of  $\omega_p, \dot{\gamma}, \beta$ , and  $\zeta$ . The corresponding eigenvectors are  $(1, \sqrt{\beta})$  and  $(1, -\sqrt{\beta})$ . For non-shear flow ( $\beta \neq 0$ ), the eigenvectors are linearly independent, and  $\mathbf{M}$  is diagonalizable.

Let  $\Lambda$  be the diagonal matrix of eigenvalues, and  $\mathbf{T} = [\mathbf{e}_1, \mathbf{e}_2]$  the matrix with corresponding eigenvectors as its columns. Diagonalizing Eq. C.1 gives

$$\tilde{\mathbf{S}}' = \Lambda \tilde{\mathbf{S}} + \frac{1}{\zeta} \tilde{\mathbf{B}} \quad (\text{C.3})$$

where

$$\tilde{\mathbf{S}} = \begin{pmatrix} \tilde{X}_p \\ \tilde{Y}_p \end{pmatrix} = \mathbf{T}^{-1} \begin{pmatrix} X_p \\ Y_p \end{pmatrix} \quad (\text{C.4})$$

and

$$\tilde{\mathbf{B}} = \begin{pmatrix} \tilde{x}_p \\ \tilde{y}_p \end{pmatrix} = \mathbf{T}^{-1} \begin{pmatrix} x_p \\ y_p \end{pmatrix} \quad (\text{C.5})$$



Then, we readily arrive at Eq. 2.14 from Section 2.1.2

$$\tilde{X}'_p = \lambda_1 \tilde{X}_p + \frac{1}{\zeta} \tilde{x}_p \quad (\text{C.6a})$$

$$\tilde{Y}'_p = \lambda_2 \tilde{Y}_p + \frac{1}{\zeta} \tilde{y}_p \quad (\text{C.6b})$$

which is easily solved over the finite interval  $\Delta t = t_1 - t_0$  by an integrating factor  $\mu = \exp(-\lambda t)$  to give

$$\tilde{X}_p(t_1) = e^{\lambda_1 \Delta t} \tilde{X}_p(t_0) + \frac{1}{\zeta} \int_{t_0}^{t_1} e^{-\lambda_1(t-t_1)} \tilde{x}_p(t) dt \quad (\text{C.7})$$

$$= e^{\lambda_1 \Delta t} \tilde{X}_p(t_0) + \Delta \tilde{X}_p \quad (\text{C.8})$$

and likewise for  $\tilde{Y}_p$

$$\tilde{Y}_p(t_1) = e^{\lambda_2 \Delta t} \tilde{Y}_p(t_0) + \frac{1}{\zeta} \int_{t_0}^{t_1} e^{-\lambda_2(t-t_1)} \tilde{y}_p(t) dt \quad (\text{C.9})$$

$$= e^{\lambda_2 \Delta t} \tilde{Y}_p(t_0) + \Delta \tilde{Y}_p \quad (\text{C.10})$$

Observe that since  $\tilde{x}_p$  and  $\tilde{y}_p$  are linear combinations of Gaussian random variables  $x_p$  and  $y_p$ ,  $\Delta \tilde{X}_p$  and  $\Delta \tilde{Y}_p$  are correlated Gaussian random variables. We must then compute the variances  $\langle \Delta \tilde{Y}_p^2 \rangle$ ,  $\langle \Delta \tilde{X}_p^2 \rangle$ , and  $\langle \Delta \tilde{X}_p \Delta \tilde{Y}_p \rangle$ .

Proceeding for  $\langle \Delta \tilde{Y}_p^2 \rangle$  as in Appendix A, we obtain

$$\langle \Delta \tilde{Y}_p^2 \rangle = \frac{1}{\zeta^2} \int_{t_0}^{t_1} \int_{t_0}^{t_1} e^{-2\lambda_2(t-t_1)} \langle \tilde{y}_p(t) \tilde{y}_p(t) \rangle dt dt \quad (\text{C.11})$$

From Eq. C.5 we know that  $\tilde{y}_p(t) = (1/2)(x_p(t) - y_p(t)/\sqrt{\beta})$ , so Eq. C.11 becomes

$$\langle \Delta \tilde{Y}_p^2 \rangle = \frac{1}{\zeta^2} \int_{t_0}^{t_1} e^{-2\lambda_2(t-t_1)} \int_{t_0}^{t_1} \left\langle \frac{1}{4} \left( x_p(t) - \frac{y_p(t)}{\sqrt{\beta}} \right)^2 \right\rangle dt dt \quad (C.12)$$

$$= \frac{1}{\zeta^2} \int_{t_0}^{t_1} e^{-2\lambda_2(t-t_1)} \int_{t_0}^{t_1} \left\langle \frac{1}{4} \left( x_p(t)^2 - \frac{2}{\sqrt{\beta}} x_p(t) y_p(t) + \frac{y_p(t)^2}{\beta} \right) \right\rangle dt dt \quad (C.13)$$

Since  $x_p(t)$  and  $y_p(t)$  are uncorrelated, the cross term can be eliminated from the average. Substituting from Eq. 2.5, and integrating twice gives the variance expression

$$\langle \Delta \tilde{Y}_p^2 \rangle = \frac{\beta + 1}{2n\beta_0 \zeta \beta \lambda_2} (e^{2\lambda_2 \Delta t} - 1) \quad (C.14)$$

where  $\beta_0$  is  $1/(kT)$ .

Solution for  $\langle \Delta \tilde{X}_p^2 \rangle$  proceeds similarly, with  $\tilde{x}_p(t) = (1/2)(x_p(t) + y_p(t)/\sqrt{\beta})$ , to give

$$\langle \Delta \tilde{X}_p^2 \rangle = \frac{\beta + 1}{2n\beta_0 \zeta \beta \lambda_1} (e^{2\lambda_1 \Delta t} - 1) \quad (C.15)$$

when  $\lambda_1 \neq 0$ . If  $\lambda_1 = 0$ , the solution simplifies to

$$\langle \Delta \tilde{X}_p^2 \rangle = \frac{\beta + 1}{n\beta_0 \zeta \beta} \Delta t \quad (C.16)$$

Finally, computing  $\langle \Delta \tilde{X}_p \Delta \tilde{Y}_p \rangle$  gives

$$\langle \Delta \tilde{X}_p \Delta \tilde{Y}_p \rangle = \frac{1}{\zeta^2} \int_{t_0}^{t_1} \int_{t_0}^{t_1} e^{-(\lambda_1 + \lambda_2)(t-t_1)} \langle \tilde{x}_p(t) \tilde{y}_p(t) \rangle dt dt \quad (C.17)$$

The product  $\tilde{x}_p(t) \tilde{y}_p(t)$  is a difference of squares, simplifying to

$$\langle \Delta \tilde{X}_p \Delta \tilde{Y}_p \rangle = \frac{1}{\zeta^2} \int_{t_0}^{t_1} e^{-(\lambda_1 + \lambda_2)(t-t_1)} \int_{t_0}^{t_1} \left\langle \frac{1}{4} \left( x_p(t)^2 - \frac{y_p(t)^2}{\beta} \right) \right\rangle dt dt \quad (C.18)$$

---

### C. MIXED FLOW SOLUTION TO ROUSE MODEL

---

which may be reduced with Eq. 2.5 and twice integrated as before to give

$$\langle \Delta \tilde{X}_p \Delta \tilde{Y}_p \rangle = \frac{\beta - 1}{n\beta_0 \zeta \beta (\lambda_1 + \lambda_2)} (e^{(\lambda_1 + \lambda_2)\Delta t} - 1) \quad (\text{C.19})$$

This may be further simplified by observing that  $\lambda_1$  and  $\lambda_2$  are conjugates

$$\langle \Delta \tilde{X}_p \Delta \tilde{Y}_p \rangle = \frac{\beta - 1}{2n\beta_0 \zeta \beta \omega_p} (e^{-2\omega_p \Delta t} - 1) \quad (\text{C.20})$$

It should be noted that  $\Delta \tilde{X}_p$  and  $\Delta \tilde{Y}_p$  become totally uncorrelated if  $\beta = 1$ , the case of pure extensional flow.

## Correlated random values

We need to generate two correlated Gaussian random variables  $x$  and  $y$  with zero mean. We want these variables to have a covariance matrix  $\mathbf{M}$  such that

$$\mathbf{M} = \begin{pmatrix} \sigma_{xx}^2 & \sigma_{xy}^2 \\ \sigma_{yx}^2 & \sigma_{yy}^2 \end{pmatrix} \quad (\text{D.1})$$

where  $\sigma_{xx}^2 = \langle x^2 \rangle$ ,  $\sigma_{yy}^2 = \langle y^2 \rangle$ , and  $\sigma_{xy}^2 = \sigma_{yx}^2 = \langle xy \rangle$ .

The covariance matrix has a generating function

$$Z \propto \int \exp \left( -\frac{1}{2} \mathbf{v}^T \cdot \mathbf{M}^{-1} \cdot \mathbf{v} + \mathbf{h}^T \cdot \mathbf{v} \right) d\mathbf{v} \propto \exp \left( \frac{1}{2} \mathbf{h}^T \cdot \mathbf{M} \cdot \mathbf{h} \right) \quad (\text{D.2})$$

where  $\mathbf{v}$  is the vector of correlated variables, and  $\mathbf{h}$  is a conjugate variable.

Since it is our objective to obtain  $\mathbf{v}$ , and  $\mathbf{M}^{-1}$  is not diagonal, we need to make a change of variables to  $\mathbf{v}$  that allows us to generate independent Gaussian random variables with appropriate variances, and correlate them as a linear combination.

Since the matrix  $\mathbf{M}$  is symmetric positive definite,  $\mathbf{M}^{-1}$  has a complete basis of eigenvectors. Thus,  $\mathbf{M}^{-1}$  is diagonalizable, and

$$\mathbf{M}^{-1} \cdot \mathbf{T} = \Lambda \cdot \mathbf{T} \quad (\text{D.3})$$

where  $\Lambda$  is the diagonal matrix of eigenvalues, and  $\mathbf{T}$  is the matrix of eigenvectors,  $[\mathbf{e}_1, \mathbf{e}_2]$ . We can then expand  $\mathbf{v}$  in the eigenvector basis as

$$\mathbf{v} = \mathbf{T} \cdot \mathbf{a} \quad (\text{D.4})$$

Since  $\mathbf{M}^{-1}$  is a symmetric positive definite matrix, its eigenvectors are orthonormal such that

---

#### D. CORRELATED RANDOM VALUES

---

$\mathbf{T}^T \cdot \mathbf{T} = \mathbf{I}$ . Combining this result with Eq. D.3 and Eq. D.4, we obtain

$$\mathbf{v}^T \cdot \mathbf{M}^{-1} \cdot \mathbf{v} = \mathbf{a}^T \cdot \Lambda \cdot \mathbf{a} \quad (\text{D.5})$$

where  $\mathbf{a}$  is a vector of independent Gaussian random variables with zero mean, and with variances such that  $\langle a_i^2 \rangle = 1/\Lambda_i$ .

The vector of correlated Gaussian random variables may be recovered by generating a representative vector  $\mathbf{a}$  of independent Gaussian random variables, and then taking  $\mathbf{v} = \mathbf{T} \cdot \mathbf{a}$ .

## Convergence order analysis

Although a treatment of weak convergence for stochastic differential equations as applied to operator splitting can be found in Ref. 1 (with essential background materials in Ref. 2), as a convenience to the reader we briefly summarize in this appendix the basic elements of this analysis.

The starting point for developing methods for stochastic DEs is the Ito equation, which in differential form (for additive noise) is

$$dX = a(X)dt + b dW \quad (\text{E.1})$$

and in integral form is

$$X(t) = X_0 + \int_0^t dt' a(X(t')) + b \int_0^t dW(t') \quad (\text{E.2})$$

In the above,  $W(t)$  is a Wiener process, i.e.,  $dW(t)$  is delta-correlated white noise. The noise integral  $W(t) = \int_0^t dW(t')$  executes a Gaussian random walk, with  $\langle W(t) \rangle = 0$  and  $\langle W^2(t) \rangle = t$ . Eq. E.1 is quite general:  $X$  can denote a single variable or a vector of values,  $a(X)$  can be any function (linear or nonlinear) of  $X$ .

To resolve ambiguities involving averages over the noise  $dW(t)$ , it is helpful to regard the time  $t$  as discrete, with timestep  $\Delta t$ :

$$X_{i+1} = X_i + a(X_i)\Delta t + b\Delta W_i \quad (\text{E.3})$$

with noise  $\Delta W_i$  a sequence of uncorrelated random steps, of magnitude  $\pm\sqrt{\Delta t}$ . The discretized equation is causal, since  $X$  at the “next” time  $X_{i+1}$  depends only on the “present”  $X_i$  and noise  $\Delta W_i$ . Also, it is straightforward to average over such discretized noise.

Suppose we have some function  $g(X(t), t)$  of our stochastic process  $X(t)$ , and want to know how  $g$  itself varies over some short time interval  $dt$ . The Ito formula, essentially the chain rule for

stochastic processes, expands  $g$  about its value at time  $t$  as

$$dg = \frac{\partial g}{\partial t} dt + \frac{\partial g}{\partial X} (a(X)dt + b dW) + \frac{1}{2} \frac{\partial^2 g}{\partial X^2} b^2 dt \quad (\text{E.4})$$

In integral form, the relation reads

$$g(X(t)) = g(X(0)) + \int_0^t dt' (a(X(t'))g'(X(t')) + (1/2)b^2 g''(X(t'))) + b \int_0^t dW(t') \quad (\text{E.5})$$

in which  $g'$  denotes  $\partial g / \partial X$ , and for simplicity we have dropped explicit time-dependence (i.e.,  $\partial g / \partial t = 0$ ).

The formal solution Eq. E.2 can be expanded by repeatedly replacing  $a(X(t'))$  and its derivatives using Eq. E.5, to obtain the Ito-Taylor expansion,

$$X(t) = X(0) + aI_{(0)} + bI_{(1)} + \left(a'a + \frac{1}{2}a''b^2\right)I_{(0,0)} + a'bI_{(1,0)} + a''b^2I_{(1,1,0)} + \dots \quad (\text{E.6})$$

in which  $a$  and its derivatives are all evaluated at the initial condition  $X = X_0$ . Also,  $I_{(i,j,k,\dots)}$  with  $i, j, k, \dots = 0$  or  $1$  denote various integrals over the noise,

$$I_{(i_1, i_2, \dots, i_n)} = \int_0^t dW^{i_n}(s_n) \int_0^{s_n} dW^{i_{n-1}}(s_{n-1}) \int_0^{s_{n-1}} \dots \int_0^{s_2} dW^{i_1}(s_1) \quad (\text{E.7})$$

Dropping the noise ( $b = 0$ ) gives the Taylor expansion of the deterministic equation  $dX = a(X)dt$ .

It is useful to assign to each of the various noise integrals  $I_{(i,j,k,\dots)}$  a scaling power of the time interval  $\Delta$ . Each integral with a  $dW$  implies a factor  $\Delta^{1/2}$  (since the variance of  $\int dW$  is of order  $\Delta$ ) and each integral without a  $dW$  a factor  $\Delta$ . Terms  $I_{(0)}$  and  $I_{(0,0)}$  are deterministic, given by  $I_{(0)} = \Delta$  and  $I_{(0,0)} = \Delta^2/2$  respectively. In what follows, we scale the noise integrals by appropriate factors of  $\Delta$  to make power-counting explicit.

We are interested in the weak and strong convergence properties of two approximate methods, explicit Euler and operator splitting. The integral form of the Euler method over the time

interval from  $t = 0$  to  $t = \Delta$  is

$$X_1 = X_0 + \Delta a(X_0) + b \int_0^\Delta dW(t') \quad (\text{E.8})$$

in which  $X_0$  is the initial condition  $X(0)$  and  $X_1$  the final value  $X(\Delta)$ .

Symmetric stochastic splitting is defined (see main text) by alternating between exact solutions with one of two partial time evolution operators  $a_1(X)$  and  $a_2(X)$ :

$$\begin{aligned} X_1 &= X_0 + \int_0^{\Delta/2} a_2(X_1(t')) dt' \\ X_2 &= X_1 + \int_0^\Delta a_1(X_2(t')) dt' + b \int_0^\Delta dW(t') \\ X_3 &= X_2 + \int_0^{\Delta/2} a_2(X_3(t')) dt' \end{aligned} \quad (\text{E.9})$$

in which  $X_3$  is the final value  $X(\Delta)$ .

To determine strong convergence order, we simply compare the Ito-Taylor expansions of the approximate solutions to the true expansion, Eq. E.6. The Ito-Taylor expansion for the Euler method is obvious from Eq. E.8,

$$X(t + \Delta) = X(t) + \Delta a(X(t)) + b\Delta^{1/2}I_{(1)} \quad (\text{E.10})$$

and agrees with Eq. E.6 through terms of order  $O(\Delta)$ , hence we say the method is of strong order 1.0.

The Ito-Taylor expansion for the operator splitting method is obtained by using the full Taylor expansion (with  $a = a_2$ ) to describe the “outer” deterministic steps, and the full Ito-Taylor expansion (with  $a = a_1$ ) to describe “inner” stochastic step. The result of each step serves as the



initial condition for the next, so the expansions are nested, with the final result

$$\begin{aligned} X(t + \Delta) = & X(t) + \Delta(a_1 + a_2) + b\Delta^{3/2}I_{(1)} + b\Delta^{3/2}(a'_1I_{(1,0)} + (1/2)a'_2I_{(1)}) \\ & + (1/4)\Delta^2(2(a_1 + a_2)(a'_1 + a'_2) + b^2a''_1 + 4b^2a'_1I_{(1,1,0)} + b^2a'_2I_{(1)}) + \dots \end{aligned} \quad (\text{E.11})$$

The above agrees with Eq. E.6 only through order  $O(\Delta)$ , so is of strong order 1.0 as well.

We now sketch a proof of the criterion for weak convergence, defined as follows. (See Ref. 2 p. 474, Theorem 14.5.2, Eq. 5.12 for details.) Suppose we have some smooth function  $g(X)$  that we want to average over trajectories, given a definite starting point  $X_0$  at time  $t_0$ . Weak convergence means the average computed with approximate dynamics approaches the true average, as the time difference  $\Delta$  becomes small:

$$\langle g(X(t)) | X_0 \rangle_{true} - \langle g(X(t)) | X_0 \rangle_{approx} = O(\Delta^{\beta+1}) \quad (\text{E.12})$$

where  $\beta$  is the weak order of convergence.

Note that if we have a finite time difference  $t_{max} - t_0$ , then the number of small timesteps  $\Delta$  needed is  $n = (t_{max} - t_0)/\Delta$ . Since error accumulates on each timestep, the total error in the average is of order  $O(\Delta^\beta)$ .

The “weak order  $\beta$ ” notation is consistent with nomenclature for strong convergence, for which a “strong order  $\alpha$ ” method means agreement of the Ito-Taylor expansions of the true and approximate dynamics *through* order  $O(\Delta^\alpha)$  for a *single* step, and therefore an error for a finite timestep  $t_{max} - t_0$  of order  $O(\Delta^\alpha)$ .

Since the timestep  $\Delta$  is small,  $X(t)$  does not stray very far from  $X_0$ . This motivates us to expand  $g(X(t))$  as

$$g(X(t)) = g(X_0) + g'(X_0)(X(t) - X_0) + (1/2)g''(X_0)(X(t) - X_0)^2 + \dots \quad (\text{E.13})$$

Evaluating the averages in Eq. E.12 then reduces to evaluating the averages of moments of the true and approximate evolution of  $X(t)$ , defined as

$$M_k(\Delta t) = \langle (X(\Delta t) - X_0)^k \rangle \quad (\text{E.14})$$

for the exact and approximate evolutions.

How high a moment must we examine, to verify Eq. E.12 for some given  $\beta$ ? Note that the Ito-Taylor expansion for  $X(t)$  begins

$$X(t) - X_0 = a(X_0)\Delta + b \int_0^t dW(t') + \dots \quad (\text{E.15})$$

To find the largest contribution to  $\langle (X(t) - X_0)^k \rangle$ , we take as many powers of noise as possible, since the noise scales as  $\Delta^{1/2}$ . (We need an even number of factors of the noise, so that the average does not vanish.)

As we consider higher moments, eventually even the lowest order contribution will be higher order than  $\Delta^{\beta+1}$ . Evidently,  $k = 2\beta$  can generate terms of order  $\Delta^\beta$ . Therefore, we need to compare the real and approximate dynamics up through the  $2\beta$ th moment, to verify weak convergence of order  $\beta$ . (The average of a term with  $k = 2\beta + 1$  powers of noise will vanish, since this  $k$  is odd, hence the error in the noise moments will be  $O(\Delta^{\beta+1})$ .)

Since the moments to be compared are to be computed for small  $\Delta$ , we use the Ito-Taylor expansions for the true and approximate solutions, together with a set of results for averaging various products of noise integrals. The results we need to sufficient order for present purposes are

$$\begin{aligned} \langle I_{(1)}^2 \rangle &= 1 \\ \langle I_{(1)}^4 \rangle &= 3 \\ \langle I_{(1)} I_{(1,0)} \rangle &= 1/2 \\ \langle I_{(1,0)}^2 \rangle &= 1/3 \end{aligned} \quad (\text{E.16})$$

---

## E. CONVERGENCE ORDER ANALYSIS

---

Any averages of noise integrals in which a given noise increment  $dW(t)$  appears with an odd power, will vanish, so that  $\langle I_{(1)} \rangle$ ,  $\langle I_{(1,0)} \rangle$ ,  $\langle I_{(1)}^3 \rangle$ ,  $\langle I_{(1)} I_{(1,0)}^2 \rangle$ ,  $\langle I_{(1)}^2 I_{(1,0)} \rangle$ , and  $\langle I_{(1)} I_{(1,1,0)} \rangle$  are all zero.

Carrying out moment averages using these methods, we can verify that the explicit Euler method is weak order 1.0, while operator splitting is weak order 2.0.

## Bibliography

- [1] W. Petersen, Siam J Numer Anal **35**, 1439 (1998).
- [2] P. Kloeden and E. Platen, *Numerical Solution of Stochastic Differential Equations (Stochastic Modelling and Applied Probability)* (Springer, Berlin, 2011).

## Derivation of cylindrical cap critical barrier

Suppose there is a “cylindrical cap” well defined by a contact angle  $\theta$ . The cap has two ends with interfacial tension  $\sigma_e$ , a lateral side with  $\sigma_s$ , and also a base against the surface with  $\sigma'$ . The cylinder has a radius  $R$  and critical height  $H$ . We need to find the various surface areas and volume of this cap to take a free energy balance, which we can then maximize. The surface area of an end cap  $A_e$  is

$$\begin{aligned}
 A_e &= A_{\text{sector}} - A_{\text{triangle}} \\
 &= \theta R^2 - R^2 \sin \theta \cos \theta \\
 &= R^2 \left( \theta - \frac{1}{2} \sin 2\theta \right)
 \end{aligned} \tag{F.1}$$

The lateral surface area  $A_s$  is

$$A_s = 2\theta RH \tag{F.2}$$

The area of the nucleus contacting the surface  $A_b$  is a rectangle

$$A_b = 2RH \sin \theta \tag{F.3}$$

Finally, the volume of the nucleus  $V$  is

$$V = A_e H = R^2 H \left( \theta - \frac{1}{2} \sin 2\theta \right) \tag{F.4}$$

Taking a free energy balance

$$\begin{aligned}
\Delta G &= \Delta G_s + \Delta G_e + \Delta G_b - \Delta G_v \\
&= A_s \sigma_s + 2A_e \sigma_e + A_b (\sigma' - \sigma'') - V \Delta S \Delta T \\
&= 2\theta R H \sigma_s + 2R^2 \left( \theta - \frac{1}{2} \sin 2\theta \right) \sigma_e - R H \sigma_s \sin 2\theta \\
&\quad - R^2 H \left( \theta - \frac{1}{2} \sin 2\theta \right) \Delta S \Delta T
\end{aligned} \tag{F.5}$$

in which we have substituted  $-\sigma_s \cos \theta$  for  $(\sigma' - \sigma'')$ , according to Young's equation.

We then differentiate in  $H$  to find the critical radius  $R^*$

$$R^* = \frac{2\sigma_s}{\Delta S \Delta T} \tag{F.6}$$

and then in  $R$  to find  $H^*$

$$H^* = \frac{4\sigma_e}{\Delta S \Delta T} \tag{F.7}$$

which is the same as the critical radius and height for the homogeneous cylinder (note that  $R^*$  and  $H^*$  have no  $\theta$  dependence). Last, substitute back into Eq. F.5 to find the critical barrier  $\Delta G^*$

$$\begin{aligned}
\Delta G^* &= \frac{8\pi\sigma_s^2\sigma_e}{(\Delta S \Delta T)^2} \left( \frac{\theta - \sin(2\theta)/2}{\pi} \right) \\
&= \Delta G_{\text{hom}}^* v(\theta)
\end{aligned} \tag{F.8}$$

## Tail corrections

It is our objective to evaluate the tail correction for material in a slab beyond the volume already accounted for within the cutoff radius  $r_c$

$$\Delta U_{ij} = \frac{\rho_j}{2} \int_{V'_c} U(r_{ij}) d\mathbf{r} \quad (\text{G.1})$$

Since this integral is not simple to evaluate, we will do this by adding and subtracting simpler integrals. Suppose that we have a slab of thickness  $2d$  which is periodic in two dimensions and has gaps in the third dimension. Choose any atom  $i$  in the slab. This atom will have distances  $h_1$  and  $h_2$  to the edge of the slab ( $h_1 \leq h_2$ ). If we assume  $r_c \leq d$ , Figure G.1 shows three possible scenarios for the atom's position. Enforcing that  $r_c \leq d$  somewhat simplifies the problem by guaranteeing that the cutoff sphere does not exit both sides of the slab (a fourth scenario). The optimal choice for  $r_c$  is  $d$  (about 19 Å for our system) since this effectively removes the first scenario; only a marginal number of atoms would fall into the category of being exactly  $d$  from the edge. For all cases, we will follow a general scheme of: (1) adding back a full spherical tail correction as if the system were fully periodic, (2) subtracting for material which is not present in the slab dimension, and (3) adding back any material which was incorrectly subtracted because it lies within the cutoff radius.

For the first case ( $h_1 \geq r_c$ ), Eq. G.1 can be evaluated by taking the full spherical integral, and subtracting the interaction with two semi-infinite half planes in the slab dimension

$$\Delta U_{ij} = U_{\text{sph}}(r_c) - U_{\text{half}}(h_1) - U_{\text{half}}(h_2) \quad (\text{G.2})$$

where  $U_{\text{half}}(h)$  is found by integrating over a semi-infinite domain and is given by Eq. 4.7.

The second case where the atom lies exactly on the boundary is also easily solved in this manner. Since the atom lies exactly on the boundary, we cannot use the same correction as in the first case, since  $U_{\text{half}}(0)$  diverges. However, we can instead consider only a hemisphere tail

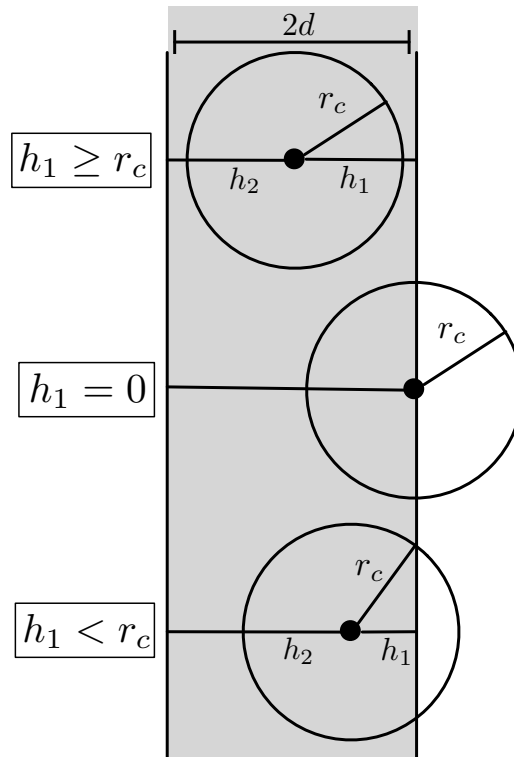


Figure G.1: Sketch of cutoff scenarios for an atom in a slab with cutoff radius  $r_c$ , thickness  $2d$ , distances to edges  $h_1$  and  $h_2$  ( $h_1 \leq h_2$ ), and full periodicity in other dimensions.



---

## G. TAIL CORRECTIONS

---

correction and then subtract a single semi-infinite half plane to obtain the missing energy

$$\Delta U_{ij} = \frac{1}{2} U_{\text{sph}}(r_c) - U_{\text{half}}(2d) \quad (\text{G.3})$$

The nontrivial case occurs when the distance to the boundary is less than the cutoff radius. As before, we add back a full spherical tail correction, and subtract two semi-infinite half planes. However, this removes some interactions that were never calculated in simulation since they lie inside the cutoff radius (more specifically inside a spherical cap), so this energy must be restored. The energy of the cap is found by integrating in spherical coordinates

$$U_{\text{cap}}(r_c, h) = \frac{\rho_j}{2} \int_0^{\phi'} \int_{r(\phi)}^{r_c} U(r) 2\pi r^2 \sin \phi dr d\phi \quad (\text{G.4})$$

where  $\cos \phi' = h/r_c$  and  $r(\phi) = h/\cos \phi$  are the necessary limits of integration in this geometry. Carrying out this integration gives the result in Eq. 4.8. Then, the complete tail correction is

$$\Delta U_{ij} = U_{\text{sph}}(r_c) - U_{\text{half}}(h_1) - U_{\text{half}}(h_2) + U_{\text{cap}}(r_c, h_1) \quad (\text{G.5})$$

## Finite thickness correction

Suppose that we have a slab of thickness  $2d$  sufficiently thick that a continuum approximation is valid for atoms a distance  $d$  away. It is our goal to extend the slab to “infinite” thickness (Figure H.1). We first separate the slab into two half slabs of thickness  $d$  (Step 1). Then we can add a continuum slab of thickness  $L$  to the middle (Step 2). If we let  $h_i$  be the nearest edge distance for the  $i$ -th atom with a specific atom type, then we can add the energy of each atom interacting with this slab by integrating the Lennard-Jones potential. If the total added thickness is  $L$ , then the atom is “missing” energy from a distance  $2d - h_i$  away to a distance  $2d - h_i + L$  away (indicated by arrows). This is because we have already calculated the potential in the first  $2d - h_i$  from simulation. Then, the correction  $\Delta U_{L,i}$  is

$$\Delta U_{L,i} = \frac{\rho_j}{2} \int_{2d-h_i}^{2d-h_i+L} \int_0^\infty U(\sqrt{r^2+z^2}) 2\pi r dr dz \quad (\text{H.1})$$

However, we want to expand the added slab to infinite thickness, so letting  $L$  tend to infinity, we find that  $\Delta U_{L,i}$  simply becomes  $U_{\text{half}}(2d - h_i)$ .

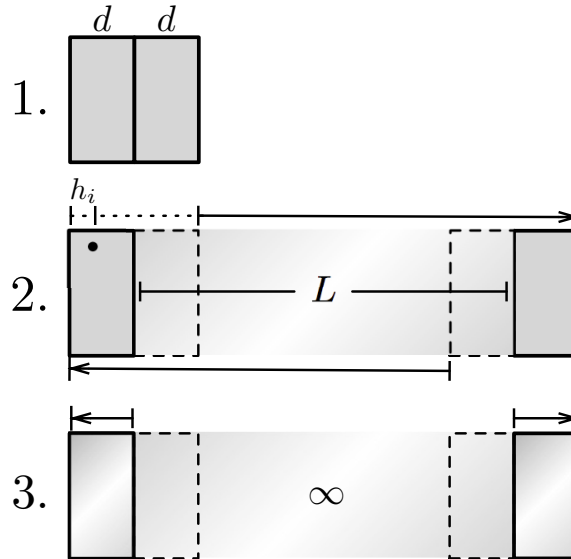


Figure H.1: Schematic of finite thickness correction.

---

## H. FINITE THICKNESS CORRECTION

---

Currently, our correction is described in terms of discrete atom positions  $h_i$ . However, if  $d$  is large, then the half slabs may also be treated as a continuum. The correction term to the surface tension is half of the cohesive energy per unit area of interface, which is equivalent to the energy in one of the half slabs per area (Step 3). Integrating through this half slab gives the correction term to the surface tension per unit area for density of type  $i$  in the half plane interacting with type  $j$  in the added infinite plane.

$$\Delta\sigma'_{ij} = \rho_i \int_d^{2d} U_{\text{half}}(h) dh \quad (\text{H.2})$$

$$= \frac{\pi}{2} \rho_i \rho_j \epsilon_{ij} \left[ \frac{\sigma_{ij}^{12}}{90} \left( \frac{1}{d^8} - \frac{1}{(2d)^8} \right) - \frac{\sigma_{ij}^6}{3} \left( \frac{1}{d^2} - \frac{1}{(2d)^2} \right) \right] \quad (\text{H.3})$$

Then, the correction term to the surface tension is

$$\Delta\sigma' = \sum_{i,j}^{\text{types}} \Delta\sigma'_{ij} \quad (\text{H.4})$$

where the sum is taken over all possible atom types for the half plane and the added infinite plane.

## Wall parameters

The Lennard-Jones 9-3 potential for a single atom with a single wall atom type (reformulated in terms of  $(C^{(6)}, C^{(12)})$  parameters rather than  $(\sigma, \epsilon)$  parameters) is

$$U_{ij} = \pi \rho_j \left[ \frac{C_{ij}^{(12)}}{45h^9} - \frac{C_{ij}^{(6)}}{6h^3} \right] \quad (\text{I.1})$$

where

$$C_{ij}^{(12)} = 4\epsilon_{ij}\sigma_{ij}^{12} \quad (\text{I.2})$$

$$C_{ij}^{(6)} = 4\epsilon_{ij}\sigma_{ij}^6 \quad (\text{I.3})$$

However, we want to represent the interaction of the  $i$ -th atom with *all* atom types in the crystal. Assuming a wall density of  $\rho_w$  and summing over all  $n$  atom types in the wall

$$U_i = \pi \rho_w \sum_j^n \frac{\rho_j}{\rho_w} \left[ \frac{C_{ij}^{(12)}}{45h^9} - \frac{C_{ij}^{(6)}}{6h^3} \right] \quad (\text{I.4})$$

$$= \pi \rho_w \left[ \frac{\bar{C}_i^{(12)}}{45h^9} - \frac{\bar{C}_i^{(6)}}{6h^3} \right] \quad (\text{I.5})$$

where we have defined  $\bar{C}_i^{(12)}$  and  $\bar{C}_i^{(6)}$  as

$$\bar{C}_i^{(12)} = \frac{1}{\rho_w} \sum_j^n 4\rho_j (\epsilon_{ii}\epsilon_{jj})^{1/2} (\sigma_{ii}\sigma_{jj})^6 \quad (\text{I.6})$$

$$\bar{C}_i^{(6)} = \frac{1}{\rho_w} \sum_j^n 4\rho_j (\epsilon_{ii}\epsilon_{jj})^{1/2} (\sigma_{ii}\sigma_{jj})^3 \quad (\text{I.7})$$

according to the geometric mixing rule of the OPLS forcefield. Further, the OPLS forcefield in GROMACS requires that the Lennard-Jones parameters be in the  $(\sigma, \epsilon)$  form. This conversion is

---

## I. WALL PARAMETERS

---

straightforward to carry out, and the required formulae for choosing the nonbonded parameters are

$$\bar{\sigma}_i = \left( \frac{\bar{C}_i^{(12)}}{\bar{C}_i^{(6)}} \right)^{1/6} \quad (\text{I.8})$$

$$\bar{\epsilon}_i = \frac{(\bar{C}_i^{(6)})^2}{4\bar{C}_i^{(12)}} \quad (\text{I.9})$$

Notice that  $\bar{\epsilon}_i$  has a factor of  $1/\rho_w$ , which shows that the wall density may be arbitrarily chosen as a convenient value (e.g. so that  $\bar{\sigma}_i$  and  $\bar{\epsilon}_i$  are of the same order as typical  $(\sigma, \epsilon)$  values).

## Effect of tail corrections on Hessian

As stated in the text, given a large enough cutoff radius, we can analyze the effect of tail corrections on the normal modes by analyzing the magnitude of tail corrections to the Hessian matrix. We require two important criteria: (1) that the cutoff radius is large enough that a continuum approximation is valid, and (2) all atoms are at their positions corresponding to the “true” energy minimum.

A cutoff radius of 1.0 nm is large enough that all important short-ranged interactions are treated discretely, and a continuum approximation beyond the cutoff is valid. Although we have expanded the cutoff radius to 1.9 nm and approximated with continuum beyond this cutoff when computing the tail corrections, we could have also simply approximated with continuum beyond the original 1.0 nm with minimal loss of accuracy.

It is also important that the Hessian is computed around the “true” position of atoms at the energy minimum. If the atoms are not at their “true” minimum, the Hessian may not accurately represent the system. The tail correction in the bulk crystal is constant, so the atoms have no additional forces. We state without proof (for now) that the forces in the slab system are negligibly small, so we may reasonably assume that the atoms are at their “true” minimum energy positions. This statement will be justified later. It is thus valid to analyze corrections to the Hessian by considering only the second derivatives of the tail corrections.

By definition, the  $(i, k)$ -th entry in the Hessian is

$$H_{ik} = \frac{\partial^2 U}{\partial x_i \partial x_k} \quad (\text{J.1})$$

where  $i$  and  $k$  are indexes corresponding to atom number and the coordinate axis of differentiation. Since tail corrections are additive, the tail correction to the Hessian  $\Delta H_{ik}$  is

$$\Delta H_{ik} = \frac{\partial^2 \Delta U}{\partial x_i \partial x_k} \quad (\text{J.2})$$

where  $\Delta U$  is the total tail correction of either the bulk or slab system

$$\Delta U = \sum_i^N \sum_j^n \Delta U_{ij} \quad (\text{J.3})$$

and  $N$  is the number of atoms and  $n$  is the number of density types. For the bulk system,  $\Delta U_{ij}$  is a constant term independent of atom position ( $U_{\text{sph}}$ ), and so  $\Delta H_{ik}$  will be zero.

The tail corrections in the slab system, on the other hand, have a position dependence. From Eq. 4.6, the correction on the  $i$ -th atom is decoupled from other atoms and varies only in a single dimension, so  $\Delta H_{ik}$  will be zero for all  $i \neq k$  and for all dimensions that are not the slab dimension. This amounts to correcting one-third of the diagonal elements of the Hessian.

Taking two derivatives in the slab dimension is equivalent to taking two derivatives with respect to the nearest edge distance  $h_1$ , and eliminates all atoms in  $\Delta U$  except for the  $i$ -th atom. Analyzing the dominant term of  $\Delta U_i$  shows that

$$\Delta U_i \sim \begin{cases} n\varepsilon\rho\sigma^6 h/r_c^4 & h \leq r_c \\ n\varepsilon\rho\sigma^6/h^3 & h > r_c \end{cases} \quad (\text{J.4})$$

where  $\varepsilon$  and  $\sigma$  are “typical” Lennard-Jones parameters,  $\rho$  is the “typical” density, and  $h$  is the nearest edge distance. This implies that

$$\Delta H_{ii,x} \sim \begin{cases} 0 & h \leq r_c \\ n\varepsilon\rho\sigma^6/h^5 & h > r_c \end{cases} \quad (\text{J.5})$$

where the subscript  $x$  attempts to clearly indicate that this correction is only necessary for the slab dimension. So, of the one-third of diagonal elements that could be corrected, only those atoms that are far from the edge will have a non-zero correction. The maximum correction will occur for atoms that are  $r_c$  from the edge, where  $\Delta H_{ii,x} \sim n\varepsilon\rho\sigma^6/r_c^5$ .

The effect of the tail correction to the Hessian can be analyzed by comparing the magnitude

of the correction to the Lennard-Jones term in the Hessian  $H_{ii}|_{LJ}$ . Because of Lennard-Jones 1-4 exclusions, we expect only attractive terms so

$$U_{ij}|_{LJ} \sim \frac{\epsilon \sigma^6}{r^6} \quad (\text{J.6})$$

Taking two derivatives and summing shows

$$H_{ii}|_{LJ} \sim \frac{N \epsilon \sigma^6}{r^8} \quad (\text{J.7})$$

where  $N$  is the number of atoms inside the cutoff radius (but outside the 1-4 exclusions). The characteristic radius for these interactions must be on the order of  $\sigma$ . For the rough purpose of scaling, the number of atoms in that shell for a cutoff radius of a few  $\sigma$  should be

$$N \sim n \rho r^2 \Delta r \sim n \rho \sigma^3 \quad (\text{J.8})$$

in a continuum sense, so  $H_{ii}|_{LJ} \sim n \epsilon \rho \sigma$ . Comparing the two terms

$$\frac{\Delta H_{ii,x}}{H_{ii}|_{LJ}} \sim \left( \frac{\sigma}{r_c} \right)^5 \ll 1 \quad (\text{J.9})$$

Therefore, the tail correction to these elements of the Hessian is negligible, and we may be reasonably confident that the normal modes are accurate.

Note that this analysis was predicated on the assumption that  $r_c$  was sufficiently large to accurately capture the short-ranged interactions. If  $r_c$  became small, our scaling shows that these corrections would no longer be negligible. Moreover, for large  $r_c$  the correction will actually decay faster (like  $1/r_c^6$  when  $r_c \gg \sigma$ ).

We have previously stated that forces due to tail corrections in the slab dimension are negligibly small. By a similar argument to the Hessian, the force corrections in the periodic dimensions



are zero and

$$\Delta F_{i,x} \sim n\epsilon\rho\sigma^2\left(\frac{\sigma}{r_c}\right)^4 \ll 1 \quad (\text{J.10})$$

in the slab direction, so these derivatives are indeed negligible and the atoms may be assumed to be at their “true” minimum.

**Local Address**  
0502 Simmons Hall  
University Park, PA 16802  
(484) 883 5770

**Permanent Address**  
40 Sullivan Chase Drive  
Avondale, PA 19311  
(610) 268 2327

# Michael Howard

mph5128@psu.edu

---

## EDUCATION

**B.S. in Chemical Engineering; Minor, Mathematics**  
The Pennsylvania State University, University Park, PA

## PUBLICATIONS

M.P. Howard and S.T. Milner, "Numerical simulation methods for the Rouse model in flow".  
*Physical Review E* **84**, 051804 (2011).

## SUBMITTED MANUSCRIPTS

M.P. Howard and S.T. Milner. "A simple model for heterogeneous nucleation of isotactic polypropylene."

M.P. Howard and S.T. Milner. "Calculated interfacial tensions and heterogeneous nucleation of isotactic polypropylene."

## RESEARCH EXPERIENCE

### Undergraduate Research

Pennsylvania State University                      University Park, PA                      Fall 2010 – Summer 2013

- Advisor: Scott Milner
- Computational and experimental investigation of flow-induced crystallization and nucleation of isotactic polypropylene
- Skills: Mathematica, C, Python, GROMACS simulation package

### NSF REU in Soft Materials

Pennsylvania State University                      University Park, PA                      Summer 2010

- Advisor: Scott Milner
- First place in poster competition ("Analytical simulations of the Rouse model in shear flow")

## AWARDS

### Selected Honors and Awards

NDSEG Fellow

Goldwater Scholar

National Merit Scholar

Larry Duda Undergraduate Student Research Award

Eagle Scout

### Complete Listing

Department of Defense NDSEG Fellowship (2013)

NSF Graduate Research Fellowship Honorable Mention (2013)

Student Marshal, Department of Chemical Engineering (2013)

Evan Pugh Scholar Award – Seniors (2013)

Donald S. Cryder Scholarship in Chemical Engineering (2012)

Lee and Mary Eagleton Award for Excellence in Design (2012)

Larry Duda Undergraduate Student Research Award in ChE (2012)

Barry M. Goldwater Scholar (2012)

Evan Pugh Scholar Award – Juniors (2012)

President Sparks Award (2011)

First Place – Penn State NSF REU in Soft Materials Poster Contest (2010)  
 McWhirter Undergraduate Scholarship (2010)  
 President's Freshman Award (2010)  
 College of Engineering Scholarship (2009-13)  
 Academic Excellence Scholarship (2009-13)  
 Fred C. and Mary Koch Foundation Scholarship (2009-13)  
 National Merit Scholar (2009-13)  
 National AP Scholar (2009)  
 High School Valedictorian (2009)  
 Eagle Scout (2008)

## **PROFESSIONAL EXPERIENCE**

APS March Meeting 2013, talk, "A simple model for heterogeneous nucleation of isotactic polypropylene."  
 AIChE Annual Fall Meeting 2012, talk, "Stochastic splitting methods for numerical simulation of Rouse chains in flow."

## **TEACHING EXPERIENCE**

### **Teaching Intern**

ChE 210: Introduction to Material Balances

Fall 2012 – Spring 2013

- Held weekly office hours and review sessions
- Developed and graded quiz problems
- Delivered selected lectures during semester

### **Grader**

ChE 430: Chemical Reaction Engineering

Spring 2012

- Graded weekly homework assignments
- Provided feedback on class performance to instructor

## **LEADERSHIP & ACTIVITIES**

Recording Secretary, Tau Beta Pi (PA B)  
 Instrument Manager and Member, Penn State Pride of the Lions Athletic Band  
 Technology Chair, A-7 THON (<http://a7forthekids.org>), supporting the Penn State IFC/Panhellenic Dance MaraTHON (philanthropy benefitting pediatric cancer patients and research)  
 Student Member, American Institute of Chemical Engineers  
 Student Member, American Physical Society